Mathematical modelling of unsteady tube stretching with internal channel pressurisation for fabricating electrospray ionisation emitters

Gagani Pathumika Ranathunga

March, 2022

Thesis submitted for the degree of
Doctor of Philosophy
in
Applied Mathematics
at The University of Adelaide
Faculty of Engineering, Computer and Mathematical Sciences
School of Mathematical Sciences

THE UNIVERSITY
of ADELAIDE

Contents

List of Tables

List of Figures

Signed Statement

I certify that this work contains no material which has been accepted for the award of any other degree or diploma in my name, in any university or other tertiary institution and, to the best of my knowledge and belief, contains no material previously published or written by another person, except where due reference has been made in the text. In addition, I certify that no part of this work will, in the future, be used in a submission in my name, for any other degree or diploma in any university or other tertiary institution without the prior approval of the University of Adelaide and where applicable, any partner institution responsible for the joint award of this degree. I give permission for the digital version of my thesis to be made available on the web, via the University's digital research repository, the Library Search and also through web search engines, unless permission has been granted by the University to restrict access for a period of time.

Signed: .... Date: 08/03/2022

Acknowledgements

First and foremost I would like to express my sincere gratitude to my principal supervisor Professor Yvonne Stokes for her invaluable supervision, patience, motivation, and immense knowledge throughout the years of my Ph.D studies. She is one of the most extraordinary people I have ever met, from whom I have gained invaluable knowledge not only in mathematical modelling but also in terms of professional development. It has been my greatest privilege to have her guidance to achieve my lifelong dream of obtaining a Ph.D. Thank you for giving me this wonderful opportunity.

I would also like to extend my sincere thanks to my co-supervisor, Dr Michael Chen, for his immense support at every stage of this research project. I am extremely grateful to have received his insights and knowledge, which have helped me succeed in my research. Despite his busy schedule, he has always been very supportive throughout and provided continual assistance whenever it was required. I am grateful for his immense support with the thesis writing, by providing detailed feedback, which has been very important to me.

I would like to thank to my co-supervisor, Professor Heike Ebendorff-Heidepriem, for generously providing me with lots of valuable suggestions with the model validation and experiments. I wish to also convey a special thanks to Dr Anna Radionova for her experimental expertise, and suggestions in this research. Thank you for spending long hours conducting experiments and collecting data to support this thesis. I am also grateful

to Mr Graham Brown, Design Engineer at Sutter Instrument Company for providing valuable information about the Sutter P-2000 instrument which provided an excellent direction for the experiments.

I would also like to thank the School of Mathematical Sciences and the University of Adelaide for giving me this prestigious opportunity to pursue my dream supported by a full scholarship. Thank you for providing all the necessary facilities and creating a great environment that helps students succeed in their academic and professional goals. Furthermore, I am thankful to have received financial support in the form of a top up scholarship for this research from Trajan Scientific and Medical, which has supported me to undertake this research project. A special thank you goes to Dr Kyle Bachus and Dr Andrew Gooley, of Trajan Scientific and Medical for their patience, direction, appreciation and trust in the outcomes of this research and consideration of patent protection for the outcomes. I also here acknowledge that the experimental work was in part conducted at the OptoFab node of the Australian National Fabrication Facility utilizing Commonwealth and SA State Government funding.

I would like to express my heartfelt gratitude to Dr Alison-Jane Hunter for supporting me in numerous untold ways. She is an exceptionally wonderful person. I am eternally grateful for her continuous support, invaluable advice, and diligent efforts in editing my thesis voluntarily whenever I requested. Thank you for always being there for me.

I want to express my gratitude to my family including my parents, husband, and sister for always believing in my potential and talent. I have always been inspired to accomplish my goals because of their love and encouragement. I sincerely appreciate the support of my husband throughout my life, without which I would have stopped these studies a long time ago. Thank you for having long conversations with me, giving me valuable suggestions to understand difficult concepts and for reading my thesis.

Abstract

Nanoelectrospray ionisation (nESI) is a useful technology for assessing the chemical composition of various liquid samples using mass spectrometry (MS). Significant efforts have been made in the design of nESI emitters, as their shape and geometry are critical to the electrospray performance and subsequent MS detection. In the actual manufacturing of these emitters through the heat and draw process, the desired geometry cannot, at present, be achieved. In particular, the inner channel reduces in size, which is not desirable. To improve the sensitivity of biological and chemical mass spectrometry and avoid clogging of the tip, a small near-uniform bore of 10 - 20μm is desirable with the external wall tapering over a length of around 5mm from 75 - 150μm in radius to a sharp end with a radius around 8 - 15μm.

Through mathematical modelling, we demonstrate, for the first time, the feasibility of producing such emitters using the heat and draw process with the addition of pressure in the channel to prevent any reduction in size. In this thesis, we consider the unsteady problem of heating and pulling of an axisymmetric cylindrical glass tube, using asymptotic methods to exploit the slenderness of the tube and over-pressure applied within the inner channel, to form tapers with a near uniform bore and small wall thickness at the tip. This is an unsteady extensional flow problem. As the glass temperature increases, the viscosity reduces until the central heated region extends and thins rapidly to yield an hour-glass

shape. During stretching, the cross-sectional geometry will also deform under the effects of surface tension and applied pressure, with the pressure counteracting the closure of the channel by surface tension and, perhaps, further expanding it. When cooled and cut transversely at the centre, two identical tapered capillaries are obtained.

In this thesis, we assume molten glass is a Newtonian fluid, and develop coupled flow and energy models to examine in detail the influence of the process parameters on the geometry, namely the pulling force, pressure, temperature, and surface tension. The use of an over-pressure in the channel, to counteract the reduction in its size as the cross-sectional area decreases due to pulling and the channel closes due to surface tension, is of particular interest. The model and solution method described in this thesis enable determination of a pulling force, channel over-pressure, and draw time to achieve tapers with the desired internal diameter and wall thickness at the very tip from a given tubular fibre for a temperature dependent viscosity.

Chapter 1

Introduction

In the current field of medical research, tapered glass tubes have a broad variety of applications — tapered optical microscopes, glass microelectrodes, nanopipettes, microneedles, nanoelectospray emitters, and optical fibres (Gallacchi et al. 2001, Huang et al. 2007, Morris et al. 2010, Yadav et al. 2020, Gibson et al. 2009, Fitt et al. 2001) to name but a few. The detection and recognition of macromolecules is one of the most demanding activities in different fields of science. Due to its high resolution and speed, mass spectrometry (MS) is often used to determine chemical composition, bio-molecular structures, and for identification of unknown chemicals within samples. Electrospray ionisation (ESI), is a technique that generates a small spray of charged droplets (in the form of an aerosol) from the tip of a tapered capillary having a small diameter channel, known as an emitter, by the application of a high voltage electric field (Figure 1.1). This technique has revolutionised the use of ionisation in the investigation of bio-molecules such as peptides and proteins since its introduction for MS by Malcolm Dole in 1968 (Dole et al. 1968). As opposed to other analytical approaches, electrospray ionisation mass spectrometry (ESI-MS) is fast, sensitive and accurate. ESI generates single or multiple charged ions that can be collected

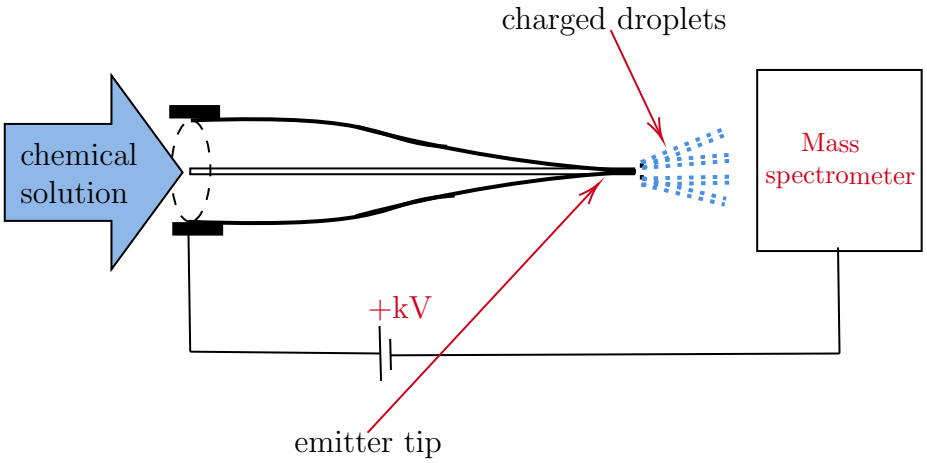

Figure 1.1: Schematic of ESI-MS technique

and analysed by a mass spectrometer. A detailed description of ESI-MS is given by Wu (2012). A mini-review of the process and some clinical applications are summarised in Ho et al. (2003).

One key factor affecting the ionisation efficiency of the ESI is the emitter tip, from which the fluid escapes, which usually tapers to a sharp tip. One way to improve ionisation efficiency is to reduce the size of the emitter tip (Sander & Elisabeth 2007). When the whole tip diameter is lowered to a few micrometres, significantly smaller charged droplets are produced by lowering the total flow rate to the nanoelectrospray regime (1,000 nL/min), which reduces sample consumption and increases sensitivity (Gibson et al. 2009, Wilm & Mann 1996). The first nanoelectrospray ionisation emitter (nESI) created by Wilm & Mann (1994) was a gold-coated glass capillary with a tip of around 1 - 3μm. It has been established that at these flow rates, the geometry of the nESI emitter tip is critical to creating small droplets for sensitive MS detection (Sander & Elisabeth 2007) . However, emitters frequently experience problems with clogging (Gibson et al. 2009, Wu 2012).

Various tapering methods have been employed for the development of emitters from

glass tubes of $150 - 300\mu$m initial outer diameter, including grinding of one end of the tube to the desired dimension at the tip (Kriger et al. 1995, Kusỳ et al. 2007, Tycova et al. 2016), and chemical etching (Kelly et al. 2006). The focus of this thesis is the heat and pull method (Valaskovic et al. 1995, Yuill et al. 2013), whereby a short segment of the glass tube is heated in the middle while it is pulled from either end so that it thins over the heated region to an hour-glass shape which can be cut to yield tapered emitters. The heating can be effected using a flame (Hannis & Muddiman 1998), a laser Wilm & Mann (1996), or an electric discharge between two electrodes Ek & Roeraade (2011). The tapering process results in a reduction in the diameter of the inner channel which can lead to clogging of the emitter tip when in use (Kelly et al. 2006). Moreover the internal channel can entirely close during the heat and pull process, which might be rectified by cutting off a portion of the tip (Hannis & Muddiman 1998). This process often requires a series of experiments to set the pull parameters in order to obtain emitter tips with a suitable geometry and the usual process always yields emitters in which the inner channel decreases in size towards the tip, which is not ideal to preserve the continuous flow of the fluid. Recently, there has been considerable interest in the application of pressure to prevent a decrease in size of the channel and produce a taper with uniform inner channel. Such emitters are required for nano-electrospray ionisation (nESI) mass spectrometry to improve the sensitivity in analysis of liquid samples.

The focus of this thesis is using mathematical modelling to evaluate the possibility of the manufacture of tapered capillaries with (near) uniform bore, using the heat and pull method with pressurisation of the channel. To improve the sensitivity of biological and chemical MS and avoid clogging of the tip, a small near-uniform bore of 10 - 20μm (radius $5 - 10\mu$m) is considered desirable with the external wall tapering over a length of around 5mm from 75 - 150μm in radius to a sharp end with a radius around 8 - 15μm.

The desired geometry with a near-uniform bore and a sharp tip cannot be achieved using the existing fabrication process of heat and draw as the inner channel diameter decreases in size, along with the outer diameter. As a result mathematical modelling is needed to determine whether or not these emitters can be fabricated using the heat and draw process, where pressure is used to stop closure of the internal channel. This is an unsteady extensional flow problem. As the glass temperature increases, the viscosity reduces until the central heated region extends and thins rapidly to yield an hour-glass shape. During stretching the cross-sectional geometry will also deform under the effects of surface tension and applied pressure, with pressure counteracting the closure of the channel by surface tension and, indeed, further expanding it to reverse the reduction in the channel size brought about by stretching. When the capillary breaks at the centre under the pulling force (or otherwise if it is cut there), two identical tapered capillaries are obtained.

1.1 Literature review

A closely related process to the unsteady capillary stretching we consider in this study is manufacture of glass micro-electrodes from axi-symmetric tubing by the heat and pull process, essentially identical to that described, excepting that no over pressure is applied in the inner channel. This was studied by Huang et al. (2003, 2007) for both fixed and variable pulling forces using a coupled flow and temperature model which neglected surface tension and, as already mentioned, did not include channel pressure in the inner channel. It is just one application of a class of extensional flow problems that have received significant attention, particularly in the last 30 years, which concern the stretching of a slender cylinder to form a long thin fibre/thread. Other applications include the spinning of textile threads, rheological measurement, and the manufacture of optical fibres using

fibre drawing. The process of fibre drawing is used in the fabrication of optical, polymer and textile fibres. The fluid mechanics of both fibre drawing and capillary stretching has been studied mathematically over the past 50 years.

Matovich & Pearson (1969) were the first to derive and use a one dimensional model to investigate the quasi-steady spinning of axisymmetric textile threads having no internal structure. More recent similar models include Wylie & Huang (2007) and Wylie et al. (2007). The quasi-steady drawing of tubes, with an over-pressure inside the tube but neglecting surface tension, was first investigated by Pearson & Petrie (1970), again using a one dimensional model, in studying the blowing of tubular films. Motivated by the steady-state drawing of microstructured optical fibres in a draw tower, Fitt et al. (2001, 2002) exploiting the slenderness of the (axisymmetric) capillary, developed an asymptotic model of capillary drawing and undertook a preliminary examination of the competition between surface tension and over-pressure in the tube. Asymptotic studies of unsteady stretching of axisymmetric viscous threads by pulling of the ends or under gravity include Dewynne et al. (1989), Stokes et al. (2000, 2011*a*), Stokes & Tuck (2004), Bradshaw-Hajek et al. (2007), Wylie & Huang (2007), Wylie et al. (2007, 2011, 2016), Howell et al. (2007) and Wylie et al. (2015). All of this work assumed negligible surface tension and a viscosity that is constant or varies axially in a prescribed manner.

A formal derivation of the asymptotic fluid-flow equations for unsteady drawing of nonaxisymmetric fibres was first given by Dewynne et al. (1992) assuming negligible inertia and surface tension and a viscosity that is at most a function of time or axial position. This work showed the simplification of the solution process brought by moving from the laboratory Eulerian reference frame to a Lagrangian reference frame, and formally demonstrated that, in the absence of surface tension, the shape of the cross-section will be preserved though it may change in scale and rotate. This model was later modified to

include inertia, with inclusion of surface tension and its role in changing the cross-sectional shape briefly discussed (Dewynne et al. 1994).

Cummings & Howell (1999) developed a model built on that of Dewynne et al. (1994) and including surface tension and constant viscosity to develop a leading order model of steady fibre drawing (for solid non-axisymmetric geometries) comprising a one-dimensional ODE problem for axial stretching along with a two-dimensional Stokes flow problem for the flow in the cross-section. They identified the significant concept of 'reduced time' to modify the kinematic condition (condition on free boundaries) in the cross plane problem to make it a classical two dimensional Stokes flow problem driven by unit surface tension which can be readily solved. Griffiths & Howell (2007, 2008) applied this model to steady drawing of non-axisymmetric thin-walled tubes subject to surface tension but with no pressurisation of the internal channel. They also added temperature to the model, assuming temperature to be uniform in the cross-section. Stokes et al. (2014) extended the model to fibres of arbitrary geometry; a key finding of this last work is the ability to express the axial stretching problem in terms of the reduced time variable of the cross-plane problem so that both axial and cross-plane problems can be solved independently to describe the final fibre geometry. They also showed that, for steady fibre drawing where only the geometry of the initial preform and final fibre are important, not the geometry through the entire neck-down region from preform to fibre, measurement of pulling tension obviates the need to model temperature.

During glass stretching the surface tension acts to close the internal structures whereas internal channel pressurisation can be useful to counteract surface tension and to keep the holes open. A number of authors have studied the effects of pressure in controlling the final fibre geometry numerically and experimentally. Fitt et al. (2001, 2002) considered axisymmetric tubes with pressurisation of the internal channel in the absence of surface

tension, and both surface tension and pressure for channels of small diameter. Luzi et al. (2010) performed full three-dimensional simulations and validated these using experimental data. Griffiths & Howell (2007) proposed that holes of small diameter can be preserved through the balance between surface tension and pressure but did not demonstrate this. Voyce et al. (2009) showed that sealing the ends of the tube can be used to pressurise the air channels. This is called 'self-pressurisation'. Chen et al. (2015) considered the active pressurisation of the channels without sealing the ends of the fibre, extending the model of Stokes et al. (2014) to develop a model for fibres of arbitrary geometry in which the axial stretching and cross-plane problems are fully coupled. They have shown mathematically and experimentally that channel pressurisation can be used to modify internal geometry of the fibres that would otherwise close due to surface tension. While the competition between surface tension and over-pressure has been considered in some detail for steady fibre drawing (Chen et al. 2015), this remains to be done for unsteady fibre drawing and it is this problem that is addressed in this thesis in order to determine whether emitters for mass spectrometry with (near) uniform bore can be manufactured by the heat and pull method.

Temperature and thus the viscosity plays an important role in the deformation process. Since viscosity decreases greatly with increasing temperature, glass can be softened so that manipulation is easy. For a complete model of steady or unsteady fibre drawing either the viscosity must be known or a temperature model must be coupled to the flow model and a temperature-viscosity relation known. Fitt et al. (2002) and Griffiths & Howell (2008) derived temperature models assuming the leading order temperature to be uniform in a cross-section. Yarin (1986) studied the effect of heat exchange with external environment. A complete formal derivation of the temperature model, demonstrating leading-order uniformity in the cross-section, is given by He et al. (2016) for unsteady

stretching of axisymmetric threads and by Stokes et al. (2019) for steady drawing of fibres with arbitrary geometry with non-negligible surface tension.

Considerable research has been undertaken into unsteady stretching of axi-symmetric viscous threads by pulling of the ends or under gravity including Dewynne et al. (1989), Stokes et al. (2000, 2011*a*), Stokes & Tuck (2004), Bradshaw-Hajek et al. (2007), Wylie & Huang (2007), Wylie et al. (2007, 2011, 2016), Howell et al. (2007) and Wylie et al. (2015). All of this work assumed negligible surface tension and a viscosity that is constant or varies axially in a prescribed manner. Mathematical modelling of unsteady stretching in gravitational extrusion is discussed with experimental results in Tronnolone et al. (2017) for a slender fluid cylinder of arbitrary shape. This study has similarities to the present study but, in our study, we set the gravitational force to zero, pull with a horizontal force, and use pressure to control the inner channel.

While some of the work on steady fibre drawing is applicable to unsteady fibre stretching, new work is required to handle the mathematical details of the unsteady stretching process as it is necessary to consider the changes of different physical variables over time. In steady fibre drawing, the primary focus is on the initial (preform) and final fibre geometry that is pulled with a given draw ratio (the ratio between the draw speed to the feed speed) over a fixed length called the "neck-down" region. The temperature distribution along the length of the neck-down region is unimportant, and the analysis can be performed using a mean temperature/harmonic mean of the viscosity along the length of the neck-down region (Stokes et al. 2014, Chen et al. 2015). In contrast, the geometry along the neck-down/heated region is of importance in our study to obtain a desired emitter geometry, and therefore the problem is more complex with the interdependence of the viscosity (or temperature) and the fibre geometry of great interest. Thus determining the final geometry of the emitter necessitates solving of coupled flow and energy balance mod-

els. Further while Chen et al. (2015) used internal channel pressurisation to prevent hole collapse because of surface tension, in this study, internal channel pressurisation is used with the aim of preserving the internal channel diameter at the initial value throughout the entire length of the emitter, which in fact cannot be guaranteed by the application of pressure alone but rather by the balance of other parameters.

Thus, in this project, we will study the fabrication of glass tubes with uniform bore radius (without hole collapse) when subjected to heating and pulling with the use of over pressure in the channel to counteract reduction in size as the cross-sectional area decreases during the fabrication process. From the above literature review, it is clear that although both fluid flow and temperature models have been considered, surface tension is generally neglected in the unsteady setting. Moreover, the temperature gradient through the fibre, the balance between pressure and surface tension and use of pressure to control the cross-sectional geometry in the context of maintaining the bore radius in an unsteady setting have not been explored and this is our interest. Past work done on asymptotic modelling of steady and unsteady fibre drawing is expanded for application to the fabrication of hollow-core tapers (where the core diameter is, typically, less than 100 micrometres).

The proposed project aims to fill the above-identified gaps in the literature and to understand the impact of various operational parameters of the unsteady stretching process on achieving the desired final geometry of the taper. Literature relevant to the explorations of this thesis that are not here mentioned will be discussed throughout this thesis where applicable.

1.2 Research questions and objectives

Because of the small-scale nature of our problem, both modelling and experimentation are complex to perform. In addition, the problem requires a variety of scales. The characteristic axial scale, for example, is on the order of 1 mm, while radial variations occur over a shorter range of 1 μm to 10 μm or even smaller. Because of the high temperatures in the heater zone and the small fibre sizes involved, even experimental measurements are complicated and time-consuming. Given the problem's complexity, a mathematical model is needed that incorporates the physics, to provide a deeper understanding of the fabrication process and better setting of the control parameters to obtain the required shape of the final fibre. This is expected to inform the development of a commercial manufacturing process to produce emitters in the future and indicate the unique nature of the research along with its positive, practical outcome.

Our research describes the process of tapering from the initial phase (solid glass tube) to the final phase (emitter), ultimately predicting the final shape of the emitter, while being able to mathematically explain the entire heating and drawing process with internal channel pressurisation and temperature control to help advance the development of an important new technology. The production of tapers with a uniform internal channel diameter in particular requires an understanding of the interplay of the underlying physical effects due to different parameters such as surface tension, pressure, pulling force and temperature control.

In summary, the objectives of this thesis are:

1. to extend the current understanding related to the unsteady stretching of glass tubes,

2. to provide a mathematical model that describes the unsteady drawing of an axi-symmetric glass tube with pressurisation in the internal channel for the heat and draw process,

3. to develop a model which is useful to predict the practical aspects of the drawing procedure, such as the fibre breaking point, parameters that lead to bursting, total extension length, and final geometries with various parameters,

4. to predict control parameters to achieve the required shape.

More specifically, we are interested in finding answers to the following questions:

1. Is it possible to fabricate tapers with a uniform internal bore to an acceptable tolerance by the heat and pull technique?

2. What are the key parameters that control geometry in the process of heat and draw?

3. Can a constant pressure and a controlled temperature variation be used to achieve a desired taper?

4. Is the effect of surface tension important?

The mathematical analysis developed in this thesis enables examination of these questions and investigation of the interplay between temperature, pulling force, surface tension and over-pressure in the inner channel on the geometry of the final emitter.

1.3 Methodology

To achieve the above objectives, we have employed a systemic approach that includes theoretical, and numerical approaches followed by some experimental validation. In particular, we aim to solve coupled flow and temperature models under constant surface tension with pressurisation of an internal air channel to alter the fibre geometry.

The theoretical approach involves the development of a mathematical model of heating and stretching of an axi-symmetric glass tube in the context of manufacturing emitters for mass spectrometry. As previously mentioned, the existence of a sharp tip with a uniformly preserved internal channel is desired in order to improve analysis of fluid samples by mass spectrometry. According to the literature, the major parameters that characterise the deformations of the geometry when drawing a capillary are surface tension, pulling force, viscosity which depends on temperature, and pressure. Therefore, we have developed a model to investigate the importance of these parameters and their effects on the final geometry.

As the glass softens due to heating, it is referred to as "molten glass", which can be thought of as a very viscous fluid and is assumed to be Newtonian, as in the majority of past work on modelling fibre drawing (Cummings & Howell 1999, Griffiths & Howell 2007, Stokes et al. 2014, Tronnolone 2016). The assumption that molten glass is an incompressible fluid is also widely held; it is thought to be accurate enough for practical purposes. Thus, we assume that molten glass is an incompressible Newtonian fluid with a temperature-dependent viscosity. Newtonian fluids have stress that is directly proportional to the rate of strain. In this connection, the constant of proportionality is precisely the viscosity. Newtonian fluids instantaneously relax upon application of a stress, regardless of its magnitude. For very viscous fluids such as molten glass, inertia can be neglected as the flow is very slow. As a result, we use the Stokes flow model. In setting up the problem we follow Dewynne et al. (1994) and develop asymptotic sub-models for fluid and energy flow using the slenderness of the capillary. By this means we reduce the complexity of the Navier Stokes equations by dropping the less significant terms, and obtain a model which can be solved very efficiently. This approach has been used widely throughout the literature for steady and unsteady drawing problems (Dewynne et al. 1994, Cummings

& Howell 1999, Fitt et al. 2002, Griffiths & Howell 2008, Wylie & Huang 2007, Stokes et al. 2014, Chen et al. 2015). We start by considering the drawing of glass tapers under a fixed force, including pressure and constant surface tension similar to the steady fibre draw model of Chen et al. (2015), but we adapt the work for unsteady drawing.

The complexity of our complete PDE model is such that it must be solved numerically and for this we use the commercial software, MATLAB. Our model includes several input parameters. Material properties are among the most important and unpredictable inputs. While some of these properties were extracted directly from the literature, the others were determined/estimated by matching to experimental data, provided by Dr A. Radionova, an experimentalist at the Institute of Photonics and Advance Sensing (IPAS) at the University of Adelaide, where the experiments were conducted. Since measurement is difficult due to large temperature changes, the micro/nano scale nature of the problem and limitations and inaccuracies in the equipment used, the experimental results contain error and uncertainties. Nonetheless, the experiments provide valuable additional validation for the model.

1.4 Summary

In summary, this thesis aims to improve the robustness and clogging resistance associated with the traditional heat and draw method in fabricating tapered emitters by showing that pressure in the internal channel might be used to reduce the tapering of internal walls compared with the outer walls. Our principal objective is to derive and use a mathematical model to investigate the interplay between temperature, pulling force, surface tension and over-pressure on the geometry of the final emitter. It is important to note that the theory developed here can be generalised and applied to a broader class of problems related to extensional flow problems.

1.5 Thesis structure

In Chapter 2, we develop a mathematical model for the unsteady heat and draw process used for tapering of tubular glass fibres pulled with a constant force. An over-pressure above atmospheric pressure may be applied within the internal channel. Considering the slenderness of the tube, we use asymptotic methods to simplify the model equations that will be applied throughout this thesis. We also discuss the method of generating numerical solutions using a specified viscosity profile.

In Chapter 3 we show and discuss the numerical results from the model developed in Chapter 2 using a viscosity that varies axially in a prescribed manner when the effects of surface tension are significant in the flow. The model and solution method here described enable determination of a pulling force, channel over-pressure, and draw time to achieve tapers with a desired internal diameter and wall thickness at the very tip. Additionally, we discuss the rationale behind the selection of various draw parameters, and the possible limitations that may be encountered during the draw process, such as capillary bursting or breaking, in parameter regimes relevant to emitter fabrication.

In Chapter 4, we discuss the scenario of having strong pressure effects compared with surface tension in the transverse flow with numerical simulations for a prescribed viscosity. This chapter also discusses a simplified flow model that can be solved analytically when the effects of surface tension are negligible and shows when the effect of surface tension might be neglected.

To complete our model development for an unsteady heat and draw process, a temperature model must be coupled to the flow model and, in Chapter 5, we develop an energy model assuming the glass is heated by a laser. We also give numerical solutions to the full model including coupled flow and temperature, using a temperature-dependent viscosity.

Following this, in Chapter 6, a comparison of numerical and experimental observations is made first to determine unknown parameters after which further experiments were used to validate the model. The puller used was not capable of applying pressure in the inner channel so that the validation was performed for zero pressure.

The conclusions arrived at throughout the course of this study are summarised in Chapter 7. This chapter also includes suggestions for future research.

We here note that a substantial amount of the work presented in Chapters 2 and 3 is to be reported in an upcoming publication; see Ranathunga et al. (2022).

Chapter 2

Mathematical formulation of the flow model

2.1 Introduction

The development of a mathematical model that describes the heat and draw process is the first step towards obtaining a quantitative understanding of emitter fabrication. In Section 2.2 of this chapter, we model the unsteady stretching of an axisymmetric glass tube pulled by a fixed force under the assumption that the molten glass is an incompressible Newtonian fluid. The glass tube typically has an internal diameter of about 10μm and external diameter around 120μm. After stretching, this tapers down to a tip diameter of around 20 - 25μm over a length of about 10mm, so that the wall thickness is very small. Due to stretching and the effect of surface tension the outer and inner walls will tend to narrow down to form a sharp tip during this process. We aim to maintain a uniform inner channel by including internal channel pressure in our model similar to the study by Chen et al. (2015). We introduce a small parameter for the slender geometry

and apply asymptotic techniques to develop a leading order model which captures the essential features of this process. In view of the extensive explanations already given in the literature on modelling of similar processes we present only the principal derivation steps here.

Section 2.2 consists of a mathematical description of the problem followed by the key steps in the derivation of the governing equations. As the glass is heated, it softens and can be considered to be a Newtonian fluid. We will neglect inertia since molten glass is highly viscous and flows very slowly. As a result, we will use the Stokes flow model. An asymptotic extensional flow model is used here due to the slenderness of the tube (the length scale in the direction of stretching is much larger compared to the width). Similar models have been used widely throughout the literature for steady and unsteady drawing problems (Cummings & Howell 1999, Fitt et al. 2002, Griffiths & Howell 2008, Stokes et al. 2014, Chen et al. 2015, Dewynne et al. 1994, Wylie & Huang 2007, Tronnolone et al. 2016). The full Navier-Stokes equations are reduced by neglecting less significant terms to obtain a model which can be solved very efficiently. Thus, a three-dimensional fibre stretching process is reduced to a one-dimensional axial stretching problem and a two dimensional free-boundary Stokes flow problem in the direction perpendicular to axial stretching, commonly called the 'cross plane' or 'transverse flow' model. A Lagrangian coordinate system similar to Dewynne et al. (1994), Cummings & Howell (1999), Griffiths & Howell (2007, 2008), Stokes et al. (2014), Chen et al. (2015) is adopted. In this system the deformation of a cross-section is an unsteady problem.

In Section 2.3 we introduce a numerical method to solve the axial and cross-plane model. This new numerical method is a key point of difference between the work in this thesis and previous similar studies in the literature. Following discussion of the numerical method, we examine the evolution of the geometry for a simple piecewise constant heater

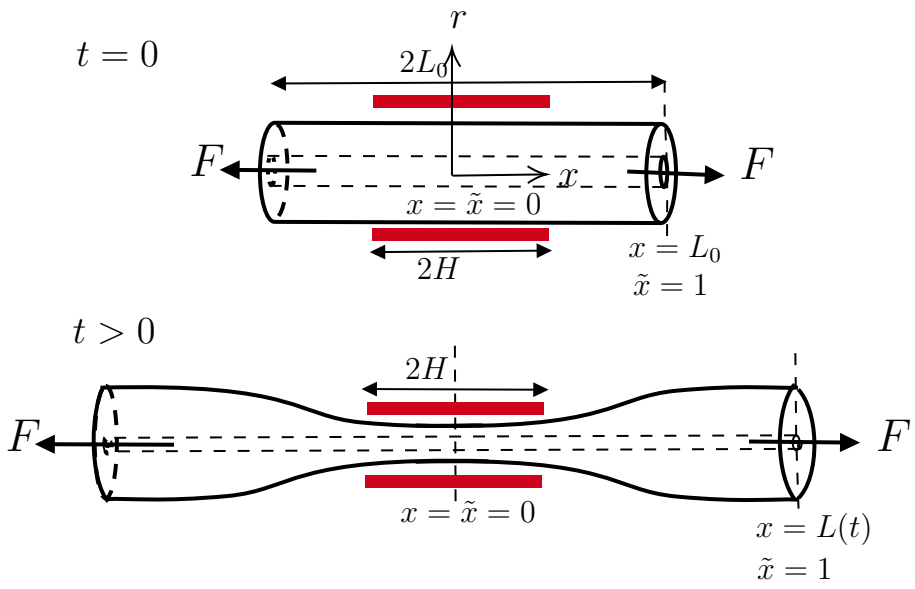

Figure 2.1: The tapering process

profile, which illustrates some of the key aspects of our problem.

2.2 Mathematical modelling

We consider the stretching of a slender axi-symmetric glass capillary of initial length $2L_0$, which is heated over a fixed distance $2H$ in the centre and pulled from both ends with a fixed force F. To describe this motion, we adopt a cylindrical polar coordinate system in which the x axis is directed along the axis of the tube with $x = 0$ (origin) at the centre of mass of the tube, and r is the radial coordinate (shown in Figure 2.1). All field variables are only dependent on r and x, the radial and axial positions, under the axi-symmetric assumption. Symmetry enables our consideration of just half of the tube, $0 \leq x \leq L(t)$, equivalent to an axi-symmetric tube held fixed at $x = 0$, heated over $0 \leq x \leq H$. As the softened glass is pulled, its length increases over time t starting from an initial length of $L(0) = L_0$. The cross-sectional area of the capillary tube is denoted

by $S(x,t) = \pi R^2(1-\phi^2)$, where $R(x,t)$ is the external radius and $\phi(x,t)$ is the ratio between inner to outer radii, known as the aspect ratio. Initially, the tube has uniform cross-sectional area, external radius and aspect ratio along its length, so that $S(x,0) = S_0$, $R(x,0) = R_0$ and $\phi(x,0) = \phi_0$. The total of the internal and external boundary lengths at position x and time t is denoted $\Gamma(x,t)$. A constant pressure P may be applied within the inner channel to prevent its closure, as the overall geometry narrows and forms a neck around $x = 0$.

The softened glass is assumed to be an incompressible Newtonian fluid with constant density ρ and surface tension γ; however, the viscosity μ of glass depends strongly on temperature and so is, in general, a function of position and time $\mu(x,t)$. To study the flow of the glass, we denote the fluid velocity as $\mathbf{u} = (u,v)$, where $u(\mathbf{x},t)$ and $v(\mathbf{x},t)$ are the axial and radial components of the velocity at position $\mathbf{x} = (x,r)$ and time $t \geq 0$, while $p(\mathbf{x},t)$ denotes the pressure in the fluid. The axi-symmetric fluid flow is governed by the continuity equation and Navier-Stokes equations for the axial and radial conservation of momentum. These are

$$\frac{\partial u}{\partial x} + \frac{\partial v}{\partial r} + \frac{v}{r} = 0, \tag{2.1a}$$

$$\rho\left(\frac{\partial u}{\partial t} + v\frac{\partial u}{\partial r} + u\frac{\partial u}{\partial x}\right) = -\frac{\partial p}{\partial x} + \frac{\partial}{\partial x}\left[2\mu\left(\frac{\partial u}{\partial x}\right)\right] + \frac{1}{r}\frac{\partial}{\partial r}\left[\mu r\left(\frac{\partial v}{\partial x} + \frac{\partial u}{\partial r}\right)\right], \tag{2.1b}$$

$$\rho\left(\frac{\partial v}{\partial t} + v\frac{\partial v}{\partial r} + u\frac{\partial v}{\partial x}\right) = -\frac{\partial p}{\partial r} + \frac{\partial}{\partial x}\left[\mu\left(\frac{\partial v}{\partial x} + \frac{\partial u}{\partial r}\right)\right] + \frac{\partial}{\partial r}\left[2\mu\left(\frac{\partial v}{\partial r} + \frac{v}{r}\right)\right]. \tag{2.1c}$$

We denote the shape of the external and internal boundaries of the capillary as $G^{(0)}(x,r,t) = 0$, and $G^{(1)}(x,r,t) = 0$, respectively. In order to fully specify the problem, the govern-

ing equations, (2.1a) - (2.1c) must be supplemented with the boundary conditions. On both the internal and external boundaries we apply a dynamic boundary condition that incorporates both surface tension and pressure, namely

$$-p\mathbf{n}^{(i)} + \mu\left(\nabla\mathbf{u} + (\nabla\mathbf{u})^T\right)\cdot\mathbf{n}^{(i)} = -(\gamma\kappa^{(i)} + P^{(i)})\mathbf{n}^{(i)},\ i = 0, 1, \tag{2.2}$$

where $\mathbf{n^{(i)}}$ is the outward normal to the boundary, denoted by $\mathbf{n}^{(i)} = \nabla G^{(i)}/|\nabla G^{(i)}|$, and $\kappa^{(i)}$ is the curvature of the boundary. Note that $P^{(i)}$ is the applied pressure, which only appears in the stress condition for the inner boundary and thus $P^{(0)} = 0$ in all cases (Chen et al. 2015), and here $P^{(1)} = P$. We also apply a kinematic boundary condition on both boundaries namely,

$$\frac{\partial G^{(i)}}{\partial t} + \mathbf{u}\cdot\nabla G^{(i)} = 0, \quad i = 0, 1. \tag{2.3}$$

The governing equation (2.1) and boundary conditions (2.2) and (2.3) will be solved to describe how the flow in the glass and shape of the taper develops over time.

2.2.1 Scaling

We now non-dimensionalise the governing equations and boundary conditions. This technique has many advantages: it decreases the number of parameters involved by prioritising the dominant parameters; it allows for the estimation of the relative value of each of the terms; and it allows for direct comparison of various scenarios using the non-dimensional parameters. Ultimately, we will reduce the complexity of the flow equations and develop a model that can be solved efficiently.

We use the following scales to non-dimensionalise the quantities in our math model,

where hats denote the dimensionless quantities:

$$(x,r) = H(\hat{x},\epsilon\hat{r}), \quad (u,v) = U(\hat{u},\epsilon\hat{v}), \quad t = \frac{H}{U}\hat{t}, \quad p = \frac{\mu_{hot}U}{H}\hat{p}, \quad \mu = \mu_{hot}\hat{\mu},$$
$$\gamma = \frac{\mu_{hot}U\chi_0}{H}\hat{\gamma}, \quad F = \frac{6\mu_{hot}U\chi_0^2}{H}\hat{F}, \quad P = \frac{\mu_{hot}U}{H}\hat{P}, \tag{2.4}$$
$$S = \chi_0^2\hat{S}, \quad \Gamma = \epsilon H\hat{\Gamma}, \quad R = \chi_0\hat{R}.$$

Here $\chi_0 = \sqrt{S_0}$ is the square root of the cross-sectional area of the initial capillary, defined for convenience, and μ_{hot} is a representative value of the viscosity of glass when it is at or near its hottest. We assume that the capillary is slender, defined as $\epsilon = \frac{\sqrt{S_0}}{H} \ll 1$ as has been used previously in the modelling of fibre drawing by (Dewynne et al. 1994, Cummings & Howell 1999, Fitt et al. 2002, Griffiths & Howell 2008, Stokes et al. 2014, Chen et al. 2015, Tronnolone et al. 2016, Stokes et al. 2019). Prior to any movement, the glass tube is symmetrical about $x = 0$, which is the centre of the tube, and its initial velocity is zero. The flow velocity scale U is a characteristic velocity which will be defined differently in Chapters 3 and 4 in accordance with the parameters which are important in a given scenario.

We now apply the above scaling to the three-dimensional fibre stretching problem (2.1) - (2.3). The resulting scaled equations have only even powers of ϵ, thus we expand the dependent variables $\hat{u}, \hat{v}, \hat{p}$ and $\hat{S}$ as perturbation series in ϵ^2, that is,

$$\hat{u} = u_0 + \epsilon^2 u_1 + \epsilon^4 u_2 + \dots, \tag{2.5a}$$
$$\hat{v} = v_0 + \epsilon^2 v_1 + \epsilon^4 v_2 + \dots, \tag{2.5b}$$
$$\hat{p} = p_0 + \epsilon^2 p_1 + \epsilon^4 p_2 + \dots, \tag{2.5c}$$
$$\hat{S} = S_0 + \epsilon^2 S_1 + \epsilon^4 S_2 + \cdots. \tag{2.5d}$$

We substitute the above expressions into the scaled governing equations, to separate each equation at different orders of ϵ^2, and retain only the dominant terms in the equations. This reduces the full problem to a one-dimensional axial stretching problem describing the motion in the direction of fibre stretching and a two dimensional transverse flow model (Cummings & Howell 1999).

2.2.2 Axial stretching model

We assume $\epsilon \ll 1$ and, following Dewynne et al. (1989), we find that at leading order (2.1b) and (2.1c) yield

$$\frac{1}{r}\frac{\partial}{\partial r}\left(\mu r \frac{\partial u_0}{\partial r}\right) = 0 \implies u_0 = u_0(x,t), \tag{2.6a}$$

$$\frac{\partial p_0}{\partial r} = 0 \implies p_0 = p_0(x,t). \tag{2.6b}$$

Thus, the axial velocity and pressure are independent of the cross-plane position. Moreover, as shown in Huang et al. (2007), He et al. (2016) and Stokes et al. (2019), a similar process can be used to show that the temperature within a cross-section in a slender geometry is constant at leading order, and so independent of the radial coordinate r and a function of only x and t. Accordingly, in the ongoing analysis of this chapter, we assume that the viscosity $\mu(x,t)$ is a function of x and t, since the viscosity is strongly dependent on the temperature. It follows that at leading-order we solve (2.1a) to obtain the radial velocity v_0 as

$$v_0 = -\frac{r}{2}\frac{\partial u_0}{\partial x}. \tag{2.7}$$

Continuing, we expand $\hat{u}$, $\hat{v}$, and $\hat{p}$ on the boundaries also using the expansions (2.5) to find (2.2) to leading order, and follow Dewynne et al. (1989) to obtain leading order

equations for mass and momentum. After dropping hats on the dimensionless variables and subscripts on the leading order dependent variables the full axial stretching problem reduces to

$$\frac{\partial \chi^2}{\partial t} + \frac{\partial}{\partial x}(u\chi^2) = 0, \tag{2.8}$$

$$\mathrm{Re}\,\chi^2\left(\frac{\partial u}{\partial t} + u\frac{\partial u}{\partial x}\right) - \frac{\partial}{\partial x}\left(3\hat{\mu}\chi^2\frac{\partial u}{\partial x}\right) - \frac{\hat{\gamma}}{2}\frac{\partial \Gamma}{\partial x} = 0, \tag{2.9}$$

where $\chi^2 = S$, subject to the initial conditions $\chi^2(x,0) = 1$ and $u(x,0) = 0$.

In (2.9), the Reynolds number $\mathrm{Re} = \rho L^2\gamma/\mu_{hot}^2\chi_0$ is a dimensionless quantity that signifies the ratio between inertial to viscous forces associated within a flow. In general, viscous forces dominate at low Reynolds numbers; at high Reynolds numbers, inertial forces become stronger, ultimately resulting in a turbulent flow. Due to the high viscosity of molten glass, the flows considered here have a very low Reynolds number, and thus the inertial forces are negligible. Furthermore, for typical parameters used in the manufacture of emitters, $\mathrm{Re} \sim (10^{-8})$; hence terms multiplied by Re will be neglected.

In an unsteady setting, it is useful to rewrite (2.8) in terms of a material derivative, that is

$$\frac{D\chi^2}{Dt} + \chi^2\frac{\partial u}{\partial x} = 0, \tag{2.10}$$

where $D/Dt = \partial/\partial t + u\,\partial/\partial x$. These model equations (2.7) - (2.9) for the axial flow have been used previously by Stokes et al. (2014) neglecting the time dependence, for steady fibre drawing. However, we retain the time dependence as our problem is unsteady.

We now adopt a Lagrangian reference frame tracking the motion of a material cross-section. To this end we label each cross-section of the fibre with its initial position $\tilde{x}$, that

is

$$\tilde{x} = x(\tilde{x}, 0), \tag{2.11}$$

where $x(\tilde{x}, t)$ is the axial position of material cross-section $\tilde{x}$ at time t such that $\tilde{x} \in [0, 1]$, as $x(0, t) = 0$, and $x(1, t) = L(t)$, see Figure 2.1. Following Stokes & Tuck (2004) we use the conservation of mass to transform between Lagrangian and Eulerian coordinates. Thus, the relationship between x and $\tilde{x}$, and is given by

$$\frac{\partial x}{\partial \tilde{x}} = \frac{\chi^2(\tilde{x}, 0)}{\chi^2(\tilde{x}, t)}, \quad x(0, t) = 0, \tag{2.12}$$

or simply,

$$x(\tilde{x}, t) = \int_0^{\tilde{x}} \frac{1}{\chi^2(\tilde{x}', t)} d\tilde{x}'. \tag{2.13}$$

Evaluating (2.13) for $\tilde{x} = 1$ gives the physical axial length of the tapered geometry resulting from the flow field that develops with time t. This allows for an arbitrary initial geometry for the fluid cylinder, but because our initial geometry is a tube with a uniform cross-sectional area, we set $\chi^2(\tilde{x}, 0) = 1$. Substituting from (2.10) into (2.9) yields

$$\frac{\partial}{\partial x}\left(3\hat{\mu}\frac{D\chi^2}{Dt} - \frac{\hat{\gamma}\Gamma}{2}\right) = 0. \tag{2.14}$$

Integrating with respect to x, and transforming (2.14) into Lagrangian coordinates yields a single first order differential equation for the cross-sectional area χ^2 as

$$3\hat{\mu}\frac{D\chi^2(\tilde{x}, t)}{Dt} - \frac{\hat{\gamma}\Gamma(\tilde{x}, t)}{2} = -6F(t), \tag{2.15}$$

where $6F$ is the pulling force. We further assume this force is constant in time and the factor 6 has been introduced for later convenience as per Stokes et al. (2014).

To be able to solve the axial model (2.15) we first need to find Γ, the total cross-sectional boundary length. As shown by Dewynne et al. (1994), without surface tension ($\hat{\gamma} = 0$) a cross-section only deforms in scale and the term in (2.15) that involves Γ is removed, enabling a straightforward solution to the axial stretching problem. However, for non-negligible surface tension, the boundary length has to be determined. In general, it is determined by solving a 2D cross plane model for flow in the cross-section, where the transverse geometry changes in scale due to the axial motion and deforms in shape due to surface tension and any pressure applied within the channel acting on the boundaries.

2.2.3 Surface tension driven transverse flow model

In an unsteady setting, the cross-plane flow is best explained in terms of Lagrangian coordinates where we move from $\tilde{x} = 0$ to $\tilde{x} = 1$ in the frame of reference. We also rescale the transverse flow variables, r the cross-plane (radial) length, Γ the total boundary length of a cross-section and $\kappa^{(i)}$ the curvatures of the boundaries, as follows:

$$r = \chi_0 \tilde{r}, \quad \Gamma = \chi_0 \tilde{\Gamma}, \quad \kappa^{(i)} = \frac{\tilde{\kappa}^{(i)}}{\chi_0}. \tag{2.16a}$$

Note that $\tilde{r}$ is not a Lagrangian co-ordinate in the cross-section $\tilde{x}$, as the cross-section changes in shape due to surface tension and applied pressure, but $\tilde{x}$, the initial axial position x at time $t = 0$, remains a Lagrangian variable for each cross-section. Following Cummings & Howell (1999) and Stokes et al. (2014) we rescale the dependent variables pressure and radial velocity for non-zero surface tension, assuming no rigid rotation in the cross-plane flow, as

$$p = p_z + \frac{\hat{\gamma}}{\chi}\tilde{p}, \quad v = v_z + \frac{\hat{\gamma}\tilde{v}}{\hat{\mu}(x,t)}, \tag{2.17}$$

where p_z and v_z are the leading order cross-plane flow solutions for zero surface tension and $\tilde{p}$, and $\tilde{v}$ are the new dimensionless variables in the cross plane flow.

Furthermore, we introduce a reduced time variable τ (Cummings & Howell 1999) to modify the kinematic condition in the cross-plane problem to render it a classical two dimensional Stokes flow problem driven by unit surface tension which can be readily solved. In this thesis we use a modified definition of reduced time accounting for axially varying viscosity $\mu(x,t)$ as in Stokes et al. (2014), which transforms deformations in τ within a cross-section to the time variable t, given as:

$$\frac{d\tau}{dt} = \frac{\hat{\gamma}}{\hat{\mu}(\tilde{x},t)\chi(\tilde{x},\tau)}, \quad \tau(\tilde{x},0) = 0. \tag{2.18}$$

The reduced time defines the amount of deformation within a cross-section, such that the larger the value of τ the greater the deformation within a particular cross-section. However, from (2.18), it is apparent that this can be regulated through the ratio between $\hat{\gamma}/\hat{\mu}$. With the introduction of the reduced time transformation, the resulting cross-plane problem is a classical two-dimensional moving boundary Stokes flow problem driven by unit surface tension and defined in a domain of unit area. For an axi-symmetric tube the flow through a cross-section can be obtained by solving

$$\frac{1}{\tilde{r}}\frac{\partial}{\partial\tilde{r}}(\tilde{r}\tilde{v}) = 0, \tag{2.19a}$$

$$\frac{\partial\tilde{p}}{\partial\tilde{r}} + \frac{1}{\tilde{r}}\frac{\partial}{\partial\tilde{r}}\left(r\frac{\partial\tilde{v}}{\partial\tilde{r}}\right) = 0, \tag{2.19b}$$

subject to free-surface boundary conditions, which include pressure $\hat{P}$ in the internal

channel following Chen et al. (2015). These are

$$-\tilde{p} + 2\frac{\partial \tilde{v}}{\partial \tilde{r}} = -\tilde{\kappa}^{(0)}, \quad \text{on } \mathrm{G}^{(0)} = 0, \tag{2.19c}$$

$$-\tilde{p} + 2\frac{\partial \tilde{v}}{\partial \tilde{r}} = -(\tilde{\kappa}^{(1)} + \frac{\hat{P}}{\hat{\gamma}}\chi), \quad \text{on } \mathrm{G}^{(1)} = 0, \tag{2.19d}$$

$$\frac{\partial G^{(i)}}{\partial \tau} + \tilde{v} = 0, \quad \text{on } \mathrm{G}^{(i)} = 0, \text{ where } i = 0, 1. \tag{2.19e}$$

Now $\tilde{r} = \tilde{R} = 1/\sqrt{\pi(1-\phi^2)}$ is the external radius on the external circular boundary $G^{(0)}$ and $\tilde{r} = \phi(\tau)\tilde{R}$ is the radius of the inner circular boundary $G^{(1)}$ at reduced time τ, from which $G^{(0)} = \tilde{r} - \tilde{R}$ and $G^{(1)} = \rho\tilde{R} - \tilde{r}$, and the curvatures are $\tilde{\kappa}^{(0)} = 1/(\tilde{R})$ and $\tilde{\kappa}^{(1)} = -1/(\phi\tilde{R})$ respectively. After solving for velocity and pressure and substituting in the kinematic conditions, the corresponding equation for ϕ in terms of τ is

$$\frac{d\phi}{d\tau} = -\frac{\sqrt{\pi}}{2}(1+\phi)^{3/2}(1-\phi)^{1/2} + \frac{1}{2}\frac{\hat{P}}{\hat{\gamma}}\phi\chi, \tag{2.20}$$

and the total boundary length is

$$\tilde{\Gamma} = 2\sqrt{\frac{\pi\,(1+\phi)}{(1-\phi)}}. \tag{2.21}$$

Returning to the previous non-dimensional problem, the outer radius $R(\tau)$ of the tube can be determined in terms of ϕ as

$$R(\tau) = \frac{\chi(\tau)}{\sqrt{\pi(1-\phi(\tau)^2)}}, \tag{2.22}$$

where $\pi R^2(\tau)(1-\phi^2(\tau)) = \chi^2(\tau)$, along with the inner channel radius of the tube as

$$\phi(\tau)R(\tau) = \frac{\phi(\tau)\chi(\tau)}{\sqrt{\pi(1-\phi(\tau)^2)}}. \tag{2.23}$$

Accordingly, the solution of the cross-plane problem (2.19) yields the evolution of the traverse flow geometry of the rescaled cross-plane problem, having a unit cross-sectional area, with respect to τ. A key observation to be made along with the introduction of pressure, as highlighted in Chen et al. (2015) is that the presence of the axial variable χ multiplying the pressure $\hat{P}$ in (2.20) couples the cross-plane and axial flow models, meaning they must be solved simultaneously to obtain the final geometry. Additionally, the evolution of the cross-plane geometry with respect to τ does not explicitly involve viscosity $\mu(x,t)$ and so any associated deformations are only evident when results are transformed to physical time t.

2.2.4 Full model

The full model comprises the 1D axial flow and 2D transverse flow models defined in equations (2.15), and (2.20). In order to solve the equations simultaneously and utilise the solution for a cross-section $\tilde{x}$ in Lagrangian coordinates, we first transform (2.15) to reduced time τ using (2.18). Thus, the axial model obtained with respect to reduced time τ is

$$\frac{D\chi}{D\tau} - \frac{\chi}{12}\tilde{\Gamma}(\tilde{x},\tau) = -\frac{\hat{F}}{\hat{\gamma}}. \tag{2.24}$$

Substituting for boundary length in (2.21), the axial equation (2.24) can be rewritten using the aspect ratio as

$$\frac{D\chi}{D\tau} = \frac{\sqrt{\pi}}{6}\chi\sqrt{\frac{1+\phi}{1-\phi}} - \frac{\hat{F}}{\hat{\gamma}}, \tag{2.25}$$

for an annular capillary of unit cross-sectional area (Chen et al. 2015).

Overall, equation (2.25) fundamentally describes the change in the cross-sectional area of the initial capillary tube with τ due to stretching, while (2.20) governs the shape of each cross-section with respect to τ due the effect of surface tension and applied pressure.

To obtain the evolution of the geometry of the fluid cylinder with respect to time t, we use (2.18) to relate t and τ for each cross-section $\tilde{x}$. Additionally, we use (2.13) to transform between Lagrangian and Eulerian coordinates in order to determine the displacements of the cross-sections $\tilde{x}$. Observe that, because initially the fibre has uniform cross-sectional area and aspect ratio and because the force F is constant, the cross-plane flow equations have no explicit $\tilde{x}$ dependence and may be solved independent of $\tilde{x}$ to obtain the evolution of the geometry with τ at every $\tilde{x}$, unlike the gravity stretching problem of Tronnolone et al. (2016), where gravitational force varies with $\tilde{x}$. Equations (2.25) and (2.20) may be solved first, independently of (2.18) and (2.12), for $\chi(\tilde{x}, \tau)$ and $\phi(\tilde{x}, \tau)$. Accordingly, the system of differential equations (2.25), (2.20), (2.18), and (2.13) comprise the full model that describes the evolution of the geometry with respect to physical coordinates x and t throughout the heat and draw process. These equations are non-linear and are fully coupled so we need to seek numerical solutions.

There are numerous approaches for solving extensional flow problems numerically with their suitability varying according to the nature of the flow and the desired solution. Thus, when selecting a solution approach it is important to take into consideration the key properties of the flow that must be solved for and the desired outcome. For the unsteady problem that we consider in this thesis, we aim to determine how the cylindrical fluid region evolves over time as a result of the motion of the individual material cross-sections.

As discussed in Section 2.2, through the use of a Lagrangian coordinate system and

reduced time, the axial and the cross-plane model equations (2.25) and (2.20) that describe the evolution of the geometry with respect to τ and are fully coupled when the internal channels are pressurised ($\hat{P} > 0$) and so need to be solved simultaneously. In the next section we discuss the procedure for generating these numerical solutions.

2.3 Numerical method

To determine the physical geometry of the tube at physical position x and physical time t we must solve (2.12) and (2.18) for $t(\tilde{x}, \tau)$ and $x(\tilde{x}, \tau)$. This is not at all straightforward because the viscosity μ is assumed to be a known function of physical position x and time t, that is the dependent variables for which we wish to solve, rather than of the independent variables of our model, $\tilde{x}$ and τ. Writing (2.18) and (2.12) in the form

$$\int_0^t \frac{1}{\hat{\mu}(x,\eta)} d\eta = \int_0^\tau \chi(\tilde{x},\tau) d\tau, \tag{2.26}$$

$$x(\tilde{x},t) = \int_0^{\tilde{x}} \frac{1}{\chi^2(\xi,t)} d\xi, \tag{2.27}$$

it is apparent that, although we can evaluate the right-hand-side of (2.26), we need $x(\tilde{x},\eta)$, $0 \leq \eta \leq t$ to determine $t(\tilde{x},\tau)$ for each cross-section $\tilde{x}$ using (2.26), while (2.27) shows that we need $\chi(\xi,t)$, $0 \leq \xi \leq \tilde{x}$ at fixed time t to find $x(\tilde{x},t)$. Thus, these equations are fully coupled in a complex manner, requiring a solution method different from those considered previously for steady and unsteady fibre drawing problems. The viscosity $\hat{\mu}(x,t)$ of each material cross-section is a function of position and time, and so changes as the cross-section moves within the heater as the capillary is stretched. As a result, the position of each cross-section must be monitored continuously over time in order to solve for the flow.

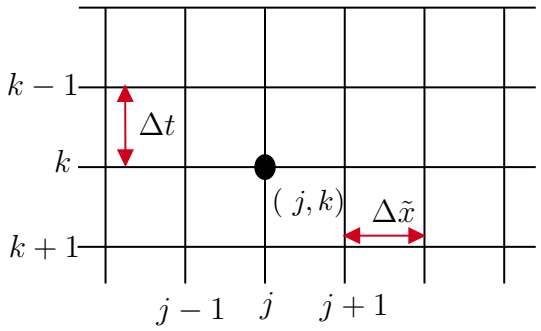

Figure 2.2: Both time and space discretisation in a mesh grid.

2.3.1 Discretisation

The basic method of solving a system of differential equations numerically is to divide continuous variables into discrete intervals, and to estimate the state of the system at the start of each interval. This procedure is known as discretisation. We consider the flow domain and discretise it into a uniform grid in order to evaluate the flow variables. As seen in the previous section, we have two coordinate systems with which to deal, the original (dimensionless) physical coordinates (x, t) in $0 \leq x \leq L(t)$ and the transformed coordinates $(\tilde{x}, \tau)$ defined in a domain $\tilde{x} \in [0, 1]$. Because the physical spatial domain increases over time it is more convenient to use the Lagrangian coordinate $\tilde{x}$, rather than x.

Recalling that (2.25) and (2.20) are independent of $\tilde{x}$ and functions of τ only, we discretise the τ domain by defining

$$\tau_i = i\Delta\tau, \quad \text{where } i = 0, 1, \ldots, I, \tag{2.28}$$

and $\Delta\tau = \tau_{i+1} - \tau_i$ is the reduced-time step. However, a consequence of (2.18), is that the physical time t for a given cross-section (with fixed $\tilde{x}$ value) to attain a particular value of reduced time $\tau > 0$ depends on the history of viscosity experienced by that cross-section.

As a result, it is more convenient to find our solution in terms of the t coordinate rather than τ. Thus we solve in terms of the $(\tilde{x}, t)$ coordinates. The discrete points for $\tilde{x}$ and time t are defined as (see Figure 2.2)

$$\tilde{x}_j = j\Delta\tilde{x}, \quad j = 0, 1, \ldots, J, \tag{2.29a}$$

$$t_k = k\Delta t, \quad k = 0, 1, \ldots, K, \tag{2.29b}$$

where $\tilde{x}_J = L_0/H$ and t_K is the final time to which we wish to compute. The spatial grid points are uniformly distributed over the domain $[0, 1]$ in $\tilde{x}$ with spatial increments $\Delta\tilde{x} = \tilde{x}_{j+1} - \tilde{x}_j$ at the discrete times t_k with time step $\Delta t = t_{k+1} - t_k$. A forward difference approximation of (2.18) yields $\tau(t)$ for each t given by

$$\tau_{j,k+1} = \tau_{j,k} + \frac{\hat{\gamma}\Delta t}{\hat{\mu}_{j,k}\,\chi_{j,k}}, \quad j = 0, 1, \ldots, J, \tag{2.30}$$

where $\tau_{j,k} = \tau(x_j, t_k)$. This allows a numerical approximation of the value of τ_{k+1} at the next time point t_{k+1} by updating the value from the previous time t_k for each k, where $k = 0, 1, \ldots, K-1$. Thus, we iteratively approximate $\tau_{j,k}$ at each time step; starting with $\tau(\tilde{x}_j, 0) = 0 \ \forall\ \tilde{x}_j$ where $j = 0, 1, \ldots, J$. Similarly, we use the trapezoidal rule or an equivalent discretisation of (2.13), to evaluate the integral and numerically approximate x as:

$$x_{j+1,k+1} = x_{j,k+1} + \frac{\Delta\tilde{x}}{2}\left(\frac{1}{\chi^2_{j+1,k+1}} + \frac{1}{\chi^2_{j+1,k+1}}\right), \quad j = 0, 1, \ldots, J-1, \tag{2.31}$$

where $x_{0,k+1} = 0$.

These discretisations enable a simple Euler time-stepping solution procedure for solving our problem, which can be programmed easily and provides sufficient accuracy for suffi-

ciently small Δt. As the number of mesh points and time steps are increased, we should observe convergence to the real solution. Although an analytic solution does not exist for $\hat{P} > 0$ (positive pressure) a semi-analytical solution found in Section 3.3 for $\hat{P} = 0$ will be used to verify the numerical procedure. In the next section we demonstrate use of this procedure to generate an accurate numerical solution to the stretching problem.

2.3.2 Method of Solution

As noted earlier, the initial geometry of our fibre stretching problem is uniform and the cross-plane problem for χ and ϕ as functions of τ is, therefore, the same for any cross-section. Thus we solve (2.25) and (2.20) independently of $\tilde{x}$ as functions of τ alone. In the case of positive pressures, the two equations are coupled and must be solved simultaneously. We solve (2.25) and (2.20) using the MATLAB ODE solver `ode45` to obtain

$$\chi(\tilde{x}, \tau_i) = \chi_i^*, \quad \phi(\tilde{x}, \tau_i) = \phi_i^*, \tag{2.32}$$

which (via interpolation) means we can obtain these values for any τ. In solving this initial value problem we stop the solver when the internal channel closes ($\phi \to 0$), the tube explodes ($\phi \to 1$) or the tube breaks ($\chi \to 0$).

In constructing a numerical solution, we here assume a physically reasonable viscosity profile $\mu(x, t)$ such that the tube deforms over the heated region $0 \leq x \leq 1$ and is effectively solid for $x > 1$. In so doing we neglect the time over which the glass tube heats up from room temperature until it is able to stretch due to the pulling force. We will consider coupling of the flow model to a temperature model, with viscosity dependent on temperature, later in Chapter 5.

We determine the evolution of the flow geometry with time as follows. Assuming the solution is known for $0 \leq t \leq t_k$, we obtain the solution at t_{k+1} by first computing $\tau_{k+1}(t)$ at each $\tilde{x}_j$ node from (2.30) for a given Δt using the solution history until t_k. Subsequently, using the already computed solutions for χ_i^* and ϕ_i^*, we interpolate to obtain the $\chi^*(\tilde{x}_j, t_{k+1})$ and $\phi^*(\tilde{x}_j, t_{k+1})$ values for each $\tilde{x}_j$. To determine the $x(\tilde{x}_j, t_{k+1})$, where $j = 0, 1, \ldots, J$ nodal positions, we use numerical quadrature or the trapezoidal method given in (2.31). Finally, we update the viscosity $\hat{\mu}(\tilde{x}_j, t_{k+1})$ based on the new locations of each cross-section after each time step. We then repeat this time-stepping procedure until the final draw time t_K.

Our time-stepping procedure can be summarised as follows: we aim to obtain the solution $\chi_{j,k} = \chi(\tilde{x}_j, t_k)$, $\phi_{j,k} = \phi(\tilde{x}_j, t_k)$, $\tau_{j,k} = \tau(\tilde{x}_j, t_k)$, $x_{j,k} = x(\tilde{x}_j, t_k)$, and $\hat{\mu}_{j,k} = \hat{\mu}(\tilde{x}_j, t_k)$ for $k = 1, 2, \ldots, K$, where $\chi_{j,0} = 1$, $\phi_{j,0} = \phi_0$, $\tau_{j,0} = 0$, $x_{j,0} = \tilde{x}_j$, and $\hat{\mu}_{j,0} = \hat{\mu}(\tilde{x}_j, 0)$. Assuming the solution to be known at time t_k, our algorithm for obtaining the solution at time t_{k+1} is

1. compute $\tau_{j,k+1}$ using finite differencing as in (2.30), for all the cross-sections $\tilde{x}_j$, where $j = 0, 1, \ldots, J$;

2. determine $\chi_{j,k+1}$ and $\phi_{j,k+1}$ for $j = 0, 1, \ldots, J$ by interpolation of the previously obtained solution $(\tau_i, \chi_i^*, \phi_i^*)$ to (2.25) and (2.20); MATLAB's 'deval' function was used for this;

3. compute $x_{j+1,k+1}$ using (2.31) for $j = 0, 1, \ldots, , J - 1$;

4. update the viscosity i.e. $\hat{\mu}_{j,k+1} = \hat{\mu}(x_{j,k+1}, t_{k+1})$.

This gives the solution at time t_{k+1}. We then increment the time step, and repeat this process through to final time t_K.

It is clear from the algorithm that we must obtain the solution to (2.32) over a sufficiently large τ-range, i.e. for a sufficiently large value I to enable the interpolations of Step 2 of the above time-stepping procedure for all $\tau_{j,k}$. However, should some $\tau_{j,k}$ exceed the maximum possible value such that the internal channel closes, the tube bursts, or the fibre breaks, we simply stop our solution procedure and adjust the final time t_K. Thus, $\tau_I \leq \tau_{\max}$, the maximum possible value of τ at which $\phi = 0$ or $\phi = 1$, or $\chi = 1$. These constraints can be identified by using the 'events' option of MATLAB ODE solvers, which stop the solver if any of these events occur.

In this way, for a given force $\hat{F}$, pressure $\hat{P}$ and viscosity $\hat{\mu}(x,t)$, we can determine the geometry of an emitter at the final time t_K. For accuracy, the time step must be chosen carefully to ensure that nodal displacements in a time step are not too large. If need be the time step can be adjusted during the solution process. The semi-analytical solution, when $\hat{P} = 0$, discussed in Section 3.3 is useful in this situation to provide a good approximation for the size of the time step.

We now illustrate the numerical method discussed above for solving the system of equations outlined in (2.25), (2.20), (2.12) and (2.18), for a simple piecewise constant viscosity profile given by:

$$\hat{\mu}(x) = \begin{cases} 1, & 0 \leq x < 1 \\ 100, & x \geq 1. \end{cases} \tag{2.33}$$

This viscosity is constant in the heated region, with a step change at $x = 1$ from $\hat{\mu} = 1$ in the heated region to $\hat{\mu} = 100$ (cold) in the cold region beyond. We consider the case of positive pressure in the inner channel and use the complete numerical scheme of Section 2.3.2 to obtain solutions to the system of differential equations discussed in Section 2.2.4.

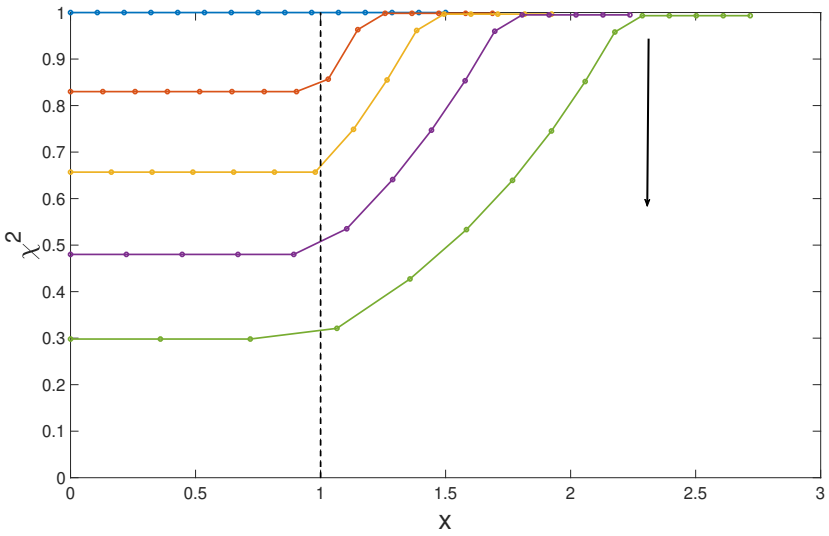

Figure 2.3: The evolution of the cross-sectional area $\chi^2(x,t)$ is shown against axial position x at times $t = 0, 0.05, 0.1, 0.15, 0.2$ for an axisymmetric fibre with initial geometry given by $L(0) = 1.5$, $\chi(x,0) = 1$ and $\phi(x,0) = 0.06$. The filled dots denote 15 individual cross-sections, equispaced at $t = 0$ and labelled by $\tilde{x}$. Pulling with force $\hat{F} = 2$ and pressure $\hat{P} = 32$ results in a decrease in χ for all cross-sections that spend time in the heated region $0 \leq x < 1$, the extent of which is indicated by the black dashed line. Beyond $x = 1$ cross-sections are solid (the viscosity is large) so that no further deformation can occur. The arrow shows the direction of increasing t.

Figure 2.3 shows the change in the cross-sectional area $\chi(x,t)$ with axial position x at different times. The filled dots in these graphs correspond to individual cross-sections $\tilde{x}$ and are used to visualise their motion and aid understanding of the evolution of the geometry. All these cross-sections initially have a unit area of $\chi^2(x,0) = 1$ and are spaced uniformly along the length of the tube. We have chosen $\hat{F} = 2$ (i.e. of a similar magnitude to surface tension) while $\hat{P}$ is an order of magnitude larger. It is evident that inside the heater where the viscosity is sufficiently small ($\hat{\mu} = 1$) the cross-sections reduce in area and are shifted in the direction of pulling as the length of the capillary increases. Because the viscosity in the heated zone is constant in space, all cross-sections that remain in this region throughout the draw experience the same deformation, resulting a tubular tip. As

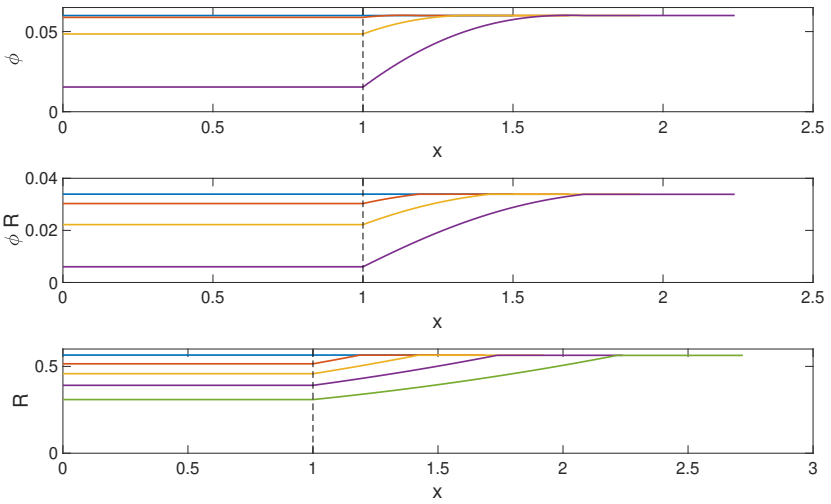

Figure 2.4: The aspect ratio $\phi(x,t)$ (top), internal channel radius $\phi(x,t)R(x,t)$ (middle), and external radius $R(x,t)$ (bottom) are shown against axial position x at times $t = 0, 0.05, 0.1, 0.15, 0.2$, with time increasing from top to bottom for pulling force $\hat{F} = 2$ and pressure $\hat{P} = 32$. The initial geometry of the axisymmetric fibre is $L(0) = 1.5$, $\chi(x,0) = 1$, and $\phi(x,0) = 0.06$. Pulling results in a reduction in $\phi, \phi R, R$ for all cross-sections that spend time in the heated region, $0 \leq x < 1$, the extent of which is indicated by the black dashed line. Once a cross-section leaves the heated region solidification of the glass means that no further change can occur.

a cross-section leaves the heater its viscosity becomes large ($\hat{\mu} = 100$) and deformation ceases so that its geometry remains constant from this point in time. However, due to stretching in the heated region, each cross-section moves in the direction of pulling. All cross-sections initially outside the heated region will not be deformed and retain their unit area but will be shifted in the direction of pulling. The cross-sections that are heated for only some part of the draw time result in a taper from the undeformed part of the tube to the tubular tip. The aspect ratio $\phi(x,t)$ at the tip also reduces rapidly as time increases due to the heating and pulling process and the progressive exit of cross-sections from the heated region.

Figure 2.4 shows the change in the cross plane variables aspect ratio $\phi(x,t)$, the internal

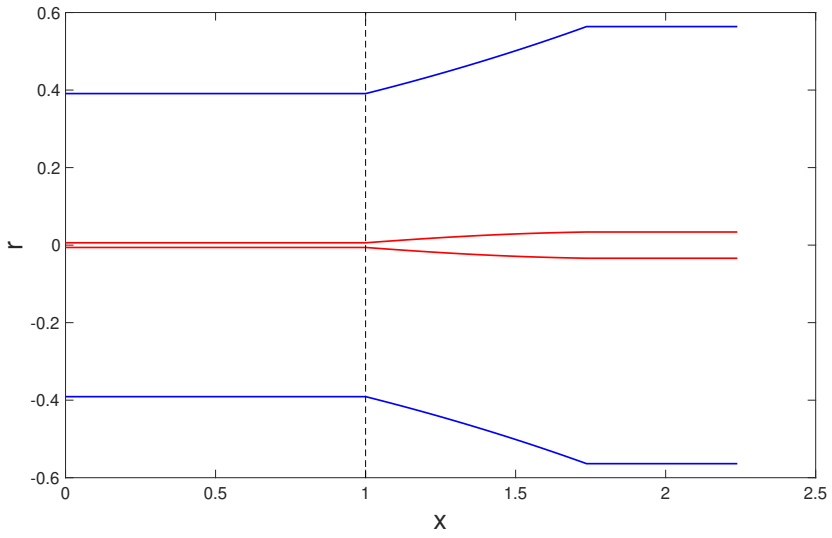

Figure 2.5: Emitter obtained from an axisymmetric tube with initial length $L(0) = 1.5$, cross-sectional area $\chi^2(x, 0) = 1$ and aspect ratio $\phi(x, 0) = 0.06$, by pulling with force $\hat{F} = 2$, and pressure $\hat{P} = 32$ for a time $t_K = 0.15$. The geometry is obtained with the viscosity profile (2.33). The outer boundary $r = R(x, t_K)$ is shown in blue and the inner channel $r = \phi(x, t_K)R(x, t_K)$ is shown in red.

radius $\phi(x, t)R(x, t)$ and external radius $R(x, t)$ with x at the given times t in the figure caption. All these dimensions decrease over time due to heating and pulling and the progressive exit of cross-sections from the heated region, resulting in a taper with a length that increases and a tip radius that decreases over time. At $t = 0.15$, it is apparent from the graph that the inner channel is nearly closed, with the aspect ratio approaching very close to zero. As a result, the curves associated with $t = 2$ are omitted from the ϕ and ϕR plots (hence only 4 curves) as they correspond to a closed inner channel.

With zero surface tension and pressure, the aspect ratio will not change over time (Dewynne et al. 1994, Cummings & Howell 1999) thus the decrease in the aspect ratio in Figure 2.4 shows that the pressure $\hat{P}$ in this case is not sufficient to overcome the effect of surface tension, let alone increase the aspect ratio to maintain the original bore size as

desired for emitters. Figure 2.5 shows the final geometry when $\hat{P} = 32, \hat{F} = 2, t = 0.15$, (channel nearly closing) using the numerical method described above and the viscosity profile in (2.33), which is time independent and piecewise constant in space.

2.3.3 Model solutions for a solid rod

For a geometry with no internal structure, the complicated solution procedure mentioned above is unnecessary. The simplicity in the case of a solid rod stems from the fact that the boundary length can be expressed directly without solving for the traverse flow problem. In this case, the boundary length, Γ is:

$$\pi R^2 = \chi \implies \Gamma = 2\sqrt{\pi}\chi, \tag{2.34}$$

using $\Gamma = 2\pi R$. Substituting in (2.15) and assuming the pulling force is a constant, after some simplification gives an implicit equation for $\chi(\tilde{x}, t)$ as:

$$\chi(\tilde{x}, t) - \chi(\tilde{x}, 0) + \frac{6\hat{F}}{\hat{\gamma}\sqrt{\pi}} \log\left(\frac{\hat{\gamma}\sqrt{\pi}\chi(\tilde{x}, t) - 6\hat{F}}{\hat{\gamma}\sqrt{\pi}\chi(\tilde{x}, 0) - 6\hat{F}}\right) = \frac{\hat{\gamma}\sqrt{\pi}t}{6m(\tilde{x}, t)}, \tag{2.35}$$

where $m(\tilde{x}, t)$ is the harmonic mean of viscosity $\hat{\mu}(\tilde{x}, t)$ at position $\tilde{x}$ over time t defined (Tronnolone 2016) as:

$$m(\tilde{x}, t) = \frac{t}{\int_0^t \frac{1}{\hat{\mu}(\tilde{x}, t)} dt}. \tag{2.36}$$

The implicit equation in (2.35) can be solved using a suitable numerical method for a known $m(\tilde{x}, t)$. The solution for constant $\hat{\mu} = 1$, when $m = 1$, is given in Stokes et al. (2011*b*). The method for obtaining these equations using the harmonic mean of viscosity $m(\tilde{x}, t)$ is discussed in greater detail in Tronnolone (2016), and only the essential equations are described in this thesis for completeness. However, when the viscosity $\hat{\mu}(x, t)$ changes

with each cross-section, the harmonic mean cannot be computed a priori for a given $\tilde{x}$ and a numerical method must be used to generate the solutions. The numerical method developed in Section 2.3.2 is adopted by using the reduced time variable to incorporate the viscosity $\hat{\mu}(x,t)$ into the problem.

The transverse flow problem is scaled with χ and therefore remains a unit circle and thus $\tilde{\Gamma} = 2\sqrt{\pi}$. Substituting for $\tilde{\Gamma}$ in (2.24) and with a little rearrangement gives the exact solution for $\chi(\tilde{x},\tau)$ as:

$$\chi(\tilde{x},\tau) = \exp\left(\frac{\sqrt{\pi}\tau}{6}\right)\left(\chi(\tilde{x},0) - \frac{6\hat{F}}{\hat{\gamma}\sqrt{\pi}}\right) + \frac{6\hat{F}}{\hat{\gamma}\sqrt{\pi}}. \tag{2.37}$$

which yields the cross-sectional area of the fluid geometry. To relate τ and t and generate the solution to a given draw time t_K, we use the relationship between t and τ in (2.18). The following algorithm describes the procedure for generating the numerical solution:

1. set the initial conditions for $\tau(\tilde{x},0), \hat{\mu}(\tilde{x},0), x(\tilde{x},0)$ and $\chi(\tilde{x},0)$;

2. compute $\tau_{j,k+1}$ using finite differencing as in (2.30), for all the cross-sections $\tilde{x}_j$, where $j = 0,1,\ldots,J$;

3. solve for $\chi(\tilde{x}_j, t_{k+1})$ using (2.37) for the calculated $\tau(\tilde{x_j}, t_{k+1})$ for all the cross-sections $\tilde{x}_j$, where $j = 0,1,\ldots,J$;

4. compute $x_{j+1,k+1}$ using (2.31) for $j = 0,1,\ldots,,J-1$;

5. update the viscosity i.e. $\hat{\mu}_{j,k+1} = \hat{\mu}(x_{j,k+1}, t_{k+1})$,

The time step is then incremented and this procedure repeated through to the final draw time t_K. This completes the solution and gives the geometry with respect to time.

The numerical solution for a solid rod is less complicated since no system of differential equations needs to be solved due to the existence of an analytical expression for χ. The evolution of the outer walls of the emitter can be determined using the expression $R(x,t) = \chi(x,t)/\sqrt{\pi}$, where χ^2 is the cross-sectional area of the glass rod. Notably, this demonstrates the use of reduced time τ to generate a full solution to this problem, without having to consider the other transverse flow variables. Additionally, if the form of each solution is considered, it is apparent that the solution with respect to τ produces an explicit solution for the evolution of the cross-section, while the solution with respect to time t produces only an implicit solution that cannot be solved completely for a viscosity that varies in space or time. Additionally, it is useful to highlight, as is also mentioned in Tronnolone (2016), that with the solution for χ in (2.37), the relationship between τ and t and the harmonic mean of viscosity is

$$\frac{6}{\sqrt{\pi}}\left(\chi(\tilde{x},\tau) - \chi(\tilde{x},0)\right) + \frac{6\hat{F}\tau}{\hat{\gamma}\sqrt{\pi}} = \frac{\hat{\gamma}t}{m(\tilde{x},t)}. \tag{2.38}$$

For a given $\chi(\tilde{x},\tau)$, (2.38) can be used to find t using the harmonic mean of viscosity.

2.4 Summary

This chapter describes the development of an extensional flow model suitable for the unsteady drawing of glass capillaries with annular cross-section. The model is composed of a 2D free boundary Stokes flow problem that describes the evolution of the flow and geometry in the cross-section and a 1D axial stretching problem. Throughout the heating and pulling process, we have investigated the geometry deformations due to non-zero surface tension, active channel pressurisation, and piecewise constant viscosity in space.

The key ideas of this chapter include:

- Development of a three-dimensional asymptotic model for the unsteady stretching of an axi-symmetrical glass tube pulled with a constant force, considering the effects of surface tension, pressure and spatially-varying viscosity. Along with the slenderness approximation, the full three dimensional model decomposes into two models:

    1. A one dimensional axial model that describes the thinning of the cross-sectional area $\chi^2(\tilde{x}, t)$ of the capillary (labelled by its initial axial position) due to unsteady pulling with a constant force and spatially varying viscosity effects.

    2. A two-dimensional cross-plane model that governs the shape of each cross-section, considering the deformations due to the surface tension (constant), pressure and viscosity effects.

- As explained in Chen et al. (2015) for steady fibre drawing, for unsteady fibre drawing including channel pressure couples the axial and cross-plane flow models which are required to be solved simultaneously.

- The model enables investigation of the effects of:

    1. Surface tension - resulting in closure of the inner channel.

    2. Time and spatially varying viscosity

    3. Constant channel pressurisation - keeping the inner channel held open during the heating and pulling process. We aim to find a balance of the parameters to stop hole closure as the cross-sectional area reduces due to stretching.

Additionally, the second half of this chapter explains the numerical approach used to solve the mathematical model developed in Section 2.2.4 for determining the evolution of the geometry accounting for the previous history of the flow.

For the sake of simplicity, the solutions derived from the numerical approach in this chapter are for a piece-wise constant viscosity in space. In the following chapter, we consider more complicated viscosity profiles by choosing a viscosity function that varies within the heated region. This allows us to focus on the fact that cross-sections cool away from the centre where they are heated.

In conclusion, the analysis of the present chapter has demonstrated that using the mathematical model and the numerical solutions developed using the time stepping procedure provides a significant insight into unsteady stretching of heated glass tubes. The numerical method developed in this chapter is further used in the subsequent chapters of this thesis to examine the various aspects of the model on the heat and draw process.

Chapter 3

Flow with significant surface tension

3.1 Introduction

A significant aspect of this study is the investigation of the impact of various material and operational parameters on the heating and pulling of a glass tube. In particular, quantifying the role of surface tension and pressure in the deformation of geometry is a key focus of this work. In Chapter 2, our preliminary analysis of the heating and pulling method with pressure in the inner channel, identified force ($\hat{F}$), pressure ($\hat{P}$), and surface tension ($\hat{\gamma}$) as the three major parameters that explain the evolution of the geometry. In terms of the application covered in this thesis, we always have a strong, constant force pulling the glass tube, which is always assumed to be significant and non-negligible. Thus, we focus our analysis on the remaining two elements. In this Chapter we assume a significant/non-negligible surface tension effect in comparison with the pressure; and then in Chapter 4 we assume significant/non-negligible pressure effect in comparison with the surface tension ($\frac{\hat{\gamma}}{\hat{P}} \ll 1$). Both problems can be described with very similar models, which scale slightly differently when the cross-plane model is formulated. For both cases,

analytical solutions are not possible due to the non-linearity of the equations, and so numerical solutions will be generated with slight variations in the method of Chapter 2.

The term 'surface tension' refers to a property of a fluid that quantifies its resistance to an external force due to molecular cohesion. The chemical composition of the surrounding atmosphere is thought to influence the interactions of the liquid molecules, resulting in changes in surface tension. It has the effect of reshaping a free surface to reduce its surface area. This is equivalent to minimising the surface's curvature or total energy. The normal force acting on the boundary is proportional to its curvature due to the surface tension, which means that a more curved boundary results in a stronger force acting upon it. In the problems considered in this thesis, in addition to stretching, surface tension determines the extent to which the external and internal radii of a tube collapses. Using this knowledge, pressure may be required to prevent closure of the internal channel (Wadsworth et al. 2005, Chen et al. 2015). Additionally, surface tension may vary with temperature, i.e., it decreases with increasing temperature (Stokes et al. 2019). However, for glass, surface tension is only weakly dependent on temperature and for the purpose of this thesis, we assume it is constant.

In the literature, surface tension is often treated as negligible in the analysis of the fibre glass drawing process. Wylie et al. (2011) investigated the problem of the pulling of an axisymmetric viscous thread by its ends with a fixed force for small inertia and surface tension forces. They suggested that the effect of surface tension is negligible and becomes unimportant as the thread is stretched. However, Tronnolone (2016) demonstrated that experimentally observed deformations in stretched fibre geometries could be explained by the effects of surface tension and, more importantly that the effects of surface tension depend on the choice of dimensionless parameters and the geometry under consideration. Luzi et al. (2010) focused on the effect of both surface tension and internal hole pressure in

Description	Symbol	Value	SI unit
Initial length	L_0	$\sim 5 \times 10^{-3}$	m
Surface tension	γ	0.3	N/m
Minimum viscosity	μ_{hot}	10^4	Pa s
Density	ρ	2200	kg/m^3
Initial external radius	R_0	6×10^{-5}	m
Initial aspect ratio	ϕ_0	0.06	-
Initial cross sectional area	S_0	1×10^{-8}	m^2
Heated length	H	$\sim 3 \times 10^{-3}$	m
Pressure	P	To be determined	Pa
Force	F	To be determined	N
Final draw time	t_K	To be determined	s

Table 3.1: Physical parameters relevant to manufacture of emitters.

steady fibre drawing with comparison to experiments. They showed during the stretching process the internal and external diameters of the fibre decrease in value due to the effects of surface tension and the use of internal hole pressurisation to counteract its effects.

3.2 Numerical solutions for non-zero pressure

We perform numerical simulations in the first half of this chapter using the flow model defined in Chapter 2 under the assumption that the impact of surface tension is significant during fibre stretching and thus acts to close the internal channel, possibly requiring the use of pressure to overcome surface tension and to keep the hole open.

The glass tube in our axisymmetric stretching problem is presumed to be stationary at $t = 0$ and we choose the velocity scale U as a characteristic velocity that balances the surface tension and viscous stress by choosing the dimensionless surface tension parameter $\hat{\gamma} = 1$, which yields $U = \gamma H/\mu_{hot}\sqrt{S}$. Substituting for U in (2.4), the scaled variables

(denoted by hats) are

$$(u, v) = \frac{\gamma H}{\mu_{hot}\sqrt{S_0}}(\hat{u}, \epsilon\hat{v}), \quad t = \frac{\mu_{hot}\sqrt{S_0}}{\gamma}\,\hat{t}, \quad p = \frac{\gamma}{\sqrt{S_0}}\,\hat{p},$$
$$F = 6\sqrt{S_0}\gamma\,\hat{F}, \quad P = \frac{\gamma}{\sqrt{S_0}}\hat{P}. \tag{3.1}$$

Typical values of the physical parameters are given in Table 3.1, from which, the axial velocity scale $\gamma H/\mu_{hot}\sqrt{S_0} \approx 0.1 - 1\text{mm/s}$ which is reasonable for emitter fabrication. We solve for this flow numerically using the system of equations (2.25), (2.20), (2.18), and (2.13) along with (2.22) and (2.23) that solve for the external and internal radii of the tube. The assumption of setting $\hat{\gamma} = 1$ enables us to explore the effects of $\hat{F}$, $\hat{P}$ on the geometry relative to non-negligible surface tension and determine the t_K required to get the final geometry with the required dimensions.

In the numerical solutions in Chapter 2, we assumed that the viscosity is piecewise constant. However, the viscosity of glass is highly temperature sensitive and so we now assume a more physically realistic viscosity profile. The viscosity is expected to vary axially over the heated region, attaining its minimum dimensionless value $\hat{\mu} = 1$ at the centre of the heated region, $x = 0$, where the temperature is hottest, and increasing with distance from the centre. At the end of the heated region, $x = 1$, the glass will have cooled sufficiently such that it is, effectively, solid with a dimensionless viscosity $\hat{\mu}_{cold} \gg 1$ and we may take this as the viscosity for $x \geq 1$. We also assume the viscosity is independent of time for the pull time $0 \leq t \leq t_K$. Hence, to illustrate the inclusion of a spatially varying temperature in this chapter, we propose a spatially varying viscosity function defined by

$$\hat{\mu}(x) = \begin{cases} 1 + (\mu_{cold} - 1)|x|^n, & 0 \leq x < 1, \\ \mu_{cold}, & x \geq 1, \end{cases} \tag{3.2}$$

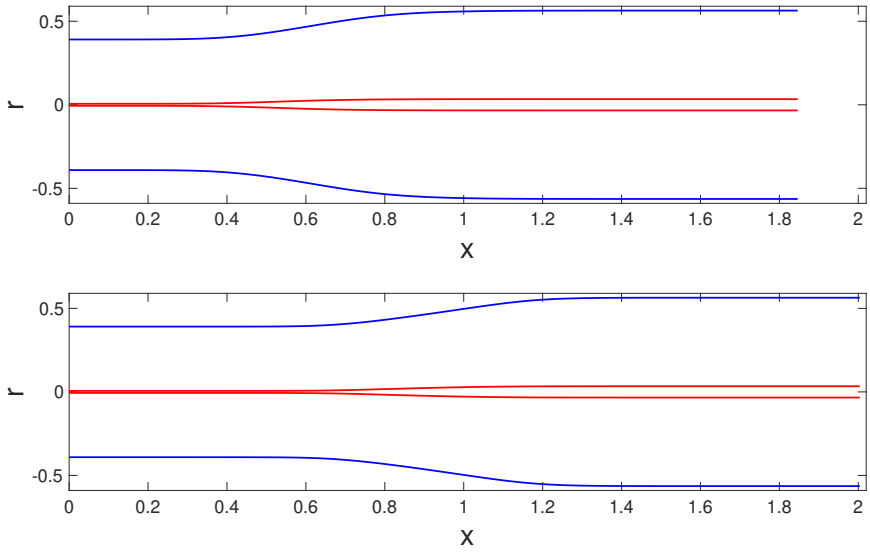

Figure 3.1: Emitters obtained from an axisymmetric tube with initial length $L(0) = 1.5$, cross-sectional area $\chi^2(x, 0) = 1$ and aspect ratio $\phi(x, 0) = 0.06$, by pulling with force $\hat{F} = 2$ and pressure $\hat{P} = 32$ for time $t_K = 0.15$. On top is the geometry obtained with the viscosity profile (3.2) with $n = 6$ and below is obtained with the viscosity profile that for $n = 12$. The outer boundary $r = R(x, t_K)$ is shown in blue and the inner channel $r = \phi(x, t_K)R(x, t_K)$ is shown in red for both figures.

where n is a positive integer that permits modification of the rate of increase of the viscosity with x. The larger the value of n, the more uniform the viscosity in the vicinity of $x = 0$ and the more rapid the viscosity rise near $x = 1$ which in turn, should lead to an extended taper compared to a profile with lower n. As in (2.33), we take $\hat{\mu}_{cold} = 100$.

Figure 3.1 compares the shape of an emitter of initial aspect ratio $\phi_0 = 0.06$, initial (dimensionless) length $L_0 = 1.5$ pulled with $\hat{F} = 2$, and $\hat{P} = 32$, until $t_K = 0.15$ using the viscosity profile in (3.2) when $n = 6$ and $n = 12$ respectively. These solutions illustrate how the geometry changes with the choice of n, and that the viscosity profile affects the final geometry. For example, we may choose $n = 12$ if we require an extended taper length. Note that changing n has no effect on the radial dimensions of the geometry and

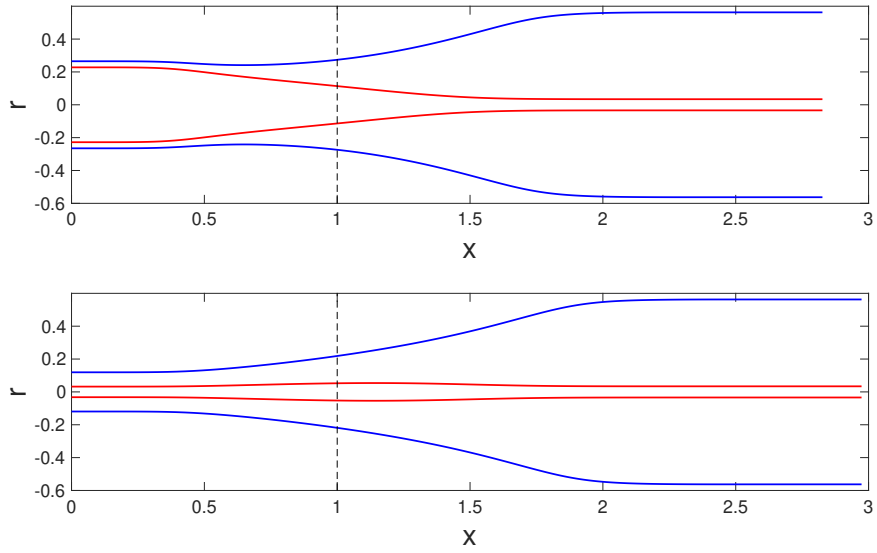

Figure 3.2: The geometry of the emitter obtained by pulling an axisymmetric tube with initial length of $L(0) = 1.5$, cross-sectional area $\chi^2(x, 0) = 1$, and aspect ratio $\phi(x, 0) = 0.06$ with a force $\hat{F} = 1.32$ for a time $t_K = 0.44$ at two different pressure values. On top is the geometry for pressure $\hat{P} = 34.217$ and below is for $\hat{P} = 34$. The outer boundary $r = R(x, t_K)$ is shown in blue and the inner channel $r = \phi(x, t_K)R(x, t_K)$ is shown in red for both figures.

will only lead to a different taper length. In the rest of this thesis, unless appropriate temperature modelling is used to determine viscosity as a function of temperature in Chapter 5, we take (3.2) with $n = 6$ as the viscosity profile. Comparing the taper of Figure 2.5 obtained using the piecewise constant viscosity function (2.33) with that of Figure 3.1, obtained with the more realistic viscosity function (all other parameters being the same), the result with piecewise constant viscosity results in a longer taper with a uniform tubular geometry over the heated length $0 \leq x \leq 1$. The shape of the resulting geometry for the continuous function is an hourglass shape, showing the effect of the axially varying viscosity profile on the deformation process.

Figure 3.2 compares the geometry obtained with a relatively high pressure $\hat{P} = 34.217$,

resulting in aspect ratio of $\phi \approx 0.8605$ at $x = 0$, with a slightly lower pressure $\hat{P} = 34$. For both pressures the viscosity is given by (3.2). For $\hat{P} = 34.217$, the internal channel radius increases as $x \to 0$ and for a pressure only a little larger, the tube will burst at $x = 0$, i.e. the inner channel radius equals the outer radius ($\phi = 1$), and the wall thickness (radius of outer wall - radius of inner wall) goes to zero. As discussed earlier, it is desirable to produce emitters for mass spectrometry with a (nearly) constant bore and with a sharp tip such that the wall thickness at $x = 0$ is small. It is apparent that the outcome is highly sensitive to the choice of channel pressure $\hat{P}$, with the capillary nearly bursting at $\hat{P} = 34.217$ but not at $\hat{P} = 34$ when $\hat{F} = 1.32$. Recall that this indicates that we are looking for parameters close to the limiting case of bursting, where the solution is extremely sensitive to small changes in the parameter values, which makes this a rather difficult task.

3.2.1 Achieving a uniform bore

The model we have developed can be used to predict the final geometry of an emitter when it is pulled from a known glass tube using a set of known draw parameters and, conversely, to predict the draw parameters required to achieve a desired final geometry when pulling from a known glass tube. This section considers and explores how to determine suitable draw parameters so that an emitter with a uniform bore can be achieved.

To begin with, our goal is to reduce the external radius of the tube to a sharp tip during the heating and pulling process while retaining a uniform internal channel and achieving a small wall thickness, namely W_T (non-dimensional) at the tip. We first define some of the terms we need in our dimensionless model. They are: $\phi_T = \phi(0, t_K)$ and $\chi_T^2 = \chi^2(0, t_K)$ as the aspect ratio and cross-sectional area at position $x = \tilde{x} = 0$ (at the tip) at the final draw time t_K, from which the external radius $R_T = R(0, t_K)$ can be readily determined.

The initial external radius of the tube at the tip is defined as $R_0 = R(0,0)$, which is the initial radius of the entire tube. The requirement of the outer radius of the tube at the tip in terms of the required wall thickness is

$$R_T = W_T + \phi_0 R_0, \tag{3.3}$$

and the requirement of the inner radius at the tip is $\phi_T R_T = \phi_0 R_0$ (same as initial) or more precisely $\phi(0,t_K)R(0,t_K) = \phi(0,0)R(0,0)$. The aspect ratio at the tip can be determined in terms of the wall thickness as:

$$\phi_T = \frac{\phi_0 R_0}{R_T} = \left\{1 + \frac{W_T}{\phi_0 R_0}\right\}^{-1} = \left\{1 + W_T\sqrt{\pi\left(\frac{1}{\phi_0^2} - 1\right)}\right\}^{-1}, \tag{3.4}$$

along with

$$\chi_T^2 = \pi(R_T^2 - \phi_0^2 R_0^2) = \pi W_T(W_T + 2\phi_0 R_0), \tag{3.5}$$

which determines the cross-sectional area at the tip. Thus, a desired W_T can be achieved by specifying the χ_T and ϕ_T corresponding to the desired geometry. In the ongoing analysis, for our illustrative problem, we select $\chi_0 R_T = 12\,\mu$m and $\phi_T\chi_0 R_T \approx 3.6\,\mu$m resulting in a wall thickness at the tip of $\chi_0 W_T = 4.2\,\mu$m which correspond to $\chi_T = 0.1911$ and $\phi_T = 0.3$ in our dimensionless problem. The dimensions of the initial tube are $R_0 = 60\,\mu$m and $\phi_0 = 0.06$ as given in Table 3.1.

We must now determine the required $\hat{F}$, pressure $\hat{P}$ and a pulling time t_K that results in the desired ϕ_T, that satisfies the requirement of W_T. Since we are seeking a geometry near to the limiting cases such as of bursting ($\phi \to 1$), breaking ($\chi \to 0$) and inner channel closure ($\phi \to 0$), the numerical analysis must be done with care.

To aid understanding, we show a number of phase plane plots in figure 3.3 for a tube

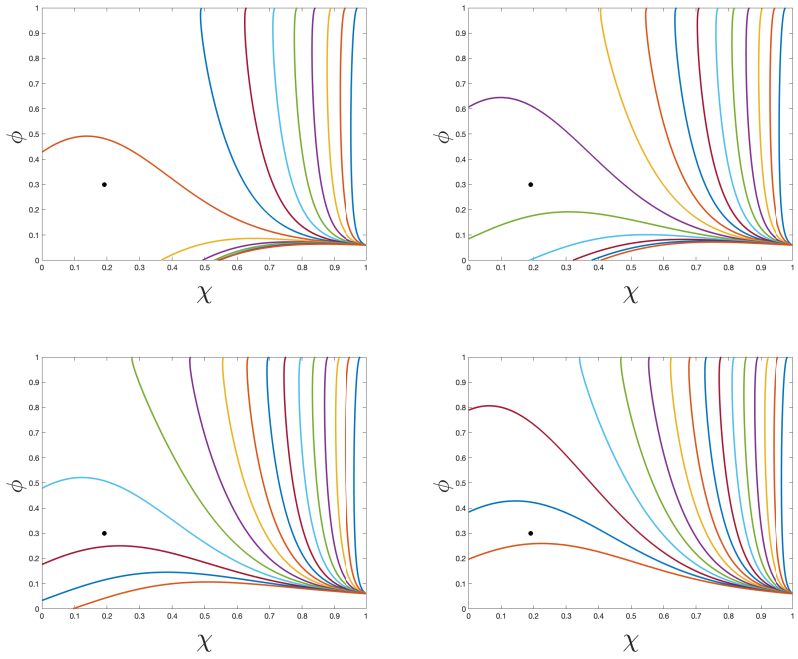

Figure 3.3: $\phi(\tau)$ versus $\chi(\tau)$ for a capillary with initial aspect ratio $\phi_0 = 0.06$. Pulling with pressure $\hat{P} = 34$ (top left), 35 (top right), 36 (bottom left), 37 (bottom right) for a force $\hat{F}$ ranging from 0.5 to 2 in increments of 0.1 increasing from top right to bottom. The black dot is at $(\chi_T, \phi_T = 0.1911, 0.3)$ corresponding to the final emitter geometry at $x = 0$.

with initial aspect ratio $\phi_0 = 0.06$, hence (dimensionless) external radius $R_0 = 0.5652$ (unit cross-sectional area). Each plot is for a different value of pressure $\hat{P}$. Each of the curves in a plot corresponds to a different pulling force $\hat{F}$ and shows how the geometry (χ, ϕ) of the cross-section at $x = \tilde{x} = 0$ changes as τ (and hence t) increases, where $(\chi, \phi) = (1, \phi_0)$ at $t = \tau = 0$. Each curve stops at one of the boundaries within the physically meaningful region $0 < \chi < 1$ and $0 < \phi < 1$. Note that, strictly $\chi > 1$ is physically possible with suitable parameters but it is not of interest in emitter manufacture and so is excluded. These plots show that there are multiple choices of $\hat{P}$, $\hat{F}$ and τ_K that will yield a desired final geometry (χ_T, ϕ_T), shown using a black dot. The wall thickness of the emitter can

be determined from $(\chi_T, \phi_T) = (0.1911, 0.3)$, and this corresponds to $R_T = 0.1130$ and $\phi_T R_T = \phi_0 R_0 = 0.0339$, i.e. the internal radius at $x = 0$ equals that of the initial tube.

Proceeding further, we now aim to develop a procedure that helps us to determine the value of $\hat{F}$ that generates the desired χ_T and ϕ_T for a given $\hat{P}$. For this we develop a root finding procedure that determines the appropriate force $\hat{F}$ for a pressure $\hat{P}$ that yields the prescribed (χ_T, ϕ_T) at the tip. The algorithm is as follows,

1. set a pressure $\hat{P}$ value;
2. set an initial range for $\hat{F}$ as a guess;
3. solve (2.20) and (2.25) in MATLAB with `ode45` for a large τ span;
4. use the function `fzero` in MATLAB to calculate the $\hat{F}$ that generates the desired ϕ_T at the tip;
5. define `events` in MATLAB ODE solver to stop computations beyond the χ_T value corresponding to the final geometry at the tip.

Additionally, we define `events` in the MATLAB ODE solver to stop the solution should $\phi = 0$, $\phi = 1$, or $\chi = 0$. We can also include $\phi_T R_T - \phi_0 R_0 = 0$ as an `event` in place of specifying χ_T as a stopping criterion to ensure that the inner channel at the tip has the same dimension as the original tube.

From the phase plane plots it is apparent there is not necessarily a unique choice of $\hat{F}$ and $\hat{P}$ that yields a required geometry at the tip ($x = 0$). The evolution of the geometry is unique from one solution to another which affects the final geometry of the cross-sections for $x > 0$ and, so the shape of the emitter. We seek an emitter with a constant bore, so after determining values of $\hat{P}$ and $\hat{F}$ that give the desired χ_T and ϕ_T, we look for

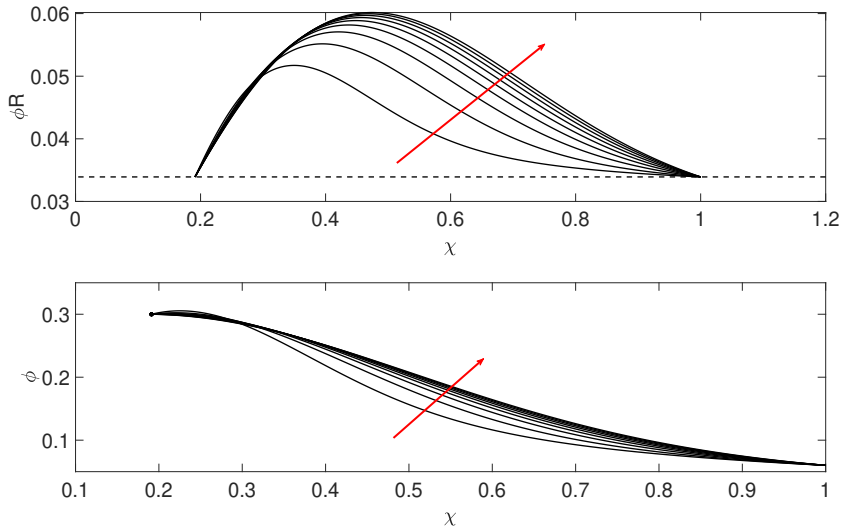

Figure 3.4: Plot of the inner boundary $r = \phi(\tau)R(\tau)$ (top) and the aspect ratio $\phi(\tau)$ (bottom) as a function of $\chi \in [\chi, 1]$ for different pressure values within the range $\hat{P} = 32 - 40$ in increments of 1. The value of the force $\hat{F}$ is determined from the algorithm above, to reach the desired (χ_T, ϕ_T). The red arrow shows the direction of increasing pressure (and force). The black dashed line in ϕR versus χ plot shows the initial inner radius (when $\chi = 1$) which is also the radius when $\chi = \chi_T = 0.1911$. The black dot in the ϕ versus χ plot corresponds to $(\chi_T, \phi_T) = (0.1911, 0.3)$.

the best choice of these parameters corresponding to the most uniform bore. To do this, the algorithm above is used to compute over a range of pressure values and the optimal solution is then selected as the parameter combination $(\hat{F}, \hat{P})$ that gives the least variation along the length of the inner channel from its original dimension, that is the smallest value

$$E = \text{ maximum } (\phi(\tau)R(\tau)) - \phi_0 R_0. \tag{3.6}$$

Figure 3.4, shows the internal radius ϕR (top) and aspect ratio ϕ (bottom) against $\chi \in [\chi_T, 1]$ for a number of different parameter combinations $\hat{P}$, and $\hat{F}$. These graphs show the change of the internal radius and the aspect ratio as the cross-sectional area reduces from $\chi^2 = 1$. Every cross-section will follow the curve corresponding to the

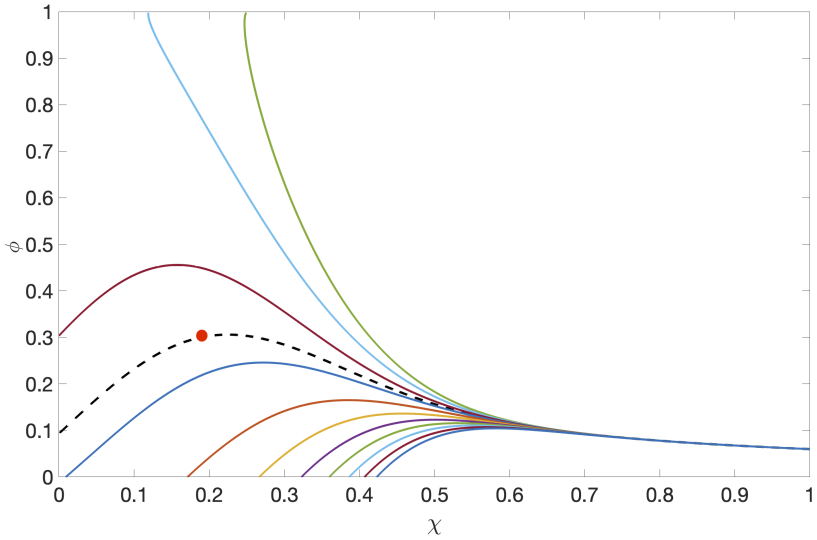

Figure 3.5: Curves $(\chi_T(\tau), \phi_T(\tau))$ for $\hat{P} = 32$ and (solid curves) $0.64102 < \hat{F} < 0.64103$ in increments of 10^{-6}, with $\hat{F}$ increasing from the top curve to the bottom curve. Initially $(\chi(0), \phi(0)) = (1, 0.06)$ and τ increases from right to left. The red dot shows the desired geometry $(\chi_T, \phi_T) \approx (0.1911, 0.3)$ at the tip $x = 0$. The black dashed-curve passing through the red dot corresponds to a force of $\hat{F} = 0.64102262$.

chosen parameters $\hat{P}$, $\hat{F}$, though only that at $x = 0$ will reach the end point $\chi = \chi_T$, specified by the stopping criterion. Of the curves shown, the curve with least variation of the inner channel is given by $(\hat{P}, \hat{F}) = (32, 0.64102262)$. With the final value of τ_I known as an output from the ODE solver, we can use (2.18) to determine the corresponding t_K, the physical time taken for the emitter to be pulled given a known $\hat{\mu}(x, t)$.

Although Figure 3.4 (top) suggests that the variation in the inner channel radius decreases with decreasing pressure (and pulling force), there is a lower limit for a practically feasible outcome. Consider Figure 3.5 showing curves (χ, ϕ) for pressure $\hat{P} = 32$ and different values of force $\hat{F}$ to which ϕ is highly sensitive. To achieve the desired geometry (χ_T, ϕ_T) at the tip (red dot through which the black dashed line passes) a force $\hat{F} = 0.64102262$ is required. For the same χ_T, a small change in the force results in a

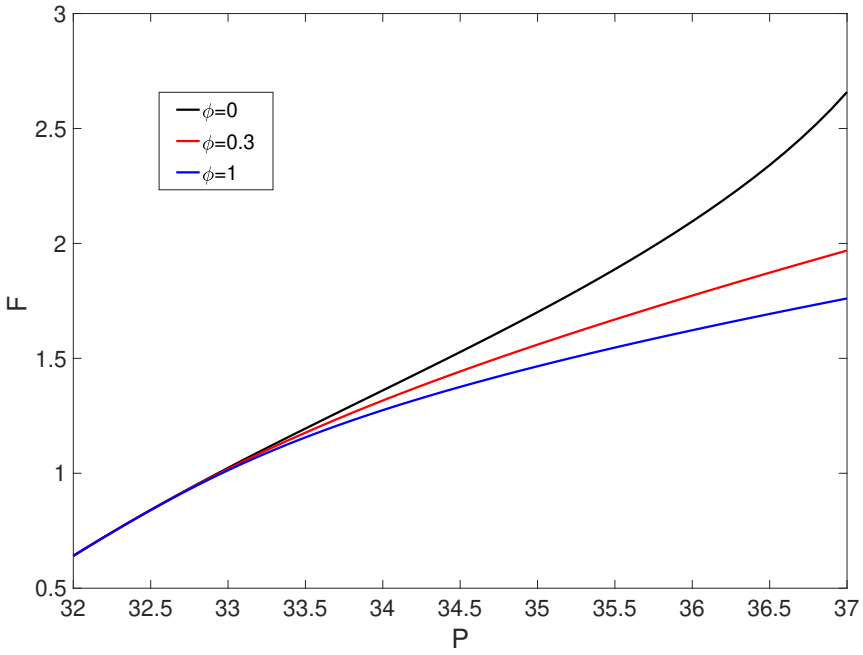

Figure 3.6: Pulling force $\hat{F}$ versus pressure $\hat{P}$ that enable the manufacture of emitters with $\chi_T = 0.1911$, and $\phi_T = 0$ (black), $\phi_T = 0.3$ (red) and $\phi_T = 1$ (blue), from a tube with initial geometry $(\chi_0, \phi_0 = 1, 0.06)$.

significant change in ϕ_T. The tube bursts ($\phi = 1$) for a slightly smaller force in the range $0.641020 < \hat{F} < 0.641021$, and the channel closes ($\phi = 0$) for slightly larger force in the range $0.641023 < \hat{F} < 0.641024$. Seven figure accuracy in the force cannot be practically achieved, so this suggests that a parameter regime with less sensitivity to small changes should be used so that the desired geometry at the tip can be assured within reasonable tolerances.

Figure 3.6 shows, the curves $(\hat{P}, \hat{F})$ corresponding to $(\chi_T, \phi_T) = (0.1911, 0.3)$ from a tube with initial geometry $(\chi, \phi) = (1, 0.06)$. Above this is shown, in black, the curve on which $(\chi_T, \phi_T) = (0.1911, 0)$ and the channel closes at $x = 0$, while below is shown, in blue, the curve on which $(\chi_T, \phi_T) = (0.1911, 1)$ and the tube bursts at $x = 0$. To obtain a valid emitter tip, even if not the desired geometry, values of $\hat{P}$ and $\hat{F}$ must be

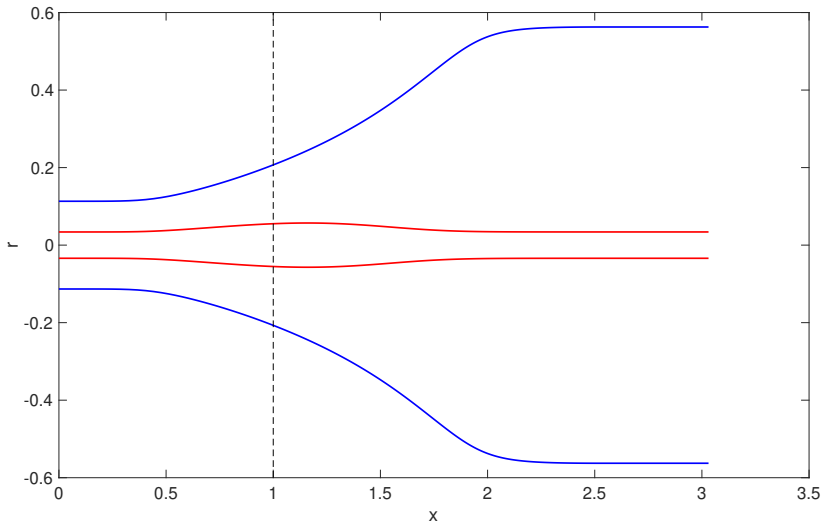

Figure 3.7: Plot of the final emitter geometry for a tube with initial length $L(0) = 1.5$, cross-sectional area $\chi^2(x,0) = 1$, and aspect ratio $\phi(x,0) = 0.06$, after pulling for a time $t_K = 0.4436$ with force $\hat{F} = 1.3166$ while applying an internal channel pressure $\hat{P} = 34$. The external boundary $r = R(x,t_K)$ is shown in blue and the internal boundary $r = R(x,t_K)\phi(x,t_K)$ is shown in red. The aspect ratio and cross-sectional area at the tip are $\phi_T = 0.3$, $\chi_T = 0.1914$.

chosen from the region between upper and lower curves. This figure clearly shows the sensitivity of ϕ_T to the force $\hat{F}$ for smaller pressure $\hat{P}$, and the decrease in sensitivity as $\hat{P}$ increases. However, while choosing a larger pressure and force means less sensitivity of the tip geometry to inaccuracies in the parameters, it must be remembered that as $\hat{P}$ increases the variation of the inner channel radius increases, and a larger bulge is seen; see Figure 3.4 (top). We conclude that the optimal choice of the parameters $\hat{P}$, $\hat{F}$ corresponds to the point on the red curve with smallest $\hat{P}$ such that variations within the tolerance range of the pulling device lead to acceptable variation in the geometry at $x = 0$. This will yield the emitter with the most uniform internal channel radius (smallest bulge) possible.

Figures 3.3 - 3.6 show the required solution of χ and ϕ as functions of independent variable τ. The analysis did not require knowledge of viscosity $\hat{\mu}(x,t)$ and the calculation

of axial position x as the use of reduced time alone is sufficient to determine a feasible parameter regime for the outcome. To determine the evolution of the physical geometry over physical time t for a prescribed viscosity function $\hat{\mu}(x,t)$, the movement of each cross-section must be tracked relative to the location of the heater. This determines the viscosity at each cross-section, which is not considered in the root finding algorithm described above. For this we run the full numerical procedure of Section 2.3.2 starting with an approximation (guess) for the final time t_K. We use a constrained τ span with $\tau \in [0, \tau_I]$, where τ_I corresponds to the value of τ from the above root finding technique that gives the desired (χ_T, ϕ_T) for the cross-section at $x = 0$. The final draw time t_K may then be adjusted to meet the τ_I requirement, i.e. that $\tau(x = 0, t = t_K) = \tau_i$. Figure 3.7 shows the shape of the glass emitter for a parameter choice which gives relatively little variation in the inner channel, namely $\hat{P} = 34$ and $\hat{F} = 1.3166$. Note here that the dimension of the inner channel at the tip is equal to that at the pulled end at the final time $t_K = 0.4436$. The solutions are plotted in dimensionless form, and can be converted back to dimensional form using the scales in (3.1). For example, in dimensional form, recall that the axial length scale is $\sim 3\,\text{mm}$ while the radial length scale is $0.1\,\text{mm}$ implying that the variations in the radius are relatively small in comparison to the variation in the axial length.

3.3 Zero channel pressure: a semi-analytical solution

The case of zero channel pressure in a surface tension-driven flow with constant pulling force is discussed in detail in both Stokes et al. (2014) and Tronnolone (2016). We will highlight the main findings relevant to our unsteady analysis for completeness. In this

case, the deformations within a cross-section are entirely due to the effect of surface tension, which is determined by the curvature (κ) of the channel. The significance of this analysis is that it provides a semi-analytical solution to the flow model in terms of τ that can be used to validate the numerical solution.

The system of differential equations in (2.20) and (2.24) for non-zero pressure, does not have an analytical solution. However, in the absence of pressure ($\hat{P} = 0$) (2.24) decouples from (2.20) and we can solve (2.20) for $\phi(\tau)$ analytically. This solution can then be used to determine $\chi(\tau)$ in (2.24). Further simplifications can be applied to obtain a semi-analytical form of the solutions to the zero-pressure case, which are helpful for verifying the accuracy of the numerical solutions here. This also provides a useful basis for understanding the underlying mechanisms of when and why channel pressurisation is important. To generate solutions for the case where $\hat{P} = 0$, we begin by defining an additional parameter α, which was introduced in Stokes et al. (2014), Chen et al. (2015) and Tronnolone (2016) to describe the geometry of the fibre cross-section, namely

$$\alpha = \sqrt{\frac{1-\phi}{\pi(1+\phi)}}, \tag{3.7}$$

where $\alpha(\tilde{x}, \tau)$ is the wall thickness (or the difference between the outer and inner radii) of cross-section $\tilde{x}$ at reduced time τ in our cross-plane model. In practice, we are more interested in ϕ, therefore, the above equation can be rearranged for ϕ to obtain

$$\phi = \frac{1-\pi\alpha^2}{1+\pi\alpha^2}. \tag{3.8}$$

Thus, the equations (2.24) and (2.20) (with $\hat{P} = 0$) in terms of α are

$$\frac{d\chi}{d\tau} = \frac{1}{6}\chi - \frac{\hat{F}}{\hat{\gamma}}, \tag{3.9}$$

$$\frac{d\alpha}{d\tau} = \frac{1}{2}. \tag{3.10}$$

As in Stokes et al. (2014) and Tronnolone et al. (2016) the solution is readily found to be

$$\alpha(\tilde{x}, \tau) = \alpha_0\left(1 + \frac{\tau}{2\alpha_0}\right), \quad \text{where } \alpha_0 = \alpha(0), \tag{3.11}$$

$$\chi(\tilde{x}, \tau) = \left(\frac{\alpha}{\alpha_0}\right)^{1/3}\left\{1 - 3\frac{\hat{F}}{\hat{\gamma}}\alpha_0\left[\left(\frac{\alpha}{\alpha_0}\right)^{2/3} - 1\right]\right\}, \tag{3.12}$$

$$\phi(\tilde{x}, \tau) = \frac{1 - \pi\alpha^2}{1 + \pi\alpha^2}, \tag{3.13}$$

which replace the numerical solution of χ and ϕ in the algorithm of Chapter 2 (page 34). The expression for the outer radius $R(\tilde{x}, \tau)$ can be computed using (3.11) as

$$R = \frac{\chi\alpha_0}{(1 - \phi)}\left(1 + \frac{\tau}{2\alpha_0}\right). \tag{3.14}$$

Hence the inner radius $\phi(\tilde{x}, \tau)R(\tilde{x}, \tau)$ at any τ is

$$\phi R = \chi\alpha_0\left(1 + \frac{\tau}{2\alpha_0}\right)\left(\frac{1 - \pi\alpha^2}{1 + \pi\alpha^2}\right). \tag{3.15}$$

As discussed earlier, a number of `events` are possible during the pulling process, depending on the problem parameters. In the case of zero pressure, for which ϕ necessarily decreases with τ, bursting cannot occur and exact expressions may be found for the reduced times at which hole closure and fibre breaking occur. The reduced time at which

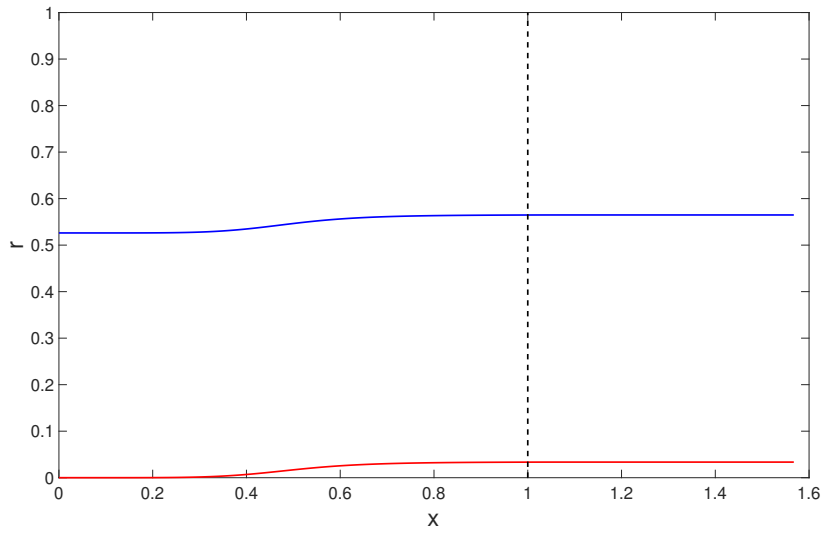

Figure 3.8: The outer boundary $r = R(x, t_K)$ (blue) and inner boundary $r = \phi(x, t_K)R(x, t_K)$ (red) over the position x after pulling from an axisymmetric fibre of initial length $L(0) = 1.5$, cross-sectional area $\chi^2(x, 0) = 1$ and aspect ratio $\phi(x, 0) = 0.06$ for a channel pressure $\hat{P} = 0$, force $\hat{F} = 1.32$, and a draw time $t_K = 0.0635$. The heated region $0 \leq x < 1$ is indicated by the black dashed line.

the internal channel closes is

$$\tau_C = 2\left(\frac{1}{\sqrt{\pi}} - \alpha_0\right), \tag{3.16}$$

at which time $\phi(\tau_C) = 0$ (or $\alpha(\tau_C) = 1/\sqrt{\pi}$), (Stokes et al. 2014). For $\tau > \tau_C$ the cross-plane model is invalid as the aspect ratio becomes negative. Therefore, beyond this point there is no longer a hole and the annular geometry must be replaced with a unit circle with no interior hole (Stokes et al. 2014), i.e. a solid rod (as discussed in Section 2.3.3). If the aim is to preserve the hole, then we will require $\tau \leq \tau_C$ for every $\tilde{x}$.

As the glass tube continues to stretch, assuming there is no hole closure, it will continue to deform as τ increases, and will eventually break at the cross-section which first reaches

the reduced time:

$$\tau_B = 2\alpha_0 \left\{ \left(1 + \frac{\hat{\gamma}}{3\hat{F}\alpha_0} \right)^{3/2} - 1 \right\}, \tag{3.17}$$

when the cross-sectional area goes to zero ($\chi^2 \to 0$).

For $\hat{P} = 0$, as the tube is heated, the viscosity of the fluid decreases rapidly and the tube lengthens and thins more rapidly, thus enhancing the effect of surface tension. When the stretching force is low, the surface tension has more time to act compared with when it is high, which results in more closure of the inner channel. More importantly, for the case of zero pressure, if we are to preserve the interior channel and avoid breakage of the tube, we will require $\tau(\tilde{x}, t) < \min(\tau_C, \tau_B)$. Once the final geometry of the tube is determined in terms of τ, for a prescribed viscosity, we can use (2.18) to find the results in terms of scaled physical time t along with the length of the tube computed using (2.12). Figure 3.8 shows an example solution for a fibre of initial aspect ratio $\phi_0 = 0.06$ pulled with a force $\hat{F} = 1.32$, channel pressure $\hat{P} = 0$, for a time $\hat{t}_K = 0.0635$ at which time the aspect ratio at $\tilde{x} = 0$ becomes zero ($\phi = 0, \tau = \tau_C = 0.0658$). The viscosity profile used was that given in (3.2) with $n = 6$. Note that the `events` in the ODE solver can be used to determine τ_C and to stop computing the solutions beyond $\phi = 0$.

3.4 Numerical convergence

For numerical convergence and the validity of the solution, both spatial and time discretisation must be sufficiently small. Most importantly the numerical solution should converge to a single solution at a given time as $\Delta\tilde{x}$ and Δt. Figure 3.9 shows the evolution of χ at $t_K = 0.4$ where $\Delta\tilde{x} = 0.1, 0.01$, and 0.001 and with $\Delta t = 0.1$, and shows convergence as $\Delta\tilde{x}$ decreases. The solutions for $\Delta\tilde{x} = 0.01$ and 0.001 compare closely to each other even under magnification, Figure 3.9 (b).

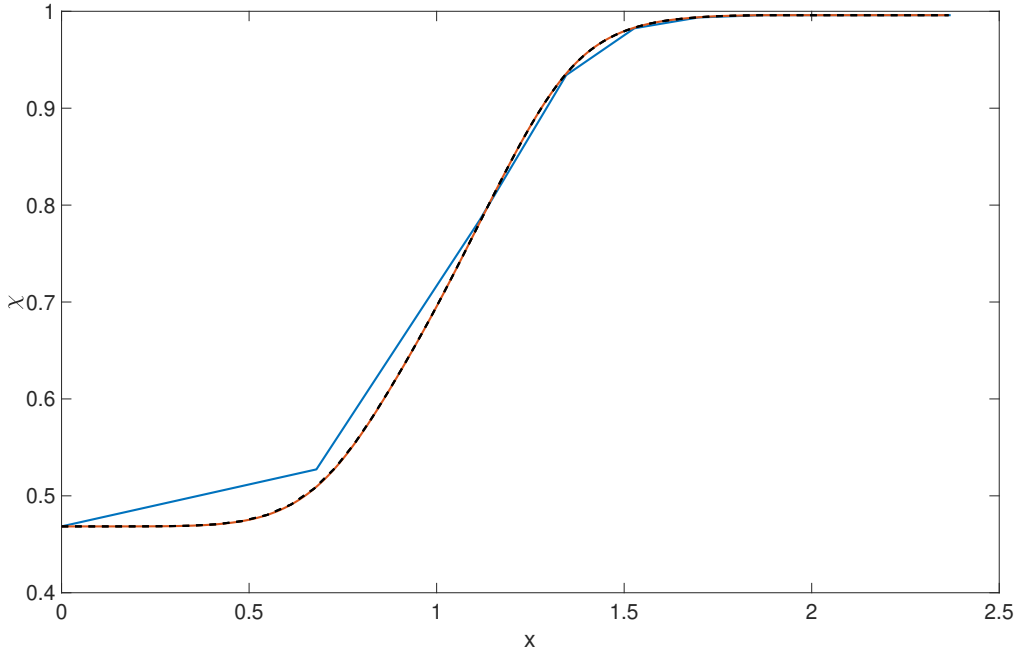

(a) χ plotted against x for $\Delta\tilde{x} = 0.1$ (blue), 0.01 (black dotted), 0.001 (orange). The initial dimensionless length of the tube is $L(0) = 1.5$, the cross-sectional area $\chi^2(x, 0) = 1$ and aspect ratio $\phi(x, 0) = 0.06$. The tube is pulled with $\hat{P} = 34$, $\hat{F} = 1.3166$, and $t_K = 0.4$, where $\Delta t = 0.1$.

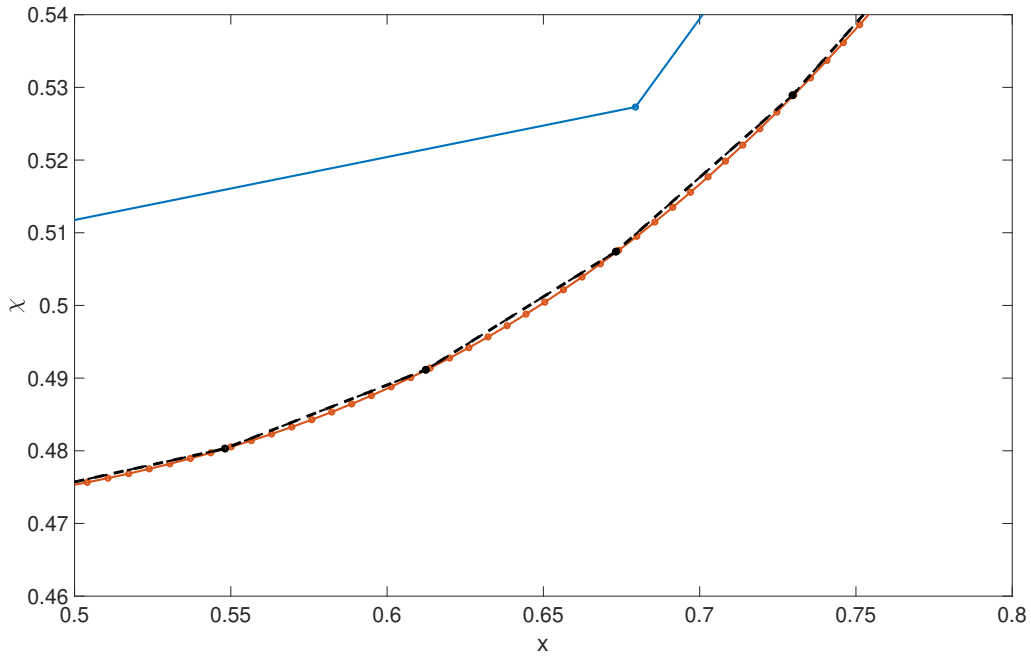

(b) A magnified image of the neck-down region from $x = 0.5$ to $x = 0.8$ of Figure 3.9 (a).

Figure 3.9: Evolution of square root of the cross-sectional area (χ) for different values of $\Delta\tilde{x}$ at time $t_K = 0.4$.

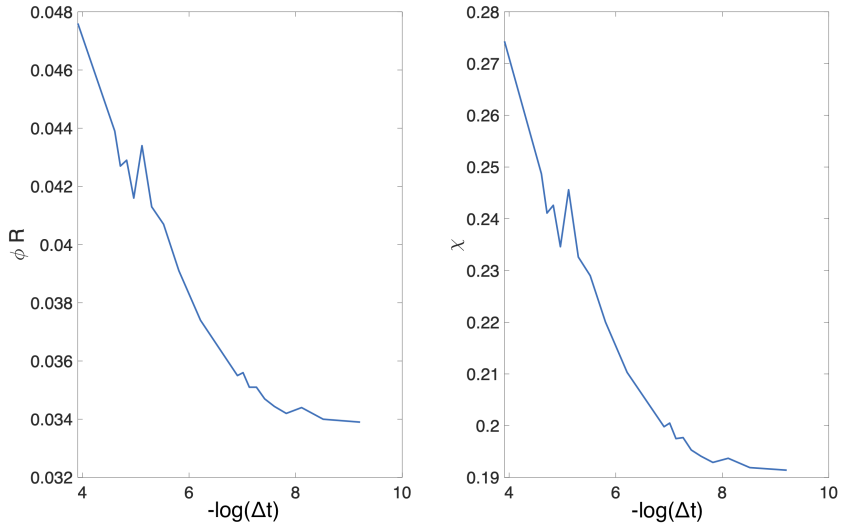

Figure 3.10: Plot of (a) inner radius $r = \phi_T R_T$ (b) χ, plotted against $-\log(\Delta t)$, where Δt is the size of the time step, and $\Delta\tilde{x} = 10^{-3}$. The initial dimensionless length of the tube is $L(0) = 1.5$, the cross-sectional area $\chi^2(x, 0) = 1$ and the aspect ratio $\phi(x, 0) = 0.06$. The tube is pulled with $\hat{P} = 34$, $\hat{F} = 1.3166$, and $t_K = 0.4436$ to achieve $\phi_T R_T = 0.0339$ and $\chi_T = 0.1911$ at the tip.

To illustrate the convergence of the numerical method with respect to the choice of Δt, Figure 3.10 shows the final inner radius $\phi_T R_T$ in (a) and χ_T in (b) versus the negative log of the time step Δt with $\Delta\tilde{x} = 0.001$. These plots show that as time step decreases, the numerical solution converges to $\phi_T R_T = 0.0339$ and $\chi_T = 0.1911$. To generate these results, we have repeated the calculation used to generate Figure 3.7 with $\Delta\tilde{x} = 10^{-3}$ and for a variety of time steps Δt.

The semi-analytical solution for zero pressure is useful to validate the interpolation step in the complete numerical solution method for non zero pressure. To test this, let us consider the result for $\phi = 0$, or $\alpha = 1/\sqrt{\pi}$, which occurs at $\tau_C = 0.0658$ and corresponds to the geometry at the tip $\tilde{x} = 0$ in Figure 3.8. Using for example, $\hat{F} = 1.32$, we can calculate analytically the resulting value of $\chi_T = 0.9325$ from (3.12). The numerical

Δt	χ_T	τ_C
0.01	0.9369	0.0616
0.001	0.9332	0.0651
0.0001	0.9326	0.0657

Table 3.2: χ_T and τ_C values at $t_K = 0.4436$ for different Δt values for zero pressure.

solutions obtained when computing the values of χ_T and τ_C (to 5 figures) for $\Delta\tilde{x} = 0.001$ with different Δt values are listed in Table 3.2 for reference. For $\Delta\tau = \Delta\tilde{x} = 10^{-3}$ and $\Delta t = 10^{-4}$ the two solutions agree to three decimal places. Thus for better accuracy (at least 5 figure accuracy) we need small time steps and space steps, which increase the computational time considerably.

3.5 Summary

In summary, the primary outcome of this chapter has been to analyse the final geometry formed due to the unsteady drawing of a slender viscous fluid fibre with an annular cross-section. We have considered the effects on the final geometry of pulling force, surface tension, active channel pressurisation, and axially varying viscosity along the heated region, with the temperature assumed to be uniform within a cross-section. Numerical solutions discussed in this chapter suggest that inner channel pressurisation may be used to obtain an emitter with a near-uniform bore and a small wall thickness at the very tip, with pressure counteracting the effect of surface tension. The model and solution method here described, enable determination of a pulling force $\hat{F}$, channel over-pressure $\hat{P}$, and draw time t_K, to achieve tapers with a desired internal diameter and wall thickness at the very tip, from a given tubular fibre, for a prescribed viscosity profile that may vary in time and space. There is not a unique solution to this problem; multiple parameter sets $(\hat{F}, \hat{P}, t_K)$ will yield the same geometry at the tip with a larger pulling force requiring

a larger over-pressure. However, the geometry along the length of the taper, which is also found, will vary between parameter sets and this may be used to determine the best choice of the parameters.

The geometry of the taper is quite sensitive to the pulling force and pressure parameters. A taper for use in mass spectrometry, having a tip with channel diameter near to that of the original fibre and small wall thickness, implies a geometry at the tip with significantly larger aspect ratio ϕ and smaller cross-sectional area χ^2 than the original fibre which, in turn, implies an over-pressure and pulling force that are nearing the regime where the fibre may burst or break. As the pulling force and over-pressure reduce, the sensitivity increases such that a very small variation in the force or pressure will result in the fibre bursting ($\phi \to 1$) or the channel closing ($\phi \to 0$). Note that such a failure will occur first at the tip which is subjected to the greatest amount of heat and consequently undergoes more deformation than any other cross-section. Practical limitations on maintaining the force and pressure at given values will, then, require that these parameters be sufficiently large so that small variations do not result in unacceptable changes in ϕ at the tip. However, larger force and over-pressure result in greater non-uniformity of the internal channel, i.e. a larger bulge in the inner channel, so that increasing these parameters too much is also not desirable. Clearly there is a trade-off between the two and an optimisation problem to be solved based on physical limitations of the puller and fitness for purpose of the taper.

Following that, we discussed the key results for the case of zero pressure, such as the maximum possible draw times to avoid events such as inner channel closure and breaking of the tube. This semi-analytical solution provides a more intuitive understanding of these scenarios as well as validates the numerical procedure. When $\hat{P} = 0$, the deformations in the cross-section are solely due to the effect of surface tension. Since this depends on the curvature κ of the geometry, the narrower the channel, the faster it closes. When the

pressure is not zero, there is a competition between the stretching and the effect of surface tension and pressurisation on the geometry. The optimal draw parameters are the ones that allows the least variation in the inner channel in a parameter regime where there is less sensitivity of geometry to small changes in the parameters and can be assured within reasonable tolerances.

Chapter 4

Pressure dominant flow

4.1 Introduction

In Chapters 2 and 3 it was assumed that the dimensionless surface tension was $\hat{\gamma} = O(1)$ and hence we derived model equations assuming the effect of surface tension to be important in the cross-plane problem. The importance of surface tension depends on the choice of the other dimensionless parameters and the geometry under consideration (Tronnolone et al. 2016). Dewynne et al. (1994) demonstrated that when the surface tension is neglected, the cross-section only rescales as its absolute size changes, and the problem can be reduced to a one-dimensional boundary value problem that can be solved efficiently for the cross-sectional area as a function of the axial coordinate. In the context of manufacturing emitters, maintaining a uniform inner channel using the heating and pulling method requires a considerable amount of pressure in addition to the pulling force. When the force applied is high enough, the surface tension is negligible in comparison, essentially allowing us to eliminate it. However, for $\hat{\gamma} \to 0$ the scalings of Section 3.2 are not appropriate, with $\frac{d\tau}{dt} \to 0$ in (2.18) and $\hat{P}/\hat{\gamma} \to \infty$ in (2.20), so that the scaling must

be changed.

In this chapter we develop a new method for defining reduced time that governs the cross-plane flow problem assuming the effect of surface tension is small compared to the applied pressure. In simple terms, pressure dominates the motion in the transverse flow compared with the effects of surface tension, and hence deformations within the cross-plane are primarily generated by the effect of pressure. This leads us to a different set of governing equations which allows us to explore the deformations in the cross-plane for scenarios in which force and pressure have been identified as essential for achieving the desired geometry. We will refer to this flow as a pressure-driven transverse flow. Furthermore, by rescaling the definition of the reduced time variable, we can consider more model simplifications such as zero surface tension which results in complete analytical solutions, and weak surface tension which results in semi-analytical solutions, as discussed in the subsequent sections of this chapter.

4.2 Pressure-driven transverse flow

We start with an alternative rescaling of pressure and velocity to that given in (2.17), using $\hat{P}$ in place of $\hat{\gamma}$. Thus we now define

$$p = p_z + \frac{\hat{P}}{\chi}\tilde{p}, \qquad v = v_z + \frac{\hat{P}}{\hat{\mu}(\tilde{x},t)}\tilde{v}, \tag{4.1}$$

where the transverse variables are denoted by tildes. Along with this scaling, the reduced time variable $\hat{\tau}$ for the transverse problem in a flow with significant pressure effects compared with the surface tension is modified to be

$$\frac{d\hat{\tau}}{dt} = \frac{\hat{P}}{\hat{\mu}(\tilde{x},t)\,\chi}. \tag{4.2}$$

The new scalings for both pressure and velocity in (4.1) also modify the dynamic boundary conditions (for both external and internal boundaries of the tube) we had previously in (2.19c) and (2.19d) in Chapter 2 as

$$-\tilde{p} + 2\frac{\partial \tilde{v}}{\partial \tilde{r}} = -\frac{\hat{\gamma}\tilde{\kappa}^{(0)}}{\hat{P}}, \quad \text{on } \mathrm{G}^{(0)} = 0, \tag{4.3a}$$

$$-\tilde{p} + 2\frac{\partial \tilde{v}}{\partial \tilde{r}} = -\left(\frac{\hat{\gamma}\tilde{\kappa}^{(1)}}{\hat{P}} - \chi\right), \quad \text{on } \mathrm{G}^{(1)} = 0, \tag{4.3b}$$

which apply on $\tilde{r} = \tilde{R}$ and $\tilde{r} = \phi\tilde{R}$ respectively. The kinematic boundary condition remains unchanged as

$$\frac{\partial G^{(i)}}{\partial \tau} + \tilde{v} = 0, \quad \text{on } \mathrm{G}^{(i)} = 0, \quad i = 0, 1. \tag{4.4}$$

Recall that the flow in a cross-section is determined by the solution of the classical Stokes flow free boundary problem, given in (2.19a) and (2.19b). Integrating (2.19a) and (2.19b) yields

$$\tilde{v} = \frac{A}{\tilde{r}}, \quad \tilde{p} = B, \tag{4.5}$$

where A and B are constants of integration. We may now solve for the velocity and pressure by substituting for $\tilde{v}, \tilde{p}$ and $\tilde{\kappa}$ into (4.3a) and (4.3b) resulting in the following expressions for radial velocity and pressure

$$\tilde{v} = \frac{\phi^2\tilde{R}^2}{2\tilde{r}(\phi^2 - 1)}\left[\frac{\hat{\gamma}(\phi + 1)}{\hat{P}\phi\tilde{R}} - \chi\right], \tag{4.6}$$

$$\tilde{p} = \frac{1}{(\phi - 1)}\left[\frac{\chi\phi^2}{(\phi + 1)} - \frac{\hat{\gamma}}{\hat{P}\tilde{R}}\right].$$

Then substituting for $\tilde{v}$ in the two kinematic conditions given in (4.4) for $i = 0, 1$ we find that

$$\frac{d\tilde{R}}{d\hat{\tau}} = -\frac{\phi\hat{\gamma}}{2\hat{P}(1-\phi)} + \frac{\phi^2\tilde{R}\chi}{2(1-\phi^2)}, \tag{4.7}$$

$$\frac{d(\phi\tilde{R})}{d\hat{\tau}} = -\frac{\hat{\gamma}}{2\hat{P}(1-\phi)} + \frac{\phi\tilde{R}\chi}{2(1-\phi^2)}. \tag{4.8}$$

Using the fact that the transverse flow problem is scaled to have a unit area i.e., $\pi\tilde{R}^2(1-\phi^2) = 1$, we obtain a differential equation for ϕ as

$$\frac{d\phi}{d\hat{\tau}} = -\frac{\hat{\gamma}\sqrt{\pi}(1+\phi)^{\frac{3}{2}}(1-\phi)^{\frac{1}{2}}}{2\hat{P}} + \frac{\phi\chi}{2}, \tag{4.9}$$

using the revised scaling for $\hat{\tau}$ introduced in (4.2). We obtain the equation governing the axial flow for a flow with significant pressure effects using the new $\hat{\tau}$ variable as

$$\frac{D\chi}{D\hat{\tau}} = \frac{\hat{\gamma}}{12\,\hat{P}}\,\chi\,\tilde{\Gamma} - \frac{\hat{F}}{\hat{P}}. \tag{4.10}$$

Finally, substituting for $\tilde{\Gamma}$ using (2.21) in (4.10) the axial model in terms of $\phi(\hat{\tau})$ is

$$\frac{D\chi}{D\hat{\tau}} = \frac{\sqrt{\pi}\,\hat{\gamma}}{6\,\hat{P}}\,\chi\sqrt{\frac{1+\phi}{1-\phi}} - \frac{\hat{F}}{\hat{P}}. \tag{4.11}$$

As with the complete model in Chapter 2 for a transverse flow where the reduced time was defined with surface tension, the equations governing the axial and transverse flow models in this alternative scaling are fully-coupled due to the presence of the axial variable χ in the cross-plane model. As a result, an analytical solution is unattainable and so we seek numerical solutions to the system of equations comprising (2.13), (4.2), (4.9) and (4.11).

4.2.1 Numerical solutions for pulling with a strong (constant) force

Recall that in Chapter 3, in the absence of a natural velocity scale, we set a characteristic velocity U by setting $\hat{\gamma} = 1$. However, in this chapter, since we aim eventually to neglect the effect of surface tension in the subsequent sections, we here define a characteristic velocity U by setting $\hat{F} = 1$, corresponding to a case of a known pulling force and so substantial stretching. Thus, gives a velocity scale $U = FH/6\mu_{hot}S_0$. In terms of the new velocity scale, the scaled variables (denoted by hats that comply with the same convention as in Chapter 2) are as follows

$$\begin{aligned}(x, r) = H(\hat{x}, \epsilon\hat{r}), \quad (u, v) = \frac{FH}{6\mu_{hot}S_0}(\hat{u}, \epsilon\hat{v}), \quad t = \frac{6\mu_{hot}S_0}{F}\,\hat{t},\\ p = \frac{F}{6S_0}\,\hat{p}, \quad \gamma = \frac{F}{6\sqrt{S_0}}\hat{\gamma}, \quad P = \frac{F}{6S_0}\hat{P}.\end{aligned} \tag{4.12}$$

Also, we set $\hat{F} = 1$ in (4.10) and (4.11). In our numerical procedure, (4.9) and (4.11) can be solved first for $\chi(\tilde{x}, \hat{\tau})$ independently of (4.2) and (2.13). Equation (4.11) describes the change in the cross-sectional area with $\hat{\tau}$ due to stretching; whereas (4.9) describes the evolution of the cross-sectional shape (i.e. aspect ratio) with $\hat{\tau}$ due to the effect of pressure and surface tension. For $\hat{\gamma} \neq 0$, these two equations are fully coupled and thus need to be solved simultaneously.

To complete the mathematical formulation of the problem and determine the physical geometry of the tube at physical time t, we must solve (4.2) for $t(\tilde{x}, \hat{\tau})$, scaled in terms of scaled applied pressure $\hat{P}$, at physical position $x(\tilde{x}, \hat{\tau})$, as given by (2.13). As with the full model discussed in Section 2.2.4, the above system of differential equations are

fully coupled in a rather complex manner as viscosity is a function of physical position x and time t similar to the model equations in Chapters 2 and 3, requiring a numerical solution. The procedure for generating this numerical solution is similar to that described previously in Section 2.3.2, since the underlying system of differential equations is the same as those from Chapter 2, rescaled with $\hat{P}$ instead of $\hat{\gamma}$. The importance of this modification to the definition of reduced time is that it permits the limiting cases of $\hat{\gamma} = 0$ and $\hat{\gamma}/\hat{P} \ll 1$, which will be explored in Sections 4.2.3 and 4.2.5, respectively. In these later sections we will see that (4.9) decouples from (4.11) and the solution to the transverse problem can be found analytically in terms of $\hat{\tau}$ for $\hat{P} \neq 0$, which could not be done when the reduced time was scaled with $\hat{\gamma}$.

The time stepping procedure for the numerical solution for the full model, including both surface tension and pressure, can be summarised below. We first introduce the time-discretisation of (4.2) that scales the reduced time using $\hat{P}$ for each t using a forward Euler method as

$$\hat{\tau}_{j,k+1} = \hat{\tau}_{j,k} + \frac{\hat{P}\Delta t}{\mu_{j,k}\,\chi_{j,k}}, \quad j = 0, 1, \ldots, J. \tag{4.13}$$

The rest of the algorithm for obtaining the solution for the system of equations for t_{k+1} is as in Chapter 2 but is repeated below for ease of reading:

1. compute $\hat{\tau}_{j,k+1}$ using (4.13), for all the cross-sections $\tilde{x}_j$, where $j = 0, 1, \ldots, J$;
2. determine $\chi_{j,k+1}$ and $\phi_{j,k+1}$ for $j = 0, 1, \ldots, J$ by interpolation of the previously-obtained solution $(\hat{\tau}_i, \chi_i^*, \phi_i^*)$ to (4.11) and (4.9) using MATLAB's 'deval' function;
3. compute $x_{j+1,k+1}$ using (2.31) for $j = 0, 1, \ldots, , J-1$;
4. update the viscosity i.e., $\mu_{j,k+1} = \mu(x_{j,k+1}, t_{k+1})$.

Here $\chi(\tilde{x}, \hat{\tau}_i) = \chi_i^*$, and $\phi(\tilde{x}, \hat{\tau}_i) = \phi_i^*$ are the solutions for (4.11) and (4.9) using the

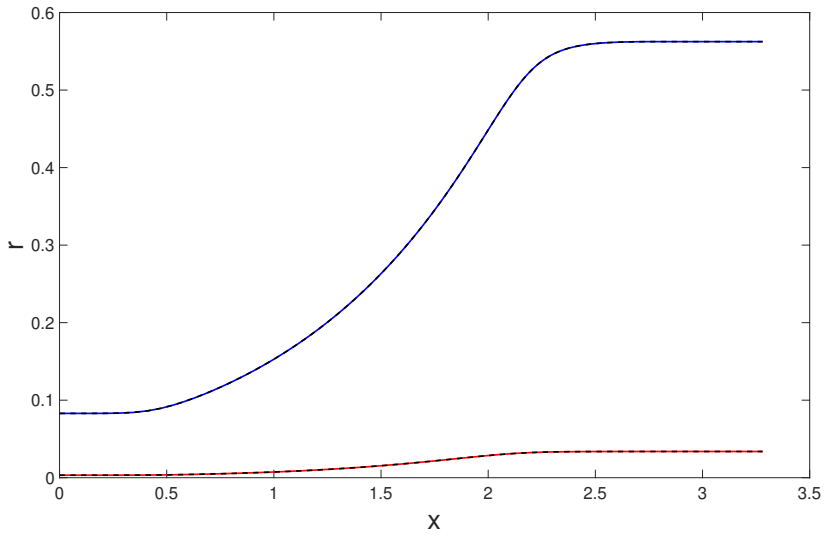

Figure 4.1: The inner and outer radii of an emitter obtained from an axisymmetric tube with initial length $L(0) = 1.5$, cross-sectional area $\chi^2(x, 0) = 1$ and aspect ratio $\phi(x, 0) = 0.06$, by pulling with force $\hat{F} = 1$, surface tension $\hat{\gamma} = 0.1$ and pressure $\hat{P} = 4$ for time $t_K = 0.5$. In blue(outer radius) and red(inner radius) are the radii obtained using model equations in Chapter 2 and in dashed black (outer and inner) are obtained using model equations developed in Chapter 4.

MATLAB ODE solver (`ode45`) for a sufficiently large $\hat{\tau}$ range. The above algorithm is repeated through to the final time t_K by incrementing the time step.

Recall that, depending on the problem parameters, a number of events are possible: namely, bursting of the tube when $\phi \to 1$, and breaking of the fibre defined as $\chi \to 1$, and closure of the channel when $\phi \to 0$. In the case of $\hat{\gamma} \ll \hat{P}$, for which ϕ necessarily increases with $\hat{\tau}$, inner channel closure cannot occur as the transverse flow is dominated by pressure and the surface tension is too weak to counteract. More generally, these events must be identified as a part of the solution process. As we have discussed in Chapter 3, none of these events are permissible in pulling emitters and, computation beyond these events is stopped by flagging them as events in the MATLAB ODE solver.

The obtained final geometry of the emitter is comparable with that generated from the

set of differential equations outlined in earlier chapters, where the reduced time is scaled with the surface tension using the same dimensionless parameters, providing a form of mutual validation for both scalings (see Figure 4.1).

4.2.2 Achieving a uniform bore

As we have identified in Chapter 3, not all choices of pressure and force can produce emitters tips with desired dimensions. The tolerance of the instrument used in the manufacturing process necessitates significant attention when choosing the operational parameters. If the force F is known and we set $\hat{F} = 1$, we have a choice between the pressure and the surface tension parameters. However, since the surface tension γ of molten glass is highly dependent on its composition, we are essentially limited to choosing an acceptable pressure P to achieve the desired geometry.

To aid our understanding of the effect of surface tension $\hat{\gamma}$ and pressure $\hat{P}$ on the evolution of the geometry with a close to uniform bore, we refer to Figure 4.2, showing a number of phase plane plots for a tube with an initial aspect ratio $\phi_0 = 0.06$. Each plot is for a different value of surface tension $\hat{\gamma}$ of size $O(10^{-2})$. Each curve corresponds to a different pressure $\hat{P}$ and shows how the geometry (χ, ϕ) evolves by solving the governing equations (4.11) and (4.9) numerically (using MATLAB) as $\hat{\tau}$ increases. The solutions of the phase plane are only allowed within the physically feasible region of $0 \leq \chi \leq 1$ and $0 < \phi < 1$. We have chosen to vary $\hat{P}$ starting from $\hat{P} = 1$, as the scaling requires $\hat{P} > 0$. These plots illustrate the competition between the surface tension and the pressure to reach the desired final geometry $(\chi_T, \phi_T) = (0.1911, 0.3)$ represented by a black dot in each of these plots and corresponding to $\phi_T R_T = \phi_0 R_0 = 0.0339$.

Figure 4.3 compares the phase plane plots for a surface tension of size $O(10^{-1})$, indicating the impact of a surface tension for an order of magnitude larger than the plots in

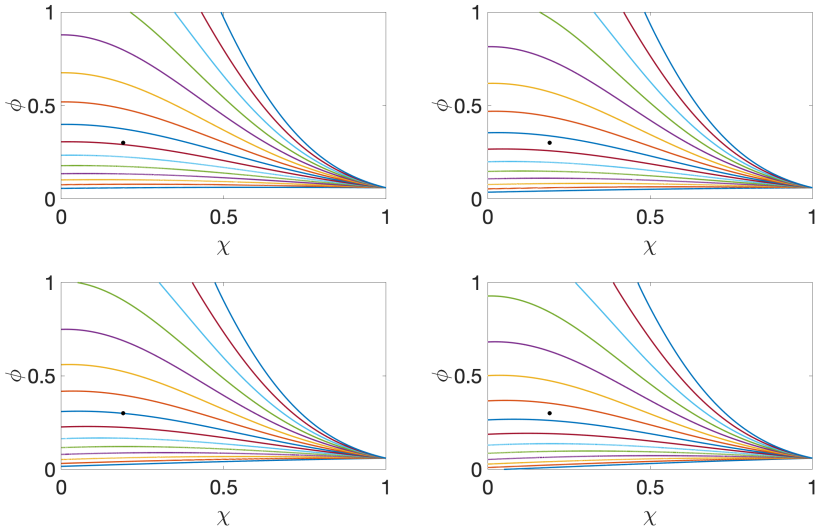

Figure 4.2: $\phi(\hat{\tau})$ versus $\chi(\hat{\tau})$ for a capillary with initial aspect ratio $\phi_0 = 0.06$, where surface tension $\hat{\gamma} = 0.02$ (top left), 0.04 (top right), 0.06 (bottom left) and 0.08 (bottom right) for a $\hat{P}$ ranging from 1 to 15 in increments of 1 increasing from bottom to top. The black dot is $(\chi_T, \phi_T) = (0.1911, 0.3)$ corresponding to the final geometry at $x = 0$.

Figure 4.2 for the same range of pressure values. These plots show that as $\hat{\gamma}$ increases, the differences become more visible and the outcome becomes more sensitive to the surface tension, estimating that to reach (χ_T, ϕ_T) when $\hat{\gamma} = 0.1$ requires $\hat{P} \approx 9$ and the required pressure $\hat{P}$ increases as $\hat{\gamma}$ increases.

As $\hat{\gamma}$ increases larger pressure is needed to achieve the desired tip geometry (χ_T, ϕ_T). Also notice that compared with $\hat{\gamma} = O(10^{-2})$ for $\hat{\gamma} = 0.1$ and 0.2, fibre explosion, i.e., $\phi \to 1$, occurs at higher pressures, while for $\hat{\gamma} = 0.3$, and 0.4, the majority/all of the curves go to $\phi_T = 0$ (hole closure). Once again we are seeking parameters near to the limiting cases of bursting and breaking and, therefore, the solution can be very sensitive to changes in the parameter values. At $\hat{\gamma} = 0.4$, all the curves have hit $\phi = 0$ resulting in inner channel closure as the pressure is insufficient to counteract the effect of the surface tension. These plots suggest that when $\hat{\gamma} = O(10^{-1})$, the impact of surface tension cannot

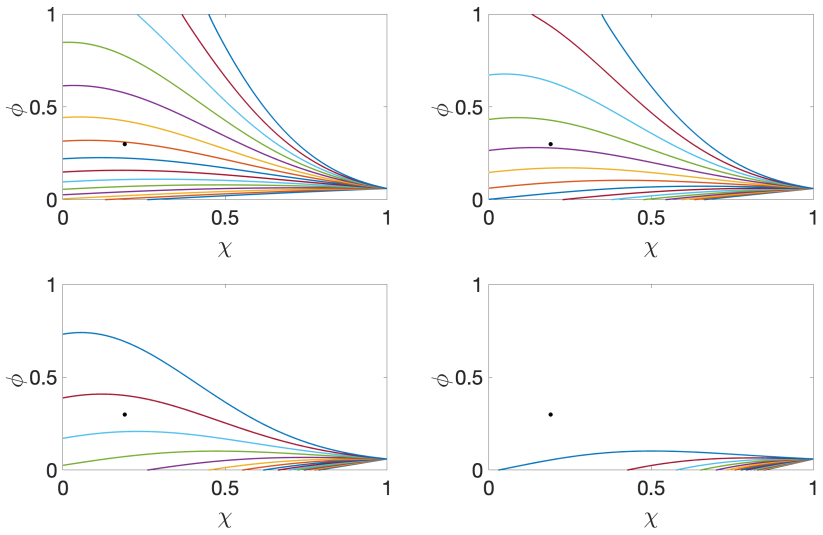

Figure 4.3: $\phi(\hat{\tau})$ versus $\chi(\hat{\tau})$ for a capillary with initial aspect ratio $\phi_0 = 0.06$, where $\hat{F} = 1$, surface tension $\hat{\gamma} = 0.1$ (top left), 0.2 (top right), 0.3 (bottom left) and 0.4 (bottom right) for a $\hat{P}$ ranging from 1 to 15 in increments of 1 increasing from bottom to top. The black dot is at $\chi_T \sim 0.1911$ and $\phi_T = 0.3$ corresponding to the dimensions of final emitter geometry at the tip.

be ignored, and if $\phi_T > \phi_0$ is desired, then the pressure $\hat{P}$ must be above a large threshold value to overcome the surface tension. As can be seen across all four values of order $\hat{\gamma} = O(10^{-2})$ in Figure 4.2 the solutions are not very sensitive to changes in pressure, suggesting that surface tension has a less significant impact on the solution.

We further improve our search for the required $\hat{P}$ that generates the (χ_T, ϕ_T) for a fixed value of $\hat{\gamma}$ by developing a root finding algorithm as follows

1. set the $\hat{\gamma}$ value;

2. set an initial range for $\hat{P}$ as an initial approximation;

3. solve (4.11) and (4.9) in MATLAB with `ode45` for a large $\hat{\tau}$ span;

4. use the function `fzero` in MATLAB to calculate the $\hat{P}$ that produces the desired

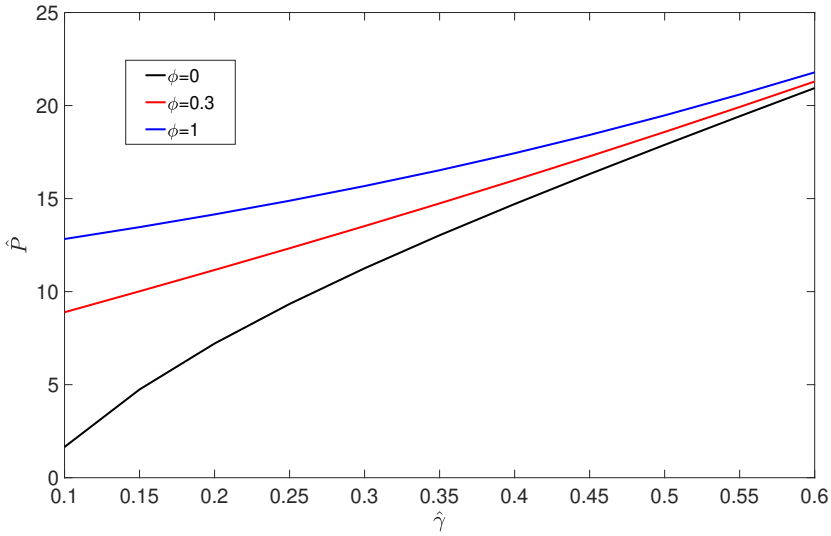

Figure 4.4: Inner channel pressure $\hat{P}$ versus surface tension $\hat{\gamma}$ for the manufacture of the emitters with $\chi_T = 0.1911$, and $\phi_T = 0$ (black), $\phi_T = 0.3$ (red), and $\phi_T = 1$ (blue), from a tube with initial geometry $\phi_0 = 0.06$.

ϕ_T at the tip;

5. define `events` in MATLAB ODE solver to stop computations beyond the desired χ_T.

We can also avoid other undesirable events such as $\phi = 0$, $\chi = 0$, and $\phi = 1$ by using the `events` option in the ODE solver to stop the computations if any of these occur. As an alternative to the final step in the above algorithm, $\phi_T R_T - \phi_0 R_0 = 0$ can also be used as the `event` in place of specifying the condition in terms of χ_T.

The resulting $\hat{P}$ from the above algorithm can then be used effectively in the full model to generate the geometry of the final fibre, using the spatially varying viscosity profile in 3.2, and for a suitable final draw time t_K, which corresponds to the resulting $\hat{\tau}_I$, obtained as an output from the above algorithm. Alternatively, the above algorithm can be modified to improve our search for an optimal pressure, $\hat{P}$, over a given array of $\hat{\gamma}$ values.

Figure 4.4 shows in red the combination of the parameters $(\hat{\gamma}, \hat{P})$ required to obtain $(\chi_T, \phi_T) = (0.1911, 0.3)$ from a tube with an initial geometry of $(\chi, \phi) = (1, 0.06)$. Shown in blue is the curve on and above which $(\chi_T, \phi_T) = (0.1911, 1)$, and the tube bursts at $x = 0$, while the curve on and below which $(\chi_T, \phi_T) = (0.1911, 0)$, and the channel at the tip $x = 0$ closes, is shown in black. To obtain a valid emitter tip, the values of $\hat{P}$, and $\hat{\gamma}$, must be chosen from the region between the upper and lower curves. The figure shows clearly the sensitivity of ϕ_T to the surface tension $\hat{\gamma}$. The sensitivity increases as $\hat{\gamma}$ increases. This shows that surface tension has a clear impact on the geometry when $\hat{\gamma} = O(10^{-1})$ or more. For smaller surface tension, the tip geometry will be less sensitive to the choice of pressure.

Recall that the optimal choice of the parameters corresponds to the smallest $\hat{P}$ leading to an emitter with the most uniform internal channel radius (smallest bulge) possible. Given that surface tension (γ) is determined by the composition of the material, and that the above algorithm determines the pair $(\hat{\gamma}, \hat{P})$ that yields the desired final geometry (χ_T, ϕ_T), then the scaling in (4.12) gives a dimensional pressure of $P = \frac{\gamma \hat{P}}{\sqrt{S_0 \hat{\gamma}}}$. The solution for $\hat{\gamma} = 0.1$ is shown in Figure 4.5 at the (final) time when $\phi_T R_T = \phi_0 R_0 = 0.0339$, i.e. the inner radius at $x = 0$ equals that of the initial tube.

Figure 4.6 compares the inner radius $\phi(x)R(x)$ at a fixed final time of $t_K = 0.1$, for two different pressure values, with the left being $\hat{P} = 1$ and the right being $\hat{P} = 10$ and using the axially varying viscosity as in (3.2) with $n = 6$. Each of the curves in a plot corresponds to a different surface tension of size $\hat{\gamma} = O(10^{-1})$ and shows how the $\phi_T R_T$ changes due to the competition between the surface tension and the pressure. For high pressure and low surface tension, i.e., $\hat{\gamma} = 0.1$ and $\hat{P} = 10$, the pressure opens the channels compared with the initial dimensions $(\phi_T R_T > \phi_0 R_0)$, thereby opposing the effect of surface tension, which tends to shrink these small-scale structures as the fibre

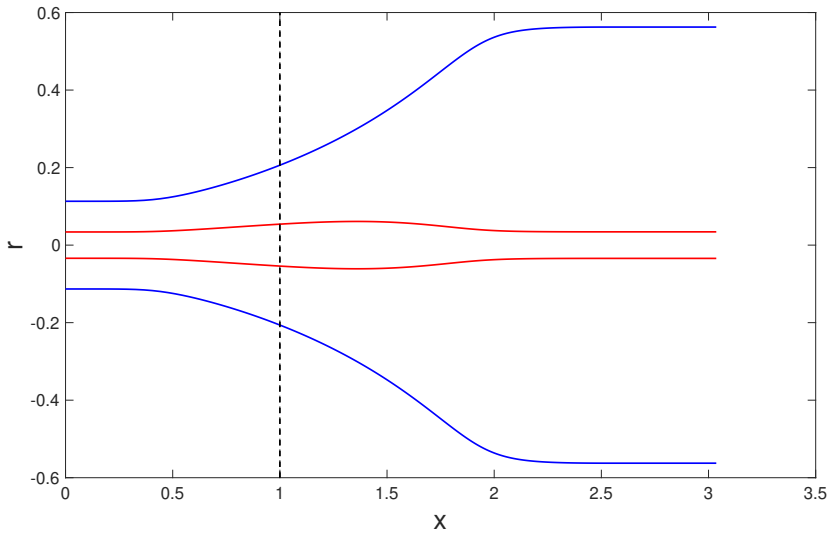

Figure 4.5: Plot of the final emitter geometry for a tube with initial length $L(0) = 1.5$, cross-sectional area $\chi^2 = 1$, and aspect ratio $\phi(x, 0) = 0.06$, after pulling for a time $t_K = 0.4932$ with surface tension $\hat{\gamma} = 0.1$ while applying an internal channel pressure $\hat{P} = 8.8919$. The external boundary $r = R(x)$ is shown in blue and the internal boundary $r = R(x)\phi(x)$ is shown in red. The aspect ratio and cross-sectional area at the tip are $\phi_T = 0.3, \chi_T = 0.1911$.

is drawn. For sufficiently large pressures, they can burst. At low pressures, the surface tension prevents a fibre explosion but can result in inner channel closure. These plots show clearly that pressure can make a significant impact on the dimension of the inner channel by counteracting the effects of surface tension, especially on geometries with small boundaries. It needs to be remembered that as the pressure increases, the variation in the inner channel radius increases, resulting in a larger bulge; conversely, as the pressure decreases, the size of the bulge reduces, albeit with the risk of channel closure.

Fundamentally, our analysis so far indicates that if the surface tension is of $O(10^{-1})$ or more, it has a significant effect on the flow and cannot be neglected. Pressurising the inner channel during the stretching process can avoid the inner channel's closure but when too large can result in bursting of the tube. To achieve a nearly uniform channel, an increased

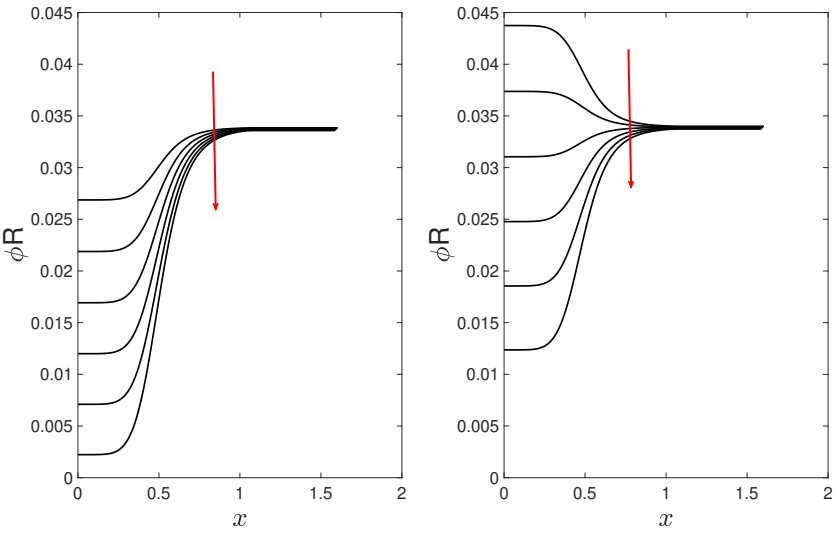

Figure 4.6: $\phi(x, t_K)R(x, t_K)$ over the position x after pulling from an initial length of $L(0) = 1.5$, and inner radius $\phi_0 R_0 = 0.0339$. Pulling with pressure $\hat{P} = 1$ (left) and $\hat{P} = 10$ (right) for a surface tension $\hat{\gamma}$ ranging from $\hat{\gamma} = 0.1 - 0.6$ in increments of 0.1 (top to bottom), and a draw time of $t_K = 0.1$. The arrow shows the direction of increasing surface tension. The results are obtained using the viscosity profile in (3.2) with $n = 6$.

aspect ratio is required at the tip, which requires a significant amount of pressure. In the following analysis, we shall refer to these model solutions in the presence of non-negligible surface tension as the "full solution". We next re-frame our model in such a way that we can investigate the effect of surface tension under the assumption that it has negligible or only a weak effect relative to the other parameters affecting the flow.

4.2.3 Solution for zero surface tension (ZST)

The axisymmetric model described in the previous section has the advantage of being sufficiently general to include the effects of both surface tension and pressure on the evolution of the geometry. As a consequence of introducing a reduced time variable

defined with pressure we may now use this model to investigate the case in which the surface tension is disregarded ($\hat{\gamma} = 0$). Interestingly, when $\hat{\gamma} = 0$ in a transverse pressure-driven flow, $\hat{\tau} \neq 0$ in (4.2) and thus the deformations within the transverse problem can still be addressed, which was not the case in the earlier flow model where surface tension is assumed to be important. Furthermore, in (4.10), in contrast with the solution of the full problem, the cross-sectional area χ^2 does not depend on the total boundary length $\Gamma(\tilde{x}, \hat{\tau})$ and (4.9) decouples from (4.10) such that the solution to the axial stretching problem can be found completely analytically in terms of $\hat{\tau}$. Thus the solution for χ is (with $\hat{F} = 1$)

$$\chi(\tilde{x}, \hat{\tau}) = \chi(\tilde{x}, 0) - \frac{\hat{\tau}}{\hat{P}}, \tag{4.14}$$

where $\chi(\tilde{x}, 0) = 1$. Substituting the above solution into (4.9), with a little rearrangement, we obtain a separable equation for ϕ

$$\frac{d\phi}{d\hat{\tau}} = \frac{\phi\chi}{2}, \tag{4.15}$$

which can be solved to obtain ϕ as

$$\phi(\tilde{x}, \hat{\tau}) = \phi_0 \exp\left[\frac{\hat{\tau}}{2}\left(1 - \frac{\hat{\tau}}{2\hat{P}}\right)\right], \tag{4.16}$$

where $\phi_0 = \phi(\tilde{x}, 0)$. For a known viscosity, using (4.2) the relationship between time and the reduced time $\hat{\tau}$ is given by

$$\frac{\hat{P}\, t}{m(\tilde{x}, t)} = \hat{\tau}\left(1 - \frac{\hat{\tau}}{2\hat{P}}\right), \tag{4.17}$$

where $m(\tilde{x},t)$ is the harmonic mean of the viscosity $\hat{\mu}(\tilde{x},t)$ at position $\tilde{x}$ over time t (Tronnolone 2016) which is defined as

$$m(\tilde{x},t) = \frac{t}{\int_0^t \frac{1}{\hat{\mu}(\tilde{x},t)} dt}. \tag{4.18}$$

Using the quadratic polynomial given in (4.17) and solving for $\hat{\tau}$ in terms of $m(\tilde{x},t)$ gives

$$\hat{\tau} = \hat{P}\left[1 - \left(1 - \frac{2t}{m(\tilde{x},t)}\right)^{\frac{1}{2}}\right], \tag{4.19}$$

where we must use the negative square root so that $\hat{\tau}(\tilde{x},0) = 0$. Thus, the ZST solution for a known $m(\tilde{x},t)$ provides a straightforward relationship for $\hat{\tau}$ for a final draw time t_K of interest. However, this is not particularly useful for the current problem for which $m(\tilde{x},t)$ changes with $\tilde{x}$ and depends on the stretching of the fibre. As a result, we use the exact solutions of (4.10), (4.9) and (4.2) with a known viscosity profile $\mu(x,t)$ and obtain a solution to the problem numerically using the numerical procedure described in Section 4.2.1 with $\hat{\gamma} = 0$.

Fundamentally, unlike in the case of transverse flow scaled with surface tension, we can address the $\hat{\gamma} = 0$ transverse problem using $\hat{\tau}$ scaled with $\hat{P}$ to generate an analytic solution for $\chi(\tilde{x},\hat{\tau})$, $\phi(\tilde{x},\hat{\tau})$ where deformations in the cross-section are solely due to pressure effects and then use a numerical procedure to determine $x(\tilde{x},\hat{\tau})$, $t(\tilde{x},\hat{\tau})$ and so find the physical geometry over time. This model is more useful for a flow domain with negligible effects of surface tension i.e., where there is a large pulling force that requires a significant amount of pressure to retain the uniformity of the internal channel.

4.2.4 Criterion for bursting and breaking

Having identified an analytical solution for the ZST case, we now use these solutions to extract additional useful and interesting details about the heat and draw process. One of the most important contributions of the modelling work to the laboratory fabrication process of these emitters is identifying the points of fibre explosion, which occurs at $\phi \to 1$, and breakage, when $\chi \to 0$. To find a condition for fibre explosion, we first rearrange the analytical expression for the aspect ratio in (4.16) to obtain a quadratic polynomial in $\hat{\tau}$, namely

$$\frac{\hat{\tau}^2}{2\hat{P}} - \hat{\tau} + 2\ln\left(\frac{\phi}{\phi_0}\right) = 0. \tag{4.20}$$

This can be solved to obtain $\hat{\tau}$ as

$$\hat{\tau} = \hat{P}\left(1 \pm \sqrt{1 - \frac{4\ln\left(\frac{\phi}{\phi_0}\right)}{\hat{P}}}\right), \tag{4.21}$$

where we must use the negative square root so that $\phi = \phi_0$ at $\hat{\tau} = 0$. Thus, the resulting expression for the reduced time takes the form

$$\hat{\tau} = \hat{P}\left(1 - \sqrt{1 - \frac{4\ln\left(\frac{\phi}{\phi_0}\right)}{\hat{P}}}\right). \tag{4.22}$$

Using (4.22) we can obtain the corresponding maximum possible reduced time $\hat{\tau}_B$ beyond which explosion occurs by setting $\phi = 1$, as

$$\hat{\tau}_B = \hat{P}\left(1 - \sqrt{1 - \frac{4\ln\left(\frac{1}{\phi_0}\right)}{\hat{P}}}\right). \tag{4.23}$$

So $\hat{\tau}_B = \hat{P}$ if $\hat{P} = 4\ln\left(\frac{1}{\phi_0}\right)$ else $\hat{\tau}_B < \hat{P}$ for $\hat{P} > 4\ln\left(\frac{1}{\phi_0}\right)$. Additionally, for real $\hat{\tau}_B$ we must have $1 \geq \frac{4}{\hat{P}}\ln\left(\frac{1}{\phi_0}\right)$, which gives a criterion for explosion. This can be rewritten in terms of the pressurisation and the initial aspect ratio of the fibre as

$$\hat{P} \geq 4\ln\left(\frac{1}{\phi_0}\right). \tag{4.24}$$

Considering the criterion for fibre breakage, when $\chi^2 \to 0$, we can also establish a condition for the fibre breakage with respect to reduced time using (4.14) and setting $\chi(\tilde{x}, 0) = 1$, as

$$\hat{\tau}_B = \hat{P}. \tag{4.25}$$

Thus, it can be concluded that in a pressure-driven transverse flow with ZST, as $\hat{\tau}$ increases from $\hat{\tau}(\tilde{x}, 0) = 0$ (at $t = 0$), the aspect ratio increases due to pressure (as there is no surface tension to counteract the pressure), and the tube breaks when $\chi^2 = 0$, or in particular when $\hat{\tau} = \hat{P}$ at some $\tilde{x}$. Since the criterion for bursting alone implies $\hat{\tau}_B \leq \hat{P}$, it is apparent that the tube will burst first or at the same time as breaking. In practice, $\hat{\tau} > \hat{P}$ has no meaning in the ZST case because the tube will have burst or broken for $\hat{\tau} \leq \hat{P}$. Furthermore, writing (4.11) in terms of t using (4.2) gives

$$\chi d\chi = \frac{-1}{\hat{\mu}(\tilde{x}, t)} dt, \tag{4.26}$$

which can be integrated analytically to obtain an expression for the maximum possible draw time t_B using the harmonic mean of the viscosity, $m(\tilde{x}, t)$, as

$$t = \frac{m(\tilde{x}, t)}{2}\left(1 - \chi^2\right) \implies t_B = \frac{\bar{m}(\tilde{x}, t)}{2}, \tag{4.27}$$

where $\chi = 0$ and $\bar{m}$ is the minimum of $m(\tilde{x}, t)$ over all $0 \leq x \leq 1$, i.e. the fibre breaks at the position $\tilde{x}$, where $m(\tilde{x}, t)$ is a minimum. For the current problem where $\mu(x, t)$ depends on stretching, a numerical solution is required.

4.2.5 The case of weak surface tension (WST)

Without the application of pressure, Tronnolone et al. (2016) showed and verified through experiments that if surface tension $\hat{\gamma}$ is $O(10^{-1})$, its effects are important in both the axial and cross-plane problem. However, if $\hat{\gamma}$ is $O(10^{-2})$, the influence of surface tension in the axial problem can be ignored, but it remains effective in the transverse flow problem in regions of large curvature, and this is referred to as weak surface tension (WST). In a surface tension driven transverse flow, $\hat{\tau}$ is scaled with $\hat{\gamma}$, and if the term $\hat{\gamma}/\chi$ in (2.18) is $O(1)$, deformations within a cross-section may be large as $\hat{\tau}$ increases, allowing for a significant shape change in the cross-plane.

Previously, we observed that when $\hat{\gamma}$ is $O(10^{-1})$ its effects are important and cannot be ignored. In a flow driven by pressure and surface tension, both the axial and the transverse flows given in (4.11) and (4.9) are influenced by the dimensionless ratio $\hat{\gamma}/\hat{P}$. We here consider the characteristics of a flow that is dominated by pressure relative to surface tension, with a strong pulling force i.e. $\hat{\gamma} \ll 1$ with $\hat{P} \sim 1$ which we term the weak surface tension case. For this case we may disregard the effect of surface tension in

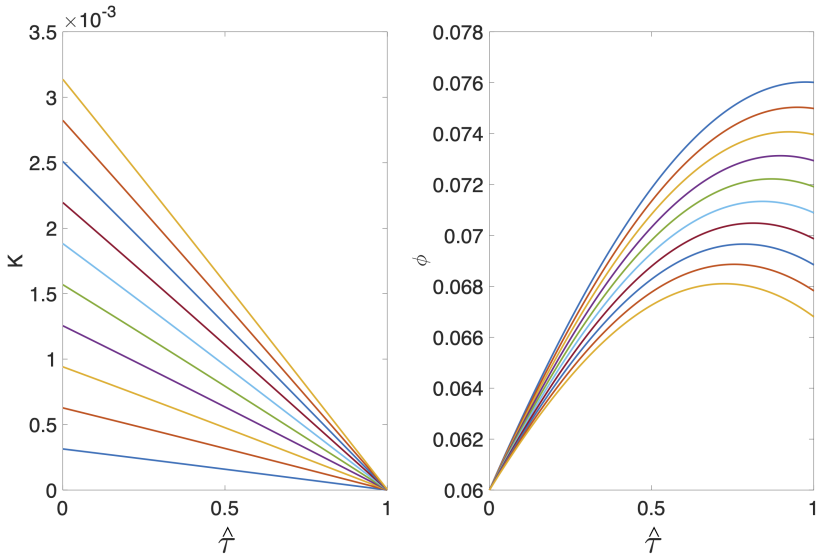

Figure 4.7: Plot of $K = \sqrt{\pi\,(1+\phi)}\hat{\gamma}\,\chi/6\sqrt{(1-\phi)}$ against $\hat{\tau}$ (left) and $\hat{\phi}$ against $\hat{\tau}$ (right) over a range of $\hat{\gamma} = 0.001 - 0.01$ in increments of 0.001 for a capillary with initial aspect ratio $\phi_0 = 0.06$ and $\chi_0 = 1$. The tube is pulled with a force $\hat{F} = 1$ and pressure $\hat{P} = 1$ corresponding to $10^{-3} \leq \hat{\gamma}/\hat{P} \leq 10^{-2}$.

the axial problem. However, we retain it in the transverse flow problem because it cannot be neglected when χ becomes small.

Consider equation (4.11) governing the axial model. Our argument here is, in order to disregard the term involving $\hat{\gamma}/\hat{P}$ in (4.11), it should be very small compared to $1/\hat{P}$, which leads to

$$K = \frac{\sqrt{\pi}\hat{\gamma}}{6}\chi\sqrt{\frac{1+\phi}{1-\phi}} \ll 1. \tag{4.28}$$

Figure 4.7 shows at left a plot of K against $\hat{\tau}$ for $O(10^{-3}) \leq \hat{\gamma} \leq O(10^{-2})$. As can be observed, for this range of $\hat{\gamma}/\hat{P}$ the term $K \ll 1$ implying that the term involving $\hat{\gamma}/\hat{P}$ is negligible in comparison to the term $1/\hat{P}$. Thus, the surface tension can be neglected from the axial problem. However, as shown in Figure 4.7 (right), the aspect ratio ϕ increases, then decreases showing the effect of surface tension in action opposing the effect of pressure. Figure 4.8 shows how solutions of (χ, ϕ) in the WST case compare

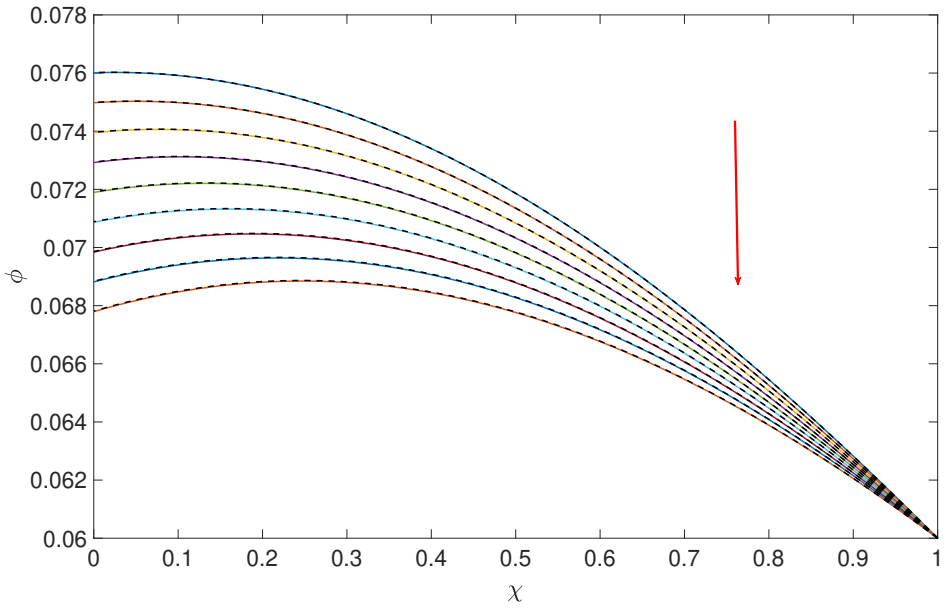

Figure 4.8: Plot of ϕ versus χ over a range of $\hat{\gamma} = 0.001 - 0.009$ in increments of 0.001 for a capillary with initial aspect ratio $\phi_0 = 0.06$ and $\chi_0 = 1$. The coloured straight lines represent the solutions for the WST case and the black dashed lines represent the solution to the full model. The tube is pulled with a pressure $\hat{P} = 1$ representing the range of $\hat{\gamma}/\hat{P} = O(10^{-3})$. The red arrow points in the direction of increasing surface tension.

with the full model (including the effect of surface tension in both axial and cross-plane models) for $\hat{\gamma}/\hat{P} = O(10^{-3})$ as $\hat{\tau}$ increases. Each curve stops at the boundary $\chi = 0$, when the fibre breaks. These plots show that for $\hat{\gamma}/\hat{P} = O(10^{-3})$ when $\hat{P} = 1$, the two solutions compare well to each other and thus WST is a good approximation to the full solution.

We note that the details of the WST with no pressurisation in the inner channel has been investigated extensively in Tronnolone (2016) regarding gravitational extension of a viscous thread and we refer interested readers to that work.

4.3 The case of zero surface tension (ZST) and zero pressure (ZP)

We briefly have discussed the case of zero surface tension and pressure, $\hat{\gamma} = \hat{P} = 0$. Neither of our reduced time variables are appropriate for this and we must revert to time t. As mentioned earlier the complete solution of the ZST and ZP case requires only an understanding of the axial flow model, which describes the change in cross-sectional area with respect to time. This is simply $d\chi^2/dt = -F/\mu$. As indicated earlier, there is no change to the aspect ratio ϕ and (4.9) becomes $d\phi/dt = 0$.

Thus, we obtain the equation that governs the cross-sectional area

$$\chi^2(\tilde{x}, t) = 1 - \frac{2\hat{F}t}{m(\tilde{x}, t)}, \tag{4.29}$$

where $m(\tilde{x}, t)$ is the harmonic mean of viscosity, as introduced in the previous section and $\chi_0^2 = 1$. A similar expression is obtained in the ZST case by Tronnolone (2016); however, for Tronnolone (2016) the force changes at each cross-section as that work models a mass falling under the influence of gravity making χ dependent on $\tilde{x}$, whereas we have a constant value for force and χ_0 is independent of $\tilde{x}$. Note that $\chi^2 \to 0$ as $t \to m(\tilde{x}, t)/2\hat{F}$ so the tube will break at the position $\tilde{x}$ where this first happens. Substituting the expression for $\chi^2(\tilde{x}, t)$ in (2.12), we obtain the solution for x in terms of $\tilde{x}$, which is

$$x(\tilde{x}, t) = \left[1 - \frac{2\hat{F}t}{m(\tilde{x}, t)}\right]^{-1} \tilde{x}. \tag{4.30}$$

This is useful for evaluating the extension of the tube after the draw process. Differentiating the above expression for x with respect to time we obtain an explicit expression for the velocity of the tube being pulled, namely

$$u(\tilde{x}, t) = \left(1 - \frac{2Ft}{3m(\tilde{x}, t)}\right)^{-2} \left(\frac{2F\tilde{x}}{\hat{\mu}(\tilde{x}, t)}\right). \tag{4.31}$$

Although the velocity is not a parameter in our model, the above expression may be useful to calculate an instantaneous pulling speed of a cross-section, if required. Note that $x \to \infty$ and $u \to \infty$ as $t \to m/2\hat{F}$, so the length and viscosity become infinite when the tube breaks.

4.4 Summary

In this chapter we have developed model equations for the unsteady stretching of a highly viscous fluid cylinder with a pressure-driven transverse flow. This was performed by introducing a new scaling of the cross-plane problem, using scaled pressure in place of surface tension with a view to examining, situations where $\hat{\gamma}/\hat{P} \ll 1$. As seen in this and previous chapters, in order to maintain an approximately uniform inner channel we must carefully balance the effects of stretching, surface tension, and pressurisation. As a result, considerable pressure is required to increase the aspect ratio (and thus maintain the physical channel size) at the tip and a decrease in force demands a decrease in pressure.

In addition to generating solutions to the full model, including the effects of both surface tension and pressure in both the axial and the transverse problems, we have considered the simplified models with surface tension featuring only in the transverse problem (the WST case) or neglected altogether (the ZST case). WST can be useful for typical values of $O(10^{-2}) \leq \hat{\gamma}$, where the impact on the axial problem from surface tension is insignificant and can be neglected, while still retaining its effect on the transverse flow to capture the small changes undergone within the cross-plane geometry. When $O(10^{-2}) \leq \hat{\gamma}/\hat{P} \leq O(10^{-1})$, the effect of surface tension is important for both axial flow and transverse flow to capture the geometry deformations, and in that case the full model, which includes the effects of both surface tension and pressure, must be considered. This model is

useful for investigating flow properties and geometry evolution in a flow field where the effect of surface tension is completely negligible ($\hat{\gamma} = 0$), which was not possible in the previous model equations discussed in Chapters 2 and 3 as the transverse flow parameter τ was scaled with the surface tension. In this case we generated a completely analytical solution and used this to develop critical criteria for events such as fibre explosion and fibre breaking. For these simplified models, the solution to the axial problem is independent of the total boundary length, $\Gamma(\tilde{x}, \hat{\tau})$ and hence independent of the transverse flow problem.

Chapter 5

The temperature model

5.1 Introduction

To date, the most important aspects of the process of unsteady stretching of heated glass tubes have been explained by defining spatially varying viscosity functions, beginning with a constant piecewise viscosity function and progressing to a spatially varying viscosity function that evaluated the effects of a non-uniform temperature distribution. The importance of spatial viscosity variation, as discussed in Chapter 3, is its effect on tube shape. Note that glass viscosity is highly sensitive to temperature. Temperature variations are significant in the glass deforming process because glass must be sufficiently heated to be deformed. Therefore, it will be beneficial to identify how temperature varies during the draw process to determine viscosity so that numerical simulations can be used effectively in industrial manufacturing of emitters.

Unfortunately, experimentally determining the actual temperature changes that occur during a draw is rather difficult. As the temperature changes, glass undergoes rapid viscosity changes. Stretching begins slowly as the glass is heated from room temperature but the stretching rate increases rapidly as the temperature nears the softening point. As the tube exits the heater, it cools causing the glass to undergo another rapid viscosity change

over the time. Stretching continues during the cooling stages until the glass solidifies. It is possible for the tube to break during or at the end of the pulling process. Considering these aspects will be of real benefit to the industry in respect to both obtaining the desired shape, and the final time taken for the fabrication. This reinforces the requirement for a comprehensive thermal model capable of capturing changes in temperature and thus viscosity across a broad temperature range, including at high temperatures, where the majority of deformation occurs rapidly, and direct measurements cannot be made.

The present chapter focuses on increasing the complexity of our model by developing a thermal model that integrates heat transfer with the fluid flow. This integrated model will then be solved numerically for the time-advancing flow during the heat and pull process. In the subsequent analysis of our problem, we aim to investigate the effect of spatial temperature variations, and the corresponding viscosity changes, that occur throughout the heat and pull process. The results of this study are considered for glass tubes manufactured from fused silica (F300) glass, which is by far the most frequently used material in the manufacture of emitters.

To justify several major model assumptions that help to determine the values of the parameters, we begin with a detailed examination of glass properties for silica glass and their dependence on temperature (Section 5.2). This section is followed by a derivation of a one dimensional temperature model for both heating and cooling phases, following the derivation given by Stokes et al. (2019) for steady fibre drawing. Here we assume the glass is heated using a laser rather than a gas flame. There are many advantages of CO_2 laser heating over gas flame heating, as stated in Grellier (2000) (Chapters 3 and 4) and Chryssou (1999). As Grellier (2000) and Chryssou (1999) highlight, the final diameter can be predicted when CO_2 laser heating is used as the heating is self-regulating. This is because as the fibre becomes narrower due to heating and pulling, the energy absorbed by

the glass becomes insufficient to maintain it at the softening point (Chryssou 1999). In Section 5.4, we discuss the procedure for generating numerical solutions for the evolution of the emitter geometry using the developed temperature model, coupled with the flow model.

5.2 Temperature dependence of material properties

As the first step towards simulating the heat and draw processes of glass under non-isothermal conditions, we discuss the temperature dependence of the key properties of glass and offer useful assumptions regarding these properties to be adopted in our model. The non-isothermal model equations require understanding of the properties of the molten glass, such as the viscosity, the density, surface tension, the specific heat, the thermal conductivity, and the emissivity. From the early stages of this thesis, we have considered that softened glass (molten glass) is an incompressible Newtonian fluid; an assumption which has been adopted generally in most of the literature outlined in Chapter 1 and can be considered precise enough for practical use.

5.2.1 Viscosity

The viscosity can be identified as the most important property in the process of glass forming. The viscosity (μ) of a fluid is a measure of the internal friction caused by the relative motion of its layers, as measured by the force per unit area resisting uniform flow. Viscosity is defined more precisely as the ratio of the shear stress to the shear rate. This ratio is independent of the shear rate for Newtonian fluids, implying that the shear stress and shear rate are linearly proportional. For glass, viscosity varies by orders of magnitude

with temperature. As the temperature decreases the viscosity increases rapidly until the glass is effectively solid. This solid glass is said to be a supercooled fluid. According to (Axinte 2011), the most commonly-used reference viscosity fixed points of glass that are useful in the different stages of the industrial glass production process are as listed below:

- **Working point** (10^3 Pa s) the temperature at which the glass can be deformed through pressing, blowing, and forming.

- **Softening point** ($10^{6.6}$ Pa s) the temperature at which the glass deforms under its own weight.

- **Annealing point** ($10^{13.4}$ Pa s) the temperature at which the glass can remove any internal stresses caused by the forming process in several minutes.

- **Strain point** ($10^{13.6}$ Pa s) the temperature at which a glass can be used without creeping for glass forming applications and any stresses can be relieved in hours. For temperatures above the strain point, glass resists flow, maintaining its shape.

There exist different mathematical relationships to express the temperature dependence of the viscosity. For many decades, the generally-accepted relationship between temperature (θ) and viscosity in glass has been the Vogel-Fulcher-Tammann (VFT) equation given in Scherer (1992) as

$$\log_{10} \mu = -A + \frac{B}{\theta - \theta_0}, \tag{5.1}$$

where A, B and θ_0 are constants that can be fitted empirically using data for a specific glass composition. Base 10 logarithms are used due to the large numbers involved. This relationship has been the most frequently used model in the literature and is considered suitable for predicting the variations of the viscosity across different temperature ranges.

The viscosity of silica, which is used in the manufacture of emitters, is considered to have two distinct temperature regimes. According to Doremus (2002), the viscosity of silica glass can follow the two parameter Arrhenius equation for high temperature regions from $\theta = 1400°\text{C}$ to $\theta = 2500°\text{C}$,

$$\mu = 0.58 \times 10^{-7} \exp\left(\frac{515400}{G_{cst}(\theta + 273.15)}\right), \tag{5.2a}$$

and for low temperature regions from $\theta = 1000°\text{C}$ to $\theta = 1400°\text{C}$,

$$\mu = 0.38 \times 10^{-13} \exp\left(\frac{712000}{G_{cst}(\theta + 273.15)}\right), \tag{5.2b}$$

where μ is in Pa s, θ is the temperature in Celsius and G_{cst} is the universal gas constant in $\text{JK}^{-1}\text{mol}^{-1}$. Recent experimental work by Boyd et al. (2012) and Jasion et al. (2015) confirm the use of this relationship in glass stretching experiments. The temperature range of interest in manufacturing emitters using fused silica is sufficiently high, that (5.2a) is the appropriate viscosity-temperature relation. According to Chryssou (1999), silica has a softening point of around 1660°C. With reference to the viscosity-temperature curve shown in Figure 5.1, the viscosity decreases strongly and continuously as the temperature increases. Although the rate of decrease reduces as temperature increases there is still a clear potential at high temperatures for even small temperature changes to have a substantial effect on the viscosity and, hence, the glass flow.

5.2.2 Density and surface tension

The density of a material (ρ) is defined as its mass per unit volume. In contrast with viscosity, the density of silica glass does not vary significantly with temperature but does vary according to its composition. Additionally, because we consider molten glass to be

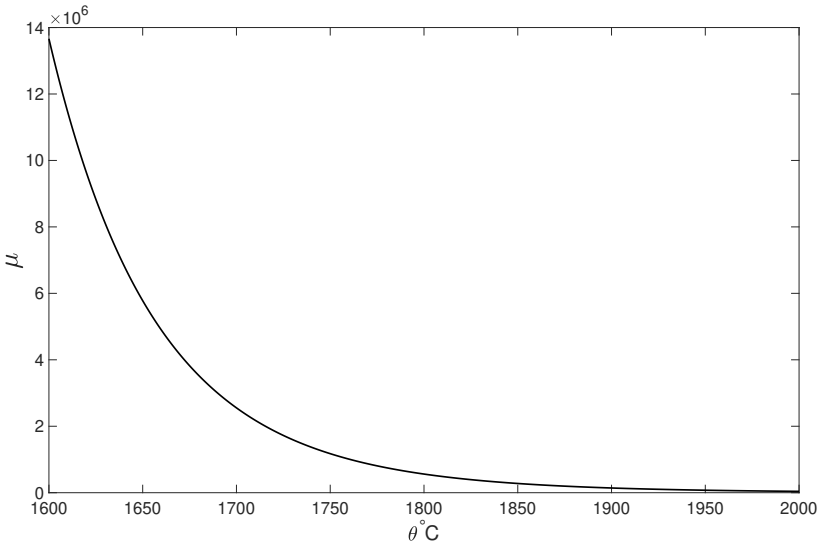

Figure 5.1: Viscosity as a function of the temperature.

an incompressible Newtonian fluid, we assume that density is not temperature-dependent. The density of silica is assumed to be $\rho = 2200\text{kg/m}^3$ (Grellier 2000, Jasion et al. 2015).

Surface tension, in studies of fibre glass drawing processes, is typically assumed to be strongly dependent on glass composition but not on temperature, and thus, is frequently treated as a constant or even ignored (Chouffart 2018). For silica glass Boyd et al. (2012) have calculated a value of $\gamma = 0.3\text{N/m}$ when the temperature is in the range 2400°C to 2600°C. The variation in the surface tension around the softening point of silica is approximately 0.02N/m per 100°C based on measurements between 1200°C and 1600°C with a measurement error of approximately 2% (Von der Ohe & Yue 2003). Accordingly, we disregard temperature variations in surface tension and use $\gamma = 0.3\text{N/m}$, as used by Jasion et al. (2015) for $\theta = 2000$°C. Although the coefficient of surface tension is assumed to be constant, note that the effect of surface tension becomes more significant, as curvature increases, as happens when cross-sectional area decreases due to stretching.

5.2.3 Specific heat

The specific heat (c_p) is defined as the amount of energy necessary to raise the temperature of a unit mass of material by one unit of temperature. It is determined by the composition of the glass and the temperature. As mentioned in Chouffart (2018), the value of c_p is expected to be constant above working point, and tends to drop gradually with the temperature in the solid state. For simplicity, we assume $c_p = 1140\text{J}/(\text{kgK})$ is a constant for silica glass (Heraeus F300) during the draw process (Jasion et al. 2015).

5.2.4 Emissivity

For the glass industry, the emission of radiation, determined by emissivity (β) from transparent materials is of fundamental importance. As specified in Grellier (2000), emissivity is determined using the notion that the total power emitted via radiation equals the total power absorbed at equilibrium. As stated in Chouffart (2018), emissivity of glass is dependent on temperature and thickness due to its semi-transparent nature. Emissivity, like many other characteristics, is temperature dependent. According to Chryssou (1999), the value for fused silica glass, starts at approximately $\beta = 1$, at room temperature, and rapidly decreases to about $\beta = 0.06$ at the softening point, which is $\theta = 1660°\text{C}$. We assume emissivity to be a constant at value $\beta = 0.8$ rounded from Jasion et al. (2015), to generate numerical outcomes using our model.

This concludes our discussion of glass properties relevant to the modelling that follows, and the values we have assumed.

5.3 Temperature modelling

We now return to the subject of developing a temperature model. As already briefly mentioned in Section 5.1, the temperature model requires two stages: heating and cooling. The Lagrangian formulation of the problem in an unsteady setting enables us to analyse the movement of fluid cross-sections with respect to the heated length. This enables the position of the cross-sections to be identified as being within or outside the heated length. The heating stage includes heating the glass from room temperature to the softening point, following which the temperature is maintained for a period until the heater is switched off externally. The cooling stage begins for cross-sections as they exit the heated length due to pulling and after the heater is turned off, at which point all the cross-sections cool. Thus, the objective of the temperature model is twofold: (1) to determine the increase in temperature caused by heating; and (2) to determine the systematic reductions in temperature of the cross-sections due to cooling.

As the first step, we recall the problem of heating and pulling a glass tube already described in Chapter 2, and illustrated in Figure 2.1. We assume that a laser heats a tube of length $2L$ over a length of $2H$ and that the tube is pulled from both sides by a constant force F, while pressurising the inner channel with a pressure P. Assuming that the heating and pulling are symmetrical about the centre, which is at $x = 0$, and hence that the velocity at $x = 0$ is zero, the initial point on the centreline, $\tilde{x} = 0$, will always correspond to the position $x = 0$. As a result, we define the problem to be symmetric about $x = 0$ and consider that half of the tube in the region $0 \leq x \leq L$, heated over $0 \leq x < H$ and pulled with force F at the end $x = L(t)$ while held fixed at $x = 0$. As introduced previously, we consider molten glass to be an incompressible Newtonian fluid, with density denoted by ρ, the specific heat capacity denoted by c_p and surface

tension denoted γ, all of which are assumed to be constants except for the viscosity $\mu(\theta)$, which is dependent on temperature (θ). The fluid is assumed to have constant thermal conductivity k, and emissivity β. The dimensions of the fibre denoted by S, ϕ, R, and, ϕR are as defined in Chapter 2.

The inability to record the temperature changes of glass during the heating and pulling process is one of the most significant drawbacks of laser heating. Due to the safety characteristics when the laser is activated, the whole device must be enclosed. This requires modelling the heat transfer in order to predict the temperature change in each cross-section during the tapering process. Several authors describe tapering optical fibres using a CO_2 laser as the heating source and give a Gaussian profile for the power distribution of the laser (Yokota et al. 1997, Chryssou 1999, Grellier 2000).

In the published literature, thermal models of glass forming processes frequently use complicated energy source terms designed for specific experimental set-ups that are not generally applicable. Rather than adopt such a model, in this thesis, we develop a relatively simple thermal model based on energy conservation to determine the spatial temperature variations in the glass caused by laser heating as used in the Sutter P-2000 puller used for experimental validation of our model. This model enables investigation of the sensitivity of emitter geometry to model quantities, and (approximate) determination of parameters by fitting to experimental data.

To begin, we define our assumptions. First, we consider the "thermal thinness" condition described in Grellier (2000) and Chryssou (1999), which enables us to model thermal energy transfer to glass in one dimension rather than three dimensions, assuming the laser heats the glass perpendicular to its axis. In other words, the radial distribution of temperature in glass is assumed to be uniform due to the very small cross-sectional area in comparison with the length of the tube. This is demonstrated asymptotically in Stokes

et al. (2019).

The governing equation for temperature θ takes the form,

$$\rho c_p \left(\frac{\partial \theta}{\partial t} + v \frac{\partial \theta}{\partial r} + u \frac{\partial \theta}{\partial x} \right) = k \left(\frac{1}{r} \frac{\partial}{\partial r} \left(r \frac{\partial \theta}{\partial r} \right) + \frac{\partial^2 \theta}{\partial x^2} \right) + Q(x), \tag{5.3}$$

where c_p and k are specific heat capacity and heat conductivity of the fluid. Although the total power of the laser is assumed to be constant, the laser oscillates over a small longitudinal section of the glass tube and the energy is not expected to be uniformly distributed. Hence, we define $Q(x)$ as the energy absorbed by the glass tube per unit volume per unit time at position x. We further assume that thermal energy supplied by the laser to the glass is given by the power density or the linear distribution of power, denoted by $q(x)$, over the heated length H, where $q(x)$ has units of energy per unit length and per unit time. Thus, $Q(x)$ can be defined as

$$Q(x) = \frac{q(x)}{S(x)}. \tag{5.4}$$

Assuming symmetry about $x = 0$, the total power delivered by the laser over the heated length $0 \leq x \leq H$ can be approximated as

$$\frac{P_{tot}}{2} = \int_0^H q(x)\, dx, \tag{5.5}$$

where P_{tot} is the total power delivered by the laser. However, the complete (100%) absorption of laser energy by the glass tube is not realistic, therefore, we introduce an important parameter named the fibre absorption efficiency factor (P_{abs}), which is defined in Chryssou (1999) to indicate the fraction of the energy absorbed by the glass tube. Considering this assumption in our model, (5.5) modifies to

$$\frac{P_{tot} P_{abs}}{2} = \int_0^H q(x)\, dx. \tag{5.6}$$

We now need to define the function $q(x)$ describing the power distribution of the laser. This distribution should reflect the effect of the laser power beam intensity. Following the literature involving CO_2 laser-based heating, i.e. Helebrant et al. (1993), Grellier et al. (1998) and Chryssou (1999), the power density is assumed to be a Gaussian distribution defined using an exponential function. Thus, we define $q(x)$ as,

$$q(x) = C \exp\left(\frac{-\alpha x}{H}\right), \tag{5.7}$$

for some constants C and α. Using (5.7) in (5.6) and simplifying further the constant C can be obtained as follows

$$C = \frac{P_{tot} P_{abs} \alpha}{2H(1 - \exp(-\alpha))}. \tag{5.8}$$

Considering the fact that heating happens only in $0 \leq x \leq H$ until $t = t_{off}$, where t_{off} is the time the laser turns off, the expression for Q becomes

$$Q(x) = \begin{cases} \tilde{Q}(x)\left(1 - \mathcal{H}(t - t_{off})\right), & 0 \leq x \leq H, \\ 0, & x > H, \end{cases} \tag{5.9}$$

where

$$\tilde{Q}(x) = \frac{P_{abs} P_{tot} \alpha}{2H\left(1 - \exp(-\alpha)\right)} \frac{\exp(-\alpha\, x/H)}{S(x)}, \tag{5.10}$$

and $\mathcal{H}$ is the Heaviside function defined by

$$\mathcal{H} = \begin{cases} 0, & t < t_{off}, \\ 1, & t \geq t_{off}. \end{cases} \tag{5.11}$$

We next define the effect of cooling in the domain of x. Generally, cooling of a fibre involves three modes of heat transfer, i.e., conduction, convection and radiation. The heat transfer by conduction is the flow of heat per unit time and per unit area, within the glass, which depends upon the temperature gradient $\partial\theta/\partial x$. When the temperature gra-

dient is large, conduction is important. Heat loss to the surroundings due to convection is commonly known as Newton cooling, and Newton's law of cooling is used to model this process. This form of cooling refers to the amount of heat transferred from a solid surface to the surrounding fluid or gases per unit time and area. The mode of heat transfer by radiation is due to electromagnetic waves, or photons. One noticeable difference between conduction and convection over radiation is the dependence of heat transfer on temperature. While the heat transfer rate is typically assumed to be linearly proportional to the temperature gradient or difference in the case of conduction and convection, respectively, in the case of radiative transfer, it is proportional to the difference in temperature to the fourth power, i.e.,

$$Q \propto (\theta^4 - \theta_0^4). \tag{5.12}$$

As a result, radiative heat transmission becomes increasingly essential as the temperature rises, and may even completely dominate conduction and convection at extremely high temperatures (Modest 2013). Additionally, the internal molecules of the glass tube may contribute to the radiation phenomenon by producing and absorbing photons in a certain range of wavelengths. As a result, energy transmission depends on the glass composition and the size of the medium. While this mechanism seems likely for laser heating, it is less certain in the glass tapering process because of the small dimensions involved in the glass tube. Although Chouffart (2018), and the references therein, demonstrate the use of this mechanism, they also mention that, in the case of the fibre drawing process, all studies have omitted the effects of internal radiation on cooling due to the small dimensions of the fibres and the complexity of generating the numerical simulations. Here we assume the glass tube is cooled radiatively and is optically thick for wavelengths that dominate heat transfer only at the external boundary of the thread (Modest 2013).

Thus, on the external boundary, we assume the boundary condition

$$-k\nabla\theta \cdot n^{(0)} = \mathcal{F}(\theta(x,t)), \tag{5.13}$$

where $\mathcal{F}(\theta(x,t))$ is the radiative heat transfer rate, assumed as

$$\mathcal{F}(\theta(x,t)) = \begin{cases} k_b\beta(\theta^4 - \theta_a^4)\,\mathcal{H}(t - t_{off}), & 0 \le x \le H, \\ k_b\beta(\theta^4 - \theta_a^4), & x > H, \end{cases} \tag{5.14}$$

in which k_b is the Stefan-Boltzman constant, β is the emissivity of the surface, and θ_a is the ambient temperature beyond heater, which are assumed to be constants. Considering the slenderness of the tube and rapid heating of the cross-section induced by the laser on the external wall of the tube, we assume no heat flux through the internal boundary,

$$-k\nabla\theta \cdot n^{(1)} = 0, \quad G^{(1)}(x,t) = 0. \tag{5.15}$$

5.3.1 Asymptotic temperature modelling

Assuming the slenderness of the glass tube and defining $\epsilon = \sqrt{S_0}/H \ll 1$, where $\sqrt{S_0}$ is the square root of the cross-sectional area at $t = 0$ and H is the heated length, we introduce the scaled variables, considering $\hat{F} = 1$ as in Chapter 4, denoted by hats as follows

$$\mu = \mu_{hot}\hat{\mu}(\hat{\theta}), \quad \theta = \theta_a + \Theta\hat{\theta}, \quad Q = \frac{k\Theta}{H^2}\hat{Q}, \tag{5.16}$$

where $\Theta = (\theta_{hot} - \theta_a)$, θ_a is the ambient temperature, θ_{hot} is a characteristic temperature (close to the softening point) and μ_{hot} is a characteristic viscosity scale corresponding to temperature θ_{hot}. Following Stokes et al. (2019), writing (5.3) in terms of the scaled variables of (5.16) and those previously defined in (4.12) we obtain the scaled temperature

equation as follows by dropping the hats for convenience,

$$\epsilon^2 \mathrm{Pe}\left(\frac{\partial\theta}{\partial t} + u\frac{\partial\theta}{\partial x} + v\frac{\partial\theta}{\partial r}\right) = \epsilon^2\frac{\partial^2\theta}{\partial x^2} + \frac{1}{r}\frac{\partial}{\partial r}\left(r\frac{\partial\theta}{\partial r}\right) + \epsilon^2 Q, \tag{5.17}$$

where

$$\mathrm{Pe} = \frac{\rho c_p F H^2}{6\mu_{hot} S_0 k}, \tag{5.18}$$

is the Peclet number. We now non-dimensionalise (5.10) using the scaled variables and obtain

$$\tilde{Q}(x) = \frac{P_{abs}P_{tot}\alpha H}{2k\Theta(1-\exp(-\alpha))S_0}\frac{\exp(-\alpha x)}{\chi^2(x)}. \tag{5.19}$$

Proceeding further we next scale (5.13), to obtain the dimensionless boundary condition on the external surface of the glass tube

$$-\left(\epsilon^2\frac{\partial\theta}{\partial x}n_x^{(0)} + \frac{1}{r}\frac{\partial(r\theta)}{\partial r}n_r^{(0)}\right) = \epsilon^2\mathrm{Pe}\mathcal{H}_R\mathcal{F}_s(\theta), \tag{5.20}$$

where

$$\mathcal{F}_s(\theta) = \begin{cases} \left[(\theta+\vartheta_a(1-\theta))^4 - \vartheta_a^4\right]\mathcal{H}(t-t_{off}), & 0 \le x \le 1, \\ \left[(\theta+\vartheta_a(1-\theta))^4 - \vartheta_a^4\right], & x > 1, \end{cases} \tag{5.21}$$

and

$$\mathcal{H}_R = \frac{6\mu_{hot}\sqrt{S_0}\beta k_b \theta_{hot}^4}{F\Theta\rho c_p}, \tag{5.22}$$

is the dimensionless parameter that represent the importance of radiative cooling and

$$\vartheta_a = \frac{\theta_a}{\theta_{hot}}, \tag{5.23}$$

is the scaled ambient air with respect to θ_{hot}. On the internal boundaries, the scaled boundary condition takes the form

$$-\left(\epsilon^2\frac{\partial\theta}{\partial x}n_x^{(1)} + \frac{1}{r}\frac{\partial(r\theta)}{\partial r}n_r^{(1)}\right) = 0. \tag{5.24}$$

Expanding all the dependent variables in powers of ϵ^2 gives

$$\theta = \theta_0 + \epsilon^2\theta_1 + \epsilon^4\theta_2 + \ldots, \tag{5.25a}$$

$$u = u_0 + \epsilon^2 u_1 + \epsilon^4 u_2 + \ldots, \tag{5.25b}$$

$$v = v_0 + \epsilon^2 v_1 + \epsilon^4 v_2 + \ldots. \tag{5.25c}$$

As is typical in the modelling of fibre drawing problems, and as discussed in Chapter 2, exploiting the fact that $\epsilon \ll 1$ is simpler to deal with than the full equations. Substituting (5.25) into the temperature equation (5.17) and boundary conditions (5.13), to obtain the leading order terms gives

$$\frac{1}{r}\left(\frac{\partial(r\theta_0)}{\partial r}\right) = 0, \tag{5.26a}$$

$$\frac{1}{r}\left(\frac{\partial(r\theta_0)}{\partial r}\right) n_r^{(i)} = 0, \quad i = 0, 1. \tag{5.26b}$$

which implies that the leading order temperature is independent of the cross-plane position, and thus depends on the axial position x and time t. This is also applicable to the viscosity $\mu(\theta_0)$, as it is a function of temperature. As shown previously in Section 2.2.2, $u = u_0(x, t)$, i.e., the leading order axial velocity is independent of the cross-plane position and thus are functions of axial position and time.

Returning to the leading order equations for temperature (5.17) and considering $O(\epsilon^2)$ terms, recalling that temperature and velocity are independent of the axial position, we obtain the equation that governs temperature at the leading order as

$$\mathrm{Pe}\left(\frac{\partial\theta_0}{\partial t} + u_0\frac{\partial\theta_0}{\partial x}\right) = \frac{\partial^2\theta_0}{\partial x^2} + \frac{1}{r}\left(\frac{\partial}{\partial r}\left(r\frac{\partial\theta_1}{\partial r}\right)\right) + Q, \tag{5.27}$$

along with the boundary conditions (5.20)

$$-\left(\frac{\partial\theta_0}{\partial x}n_x^{(0)}+\frac{1}{r}\frac{\partial}{\partial r}\left(\frac{r\theta_1}{\partial r}\right)n_r^{(0)}\right)=\mathrm{Pe}\mathcal{H}_R\mathcal{F}_s(\theta_0), \tag{5.28}$$

and (5.24) for the inner channel as

$$-\left(\frac{\partial\theta_0}{\partial x}n_x^{(1)}+\frac{1}{r}\frac{\partial}{\partial r}\left(\frac{r\theta_1}{\partial r}\right)n_r^{(1)}\right)=0. \tag{5.29}$$

The leading order temperature equation (5.27) can be simplified by integrating over the cross-sectional area at the axial position and using the divergence theorem and the boundary conditions in (5.28) and (5.29) resulting in

$$\left(\frac{\partial\theta_0}{\partial t}+u_0\frac{\partial\theta_0}{\partial x}\right)=\frac{1}{\mathrm{Pe}\chi_0^2}\frac{\partial}{\partial x}\left(\chi_0^2\frac{\partial\theta_0}{\partial x}\right)-\frac{\mathcal{H}_R\Gamma_0^{(0)}}{\chi_0^2}\mathcal{F}_s(\theta_0)+\mathcal{Q}, \tag{5.30}$$

where $\mathcal{Q}$ is given by

$$\mathcal{Q}(x(\tilde{x},t),t)=\frac{Q}{\mathrm{Pe}}=\begin{cases}\mathcal{C}\exp(-\alpha x)/\chi^2\left(1-\mathcal{H}(t-t_{off})\right), & 0\le x\le 1,\\ 0, & x>1,\end{cases} \tag{5.31}$$

with

$$\mathcal{C}=\frac{3\mu_{hot}P_{tot}\alpha P_{abs}}{\Theta\rho c_p FH(1-\exp(-\alpha))}, \tag{5.32}$$

and $\Gamma_0^{(0)}$ is the length of the external boundary of the cross-section at the leading order, which can be obtained by solving for the cross-plane flow.

Using the parameters for pulling emitters discussed in this thesis, $\mathrm{Pe}\sim O(10)$; therefore, we may neglect the second order term relating to heat conduction from the temperature equation (5.30). Accordingly, incorporating the aforementioned notations (after dropping the zero subscript) we obtain the temperature equation for the whole domain as

$$\frac{D\theta}{Dt}=\mathcal{Q}(x,t)-\frac{\mathcal{H}_R\tilde{\Gamma}^{(0)}}{\chi}\mathcal{F}_s(\theta), \tag{5.33}$$

where $\tilde{\Gamma}^{(0)} = 2\pi\tilde{R} = 2\sqrt{\pi}/\sqrt{1-\phi^2}$, as $\tilde{R} = 1/\sqrt{\pi(1-\phi)}$ in a domain of unit cross-sectional area, and $D/Dt = \partial/\partial t + u_0\,\partial/\partial x$, giving the time rate of change of θ following a moving cross-section $\tilde{x}$.

While the model we develop is applicable for arbitrary viscosity and temperature relationship, for the sake of precision, we will use the expression in (5.2a) that has been extensively used in the literature to determine the viscosity of silica glass. Thus the scaled viscosity becomes

$$\hat{\mu} = \exp\left(\frac{515400}{G_{cst}}\left(\frac{1}{\theta_a - \Theta\theta} - \frac{1}{\theta_{hot}}\right)\right), \tag{5.34}$$

where θ_a, θ_{hot} are in Kelvin and $G_{cst} = 8.314\text{JK}^{-1}\text{mol}^{-1}$.

5.4 Numerical solutions using temperature-dependent viscosity

In light of the foregoing explanation of the temperature model, we note that the fluid flow model presented in Section (2.2.4) must be coupled with the thermal model discussed in Section (5.3) and the two solved simultaneously. Generally, a numerical solution approach is required, including a discretisation in the time and spatial domains to obtain the evolution of the geometry with respect to physical time t. We will here discuss the solution approach including temperature. With our use of the reduced time variable τ, the temperature model enters the flow model through the viscosity which features only in the equation relating physical time t and τ.

Apart from computations relating to temperature dependent viscosity, the numerical approach described in Section 2.3 for computing the time advancing flow model with an axially variable viscosity remains mostly unchanged. The Lagrangian method of time advancement is still valid and is effective for tracking the position of each cross-section

relative to the heated length. Now we must use the position of each cross-section to determine temperature which then determines the viscosity.

Accordingly, in addition to the numerical procedure explained in detail in Section 2.3, the following modifications have been adopted to improve the mathematical simulations using a temperature-dependent viscosity. First, note that at $t = 0$ glass can be considered a solid that will not flow, and the temperature of the glass can be defined as θ_a. Then, we proceed with a time discretisation of (5.33) to numerically approximate $\theta(\tilde{x}, t)$ inside and outside the heated length for each t using a forward Euler method, given as

$$\frac{\theta_{j,k+1} - \theta_{j,k}}{\Delta t} = \mathcal{Q}_{j,k} - \frac{\mathcal{H}_R \, \tilde{\Gamma}^{(0)}_{j,k}}{\chi_{j,k}} \mathcal{F}_s(\theta_{j,k}), \tag{5.35}$$

where

$$\mathcal{Q}_{j,k} = \frac{\mathcal{C} \exp(-\alpha x_{j,k})}{\chi^2_{j,k}}, \tag{5.36}$$

and the cooling term as

$$\frac{\mathcal{H}_R \, \tilde{\Gamma}^{(0)}_{j,k}}{\chi_{j,k}} \mathcal{F}_s(\theta_{j,k}) = -2\sqrt{\frac{\pi}{(1-\phi^2_{j,k})}} \frac{1}{\chi_{j,k}} \mathcal{H}_R \left[(\theta_{j,k} + \vartheta(1 - \theta_{j,k}))^4 - \vartheta_a^4 \right]. \tag{5.37}$$

The temperature at the next time point is determined using the results of the previous discrete time point t_k for each k, until $k = K$, where $k = 0, 1, \ldots, K$. This way we can acquire an approximate solution for $\theta_{j,k}$ at each time step inside and outside the heater, starting with $\theta(\tilde{x}_j, 0) = \theta_a \ \forall \ \tilde{x}_j$ where $j = 0, 1, \ldots, J$. The temperature-dependent viscosity value at each cross-sectional node in the glass can be computed using the temperature-viscosity relationship in (5.34) as

$$\hat{\mu}_{j,k+1} = \exp\left(\frac{515400}{G_{cst}} \left(\frac{1}{\theta_a - \Theta\theta_{j,k+1}} - \frac{1}{\theta_{hot}} \right) \right). \tag{5.38}$$

Recalling that the solution of the transverse flow problem is defined using the τ variable

and (2.25) and (2.20) are independent of $\tilde{x}$ (see Chapter 2), the algorithm for solving the coupled temperature and flow model numerically for time t_{k+1} is as follows

1. compute $\tau_{j,k+1}$ using finite differencing as in (2.30) for all the cross-sections $\tilde{x}_j$, where $j = 0, 1, \ldots, J$;

2. use $\tau_{j,k+1}$ to interpolate the values for $\hat{\chi}(\tilde{x}, t_{k+1})$ and $\hat{\phi}(\tilde{x}, t_{k+1})$ for each $\tilde{x}_{j,k+1}$ using the `deval` option in MATLAB `ode45` solver;

3. compute $x_{j+1,k+1}$ using (2.31) for $j = 0, 1, \ldots, , J-1$;

4. compute $\theta_{j,k+1}$ using (5.35) for $j = 0, 1, \ldots, J$;

5. update the viscosity $\hat{\mu}_{j,k+1} = \hat{\mu}(\theta_{j,k+1})$ at each $\tilde{x}_j$ node by substituting the calculated nodal temperatures into equation (5.38);

6. stop if $\max(\theta_{j,k+1}) \leq \theta_a$ (or use another suitable stopping criterion) for $j = 0, 1, \ldots, J$.

The above steps from 1-5 should be repeated until the maximum temperature at each node ($\tilde{x}_j$) is less than or equal to the initial temperature (θ_a), or the viscosity is high enough to prevent any further deformation, thereby reducing the computational time. The reason for selecting this stopping criterion is discussed in more detail in Section 5.4.1. The numerical method we discuss here is a time stepping process in which we store and use the previously-computed numerical solutions for $\chi_{j,k} = \chi(\tilde{x}_j, t_k)$, $\phi_{j,k} = \phi(\tilde{x}_j, t_k)$, $\tau_{j,k} = \tau(\tilde{x}_j, t_k)$, $x_{j,k} = x(\tilde{x}_j, t_k)$, $\theta_{j,k} = \theta(\tilde{x}_j, t_k)$, and $\hat{\mu}_{j,k} = \hat{\mu}(\theta_{j,k})$ for $k = 1, 2, \ldots$ at each mesh node $\tilde{x}_j$ for $j = 0, 1, \ldots, J$, in order to evaluate the numerical solution at the next discrete time point for each mesh node. The forward Euler expansion is extremely convenient for computing numerical solutions when used in conjunction with a Lagrangian setting of tracking each cross-section, requiring only a small amount of

additional computer memory to store the computed variables at each mesh node for the subsequent computations.

We must set the final time t_K sufficiently large to enable complete cooling of the tube and must obtain the solution to (2.32) over a sufficiently large τ range, i.e. for a sufficiently large value I, to enable the interpolations of Step 2 of the above time-stepping procedure for all $\tau_{j,k}$ computed in Step 1. If, however, for some $\tau_{j,k}$ the value exceeds the maximum possible such that the internal channel closes, the tube bursts, or the fibre breaks, we simply stop our solution procedure and adjust the final time.

5.4.1 Numerical solutions

The final model, which couples flow and temperature models, is comprised of the system of first order ODEs given in (2.25), (2.20), (5.33), (5.34), (2.12) and (2.18). A numerical solution is therefore necessary to solve this fully coupled system of differential equations. To generate these numerical computations in the ongoing study of this section, we will use the properties of silica, (obtained from Jasion et al. (2015) and the references therein), and the dimensions summarised in Table 5.1, unless otherwise specified. In addition, it is important to point out that the scaled starting temperature for computing the numerical solutions is $\theta_0 = 0.6$ as the glass is effectively solid and unable to deform at dimensionless temperatures below this. Furthermore, we stop computations should the maximum $(\theta(x_j, t_k)) \leq \theta_0$, for all $j = 1, 2, \ldots, J$, at a time t_k less than the specified final time t_k, to avoid unnecessary computation. Fundamentally, when the temperature of the glass drops beyond the softening point, deformation becomes so slow due to the high viscosity that we may consider the glass to be solid.

The parameter α in (5.7) is assigned to reflect the distribution of power over the length

Parameter	symbol	Value	SI unit
Initial length	$L(0)$	5×10^{-3}	m
Surface tension	γ	0.3	N/m
Characteristic viscosity	μ_{hot}	6×10^{5}	Pas
Density	ρ	2200	kg/m^3
Initial outer radius	R	120	μm
Initial aspect ratio	ϕ_0	0.06	-
Heated length	H	3×10^{-3}	m
Specific heat	c_p	1140	J/kgK
Force	F	0.84	N
Emissivity	β	0.885	-
Absorption efficiency factor	P_{abs}	(assume) 0.68	-
Initial temperature	θ_a	293	K
Characteristic temperature	θ_{hot}	2069	K
Universal gas constant	G_{cst}	8.3145	J/Kmol
Stefan Boltzman constant	k_b	5.6×10^{-8}	W/m^{2}K^4

Table 5.1: Summary of the glass properties and pull parameters used for generating numerical solutions (Jasion et al. 2015).

of the glass tube and examine the effect of the power distribution in non-isothermal conditions. From the equation it can be seen that different temperature distributions can be specified by imposing different power distributions specified by the value of α in the glass. Thus, a different α might be used to realise different emitter shapes. To compare the effect on the solution from different values of α, numerical solutions for $\alpha = 0.41, 0.405$ are plotted in Figure 5.2. From the figure it appears that the geometry is quite sensitive to small changes in α. Changing the value of α changes the way in which power is distributed along the length of the tube i.e. as $\alpha \to 0$ distribution is uniform over $0 \leq x \leq 1$; larger α focuses more energy around $x = 0$ and thus affects the distribution of temperature (see Figure 5.3). Given the strong sensitivity of viscosity to temperature, even a small variation in temperature can have a major impact on the viscosity and hence on the glass flow.

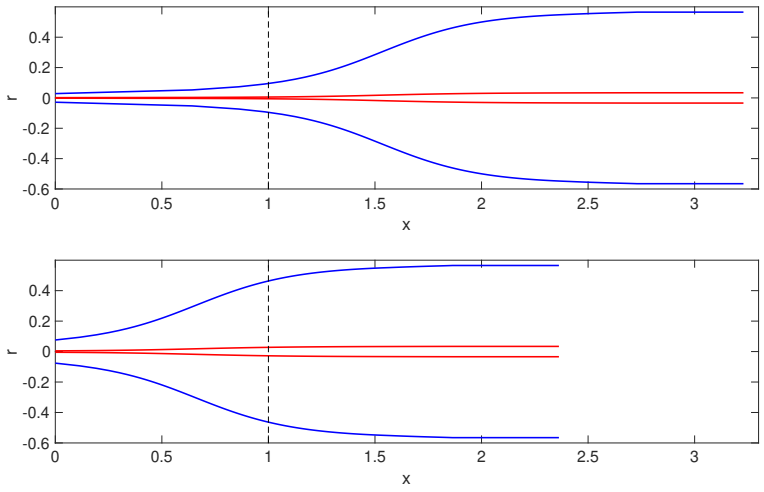

Figure 5.2: Emitter obtained from an axisymmetric tube by pulling with force $\hat{F} = 1$, pressure $\hat{P} = 0$, and $t_{off} = 1.605$ until the stopping criterion is met. The geometry is obtained with the temperature dependent viscosity in (5.38), for laser power $P_{tot} = 2\text{W}$, $\alpha = 0.41$ (top) and $\alpha = 0.405$ (bottom). The outer boundary is shown in blue, and the inner channel is shown in red.

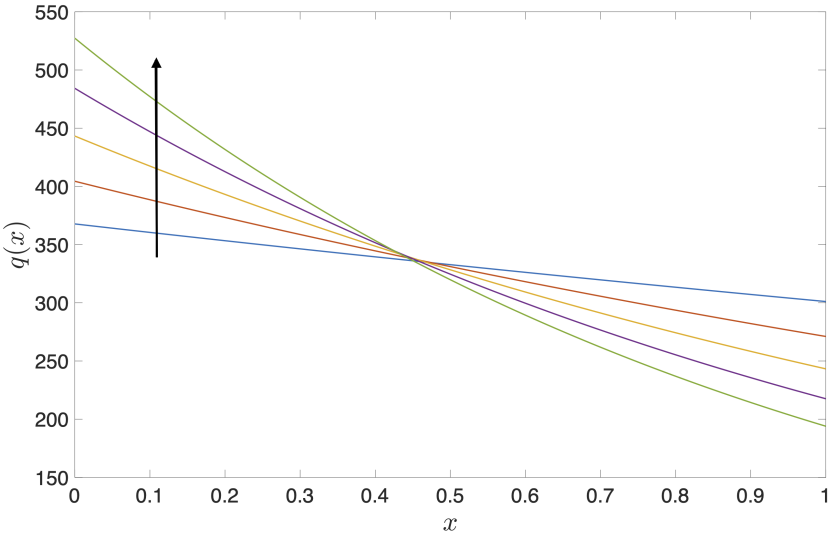

Figure 5.3: Plot of the power distribution $q(x)$ along the length x for different values of α ranging from $\alpha = 0.2, 0.4, \ldots, 1$ in increments of 0.2. The arrow points in the direction of increasing α.

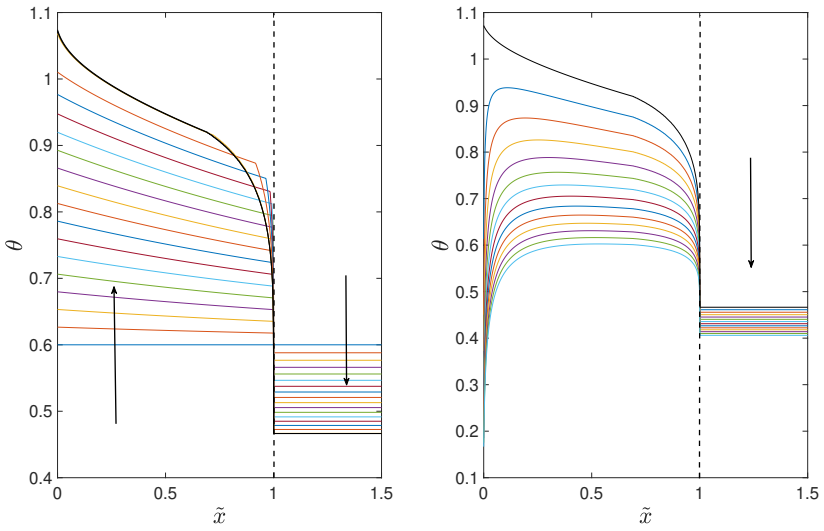

Figure 5.4: Temperature $\theta(\tilde{x}, t)$ of cross-section $\tilde{x}$ over a time range $0 \leq t \leq t_{off}$ (left) when the laser is heating the glass, and (right) over a time range $t > t_{off}$ until the stopping criterion is met when the glass is everywhere cooling. Plotted are the results corresponding to every 100^{th} time step. The arrow points in the direction of increasing time. The black curve in the left graph represents the temperature at $t = t_{off} = 1.605$, the time the heater is turned off, whereas the black curve in the right graph represents the time at $t = 1.606$, the temperature immediately after the heater is turned off. The black dashed line shows the extent $0 \leq \tilde{x} \leq 1$ of the heater at time $t = 0$; cross-sections to the right of this line receive no heating. For $t > 0$ the heated region extends to the value $\tilde{x} < 1$ such that $x(\tilde{x}, t) = 1$. The pull parameters are the same as those used to generate Figure 5.5.

Figure 5.4 (left) shows the change in temperature of the glass $\theta(\tilde{x}, t)$ at cross-sections $\tilde{x}$ at different times t, using the pull parameters that yield the emitter geometry shown in Figure 5.5. Initially all cross-sections are assumed to be at the same temperature $\theta_0(\tilde{x}, 0) = 0.6$. The temperature at a cross-section within the heated region increases and viscosity decreases as time passes, until the heater is turned off at $t = t_{off}$ or the cross-section $\tilde{x}$ exits the heated region. The temperature decreases and the viscosity increases once a cross-section $\tilde{x}$ leaves the heater, due to cooling. When the temperature is sufficiently hot, stretching begins. According to our assumed distribution of power,

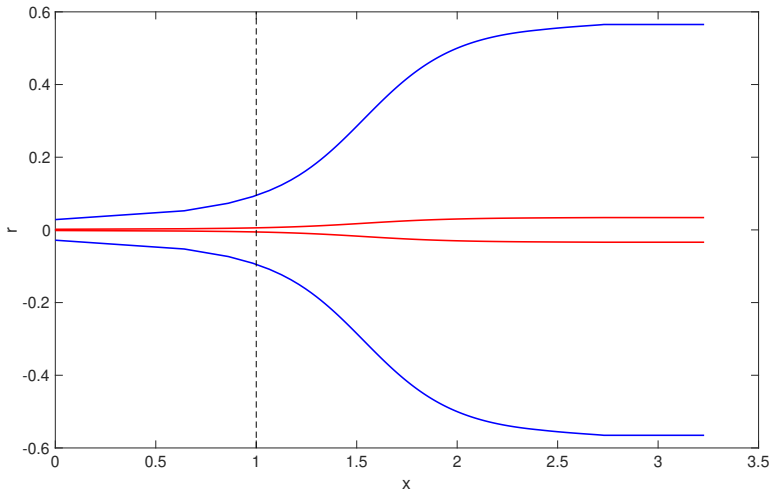

Figure 5.5: Emitter obtained from an axisymmetric tube by pulling with force $\hat{F} = 1$, pressure $\hat{P} = 0$ and $t_{off} = 1.605$ until the stopping criterion is met. The geometry is obtained with the temperature dependent viscosity in (5.38), for $\alpha = 0.41$, and laser power $P_{tot} = 2$W. The outer boundary is shown in blue, and the inner channel is shown in red.

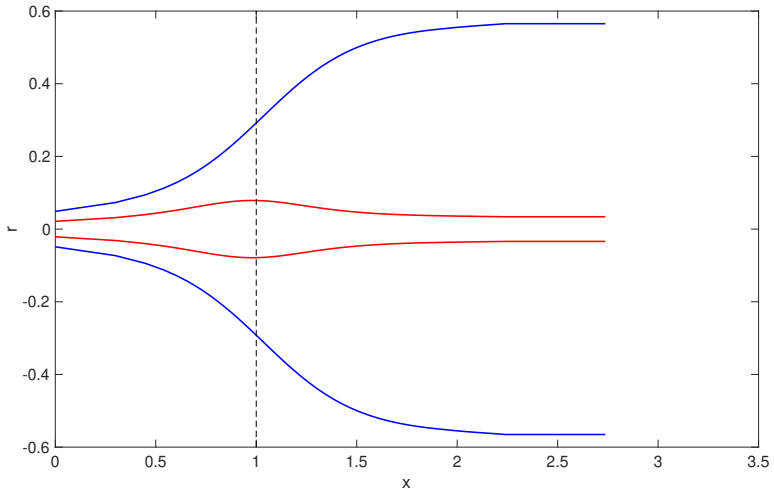

Figure 5.6: Emitter pulled with a pulling with force $\hat{F} = 1$, pressure $\hat{P} = 8$ and $t_{off} = 1.605$ until the stopping criterion is met. The geometry is obtained with the temperature dependent viscosity in (5.38), for $\alpha = 0.41$, and laser power $P_{tot} = 2$W. The outer boundary is shown in blue, and the inner channel is shown in red.

the temperature is hottest in the centre $\tilde{x} = 0$ and decreases along the heater length. As shown in Figure 5.4 (right), when cooling begins after turning the laser off (black curve), the tube cools rapidly and reaches a point where $\theta \leq 0.6$ everywhere and no further deformation occurs. Cooling occurs rapidly in the centre $\tilde{x} = 0$, where the tube is smallest and there is less thermal mass, while cooling is slower in the region with thicker glass. Thus, when determining the stopping condition, we cannot simply look at the cross-section at the centre or $x = \tilde{x} = 0$. This is because this cross-section cools the fastest and becomes solid at a time when cross-sections in the region of thicker glass are still hot and are still deforming. As a result, checking the cross-section at the centre alone is insufficient; we must check all cross-sections to ensure that they have all returned to the starting temperature ($\theta_0 = 0.6$), which serves as the stopping condition. Introducing a stopping criterion reduces computational time and space considerably, as it reduces unnecessary computations.

To demonstrate the shape of the emitter under the influence of temperature dependent viscosity, Figure 5.5 shows the evolution of the geometry as temperature changes as in (5.33) where $\alpha = 0.41$ and with no pressurisation of the inner channel. In comparison with the shape of the emitter in Figure 4.5 derived using the axially variable viscosity function (3.2), the tip has a longer tapered region all the way to the very tip which is narrower; with the axially varying viscosity function the region near the tip is much straighter. Note that without pressure, the inner channel is nearly closed, i.e. ϕ is near 0, and we could choose a positive pressure to prevent this. Figure 5.6 shows the geometry for the same initial tube and draw parameters excepting that positive pressure is used. In comparison with the outcome without pressure, the total area at the tip has increased and become less narrow, and the overall tip length has decreased. This demonstrates that pressure has an effect on heating and hence, on the overall deformation. The effect of bulging appears

in the inner channel due to the application of pressure.

5.4.2 The effect of inner channel pressurisation on the bulge

Although the motivation of this thesis is to use pressure in the heat and pull process to develop an emitter with a uniform inner channel that will maintain continuous flow without becoming blocked, adding pressure to keep the channel size at the tip also causes the inner channel to bulge along its length. By allowing for some flexibility in the required dimension of the inner channel at the tip, the effect of inner channel bulging can be reduced. Thus, in this section, we will analyse the pressure and the resulting inner channel quantitatively in order to acquire a better understanding of pressure magnitude on channel geometry and the deviation from the initial radius along its length.

Figure 5.7 compares the evolution of the inner channel radius and outer radius over the length x corresponding to six different pressure values. Table 5.2 lists the important information from Figure 5.7 such as the dimensional values of the inner radius at the tip, the reduction of the inner channel radius at the tip ($\phi_T R_T$) as a percentage of the initial dimension ($\phi_0 R_0$), the maximum bulge radius as a percentage of the initial tube radius, the wall thickness at the tip and the pressure in kilo pascal to obtain the inner channel at those dimensions.

The pressure has a noticeable effect on the deformation of the inner channel, with high pressure generating shorter tip lengths than low pressure. As pressure decreases, the bulge moves away from $x = 0$ and the taper increases in length. The location of the bulge can be explained by the localisation of the heat. In our model, heat is dispersed in such a way that the central area receives the most heat. As a result, it is more fluid in the centre and hence deforms more easily, necessitating a greater amount of pressure to

$\phi_T R_T$ (μm)	$\phi_T R_T$ (reduction at the tip)	Bulge	W_T (μm)	Pressure (KPa)
7.2027	0%	282%	6.0464	27642
5.4240	25%	251%	5.9164	25996
3.6175	50%	210%	5.7194	23325
1.8373	75%	151%	5.4945	17859
0.7846	90%	104%	5.5107	9162
0.4203	95%	-	5.6330	1895

Table 5.2: Relationship between $\phi_T R_T$, reduction of $\phi_T R_T$ as a percentage, size of the bulge, and the required pressure for Figure 5.7.

keep it open. If it is important to preserve the hole's original dimension at the tip, the pressure requirement is quite high, resulting in a larger bulge. The best pressure depends on the requirement at the tip and the acceptable variation in the channel radius along the tip length. This will be determined by practical application, for example whether a bulge leads to fluid mixing. As seen in Table 5.2, a high dimensional pressure is required to maintain the channel's original dimension at the tip. From (4.12) pressure is directly related to force and thus, a reduction in force may reduce the requirement for pressure.

5.4.3 Effect of a different power distribution

From the analysis so far, it is apparent that the distribution of power plays an important role in the deformation. In fact, it is the primary factor that determines the distribution of temperature, which causes the deformations. All the numerical solutions we have considered in Section 5.4.1 are derived using the power distribution defined in (5.7) using an exponential function. It is interesting to analyse the way in which the geometry changes as the temperature profile along the glass changes. Therefore, in the ongoing analysis, we compare the influence of a different power distribution, and thus temperature variations,

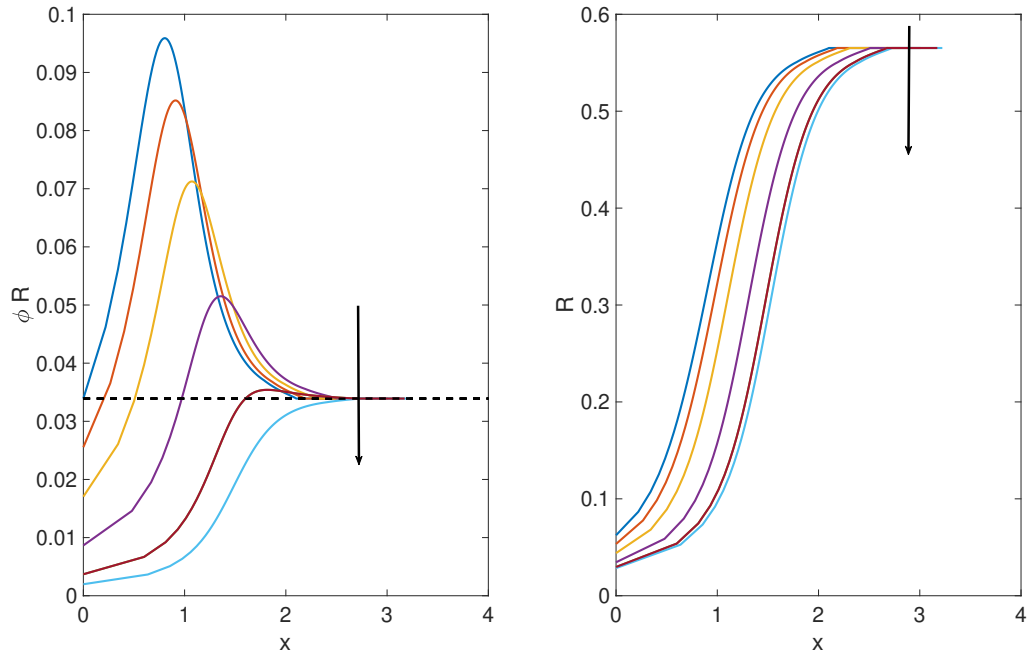

Figure 5.7: Plot of inner boundary ϕR (left) and outer boundary R (right) as a function of x for (top to bottom in direction of arrow) $\hat{P} = 8.90, 8.37, 7.51, 5.75, 2.95, 0.61$ respectively, and $t_{off} = 1.605$ with the tube pulled until the stopping criterion is met. We have (top to bottom) $(0, \phi_T R_T) = 0.0339(100\%), 0.0254(75\%), 0.0169(50\%), 0.0085(25\%), 0.0034(10\%), 0.0017(5\%)$. The percentages indicate the reduction in the inner channel radius relative to its initial dimension of $(\phi_0 R_0, 0) = 0.0339$. The black dashed line on the left graph indicates the dimension of the initial inner radius. The results are obtained using the temperature dependent viscosity in (5.38), for $\alpha = 0.41$, and laser power $P_{tot} = 2$W.

on the final outcome.

The exponential function seems to have worked well in determining the temperature distribution along the heated region of the glass, yielding a small wall thickness at the tip with a neck down as required in the final shape of an emitter. We now consider a cosine function, which can also be integrated easily, to compare the effect of a different power distribution on the final geometry. The approach of deriving the heat equation in this case is similar to that which was used previously to obtain (5.33) ($0 \leq x \leq 1$) and

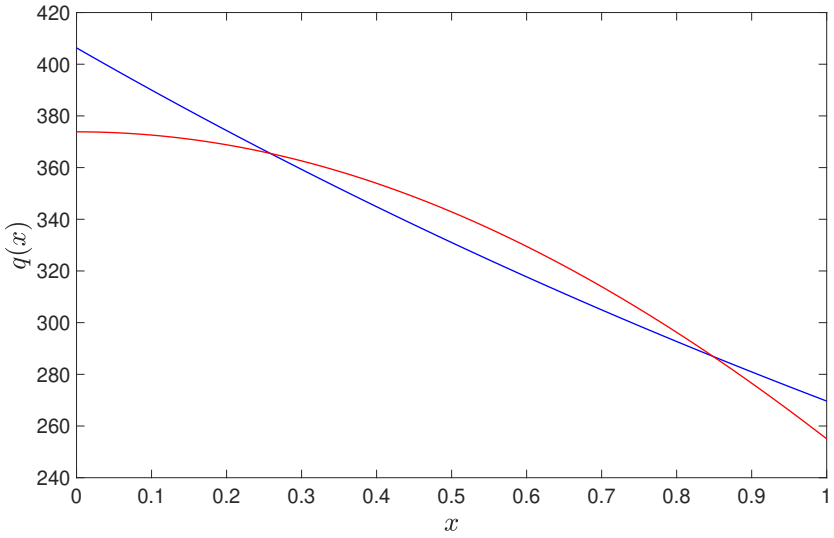

Figure 5.8: A comparison of power distribution per unit length over the length of the heater for two different functions, where $\alpha = 0.41$ and $P_{tot} = 2$W. The blue line represents the expression for when $q(x)$ is approximated using an exponential ($q_1(x)$) and red represents the expression for the cosine function ($q_2(x)$).

requires only a simple modification to the (scaled) power distribution given as follows:

$$q(x) = C\,\cos(2\alpha x), \tag{5.39}$$

which modifies the expression for C to

$$C = \frac{P_{tot}\alpha}{H\sin(2\alpha)}. \tag{5.40}$$

Using (5.39) and (5.40) a similar relation for $\mathcal{Q}$ as in (5.31) for $0 \leq x \leq 1$ is obtained as

$$\mathcal{Q} = \frac{6P_{tot}P_{abs}\mu_{hot}\alpha}{\Theta H\rho c_p F\sin(2\alpha)}\frac{\cos(2\alpha x)}{\chi^2}. \tag{5.41}$$

In Figure 5.8 we show the power distribution per unit length as given by the cosine and exponential functions. For both functions, power, hence temperature, decreases from $x = 0$ to $x = 1$. Notice that $q_1(x)$ decreases approximately linearly whereas $q_2(x)$ decreases

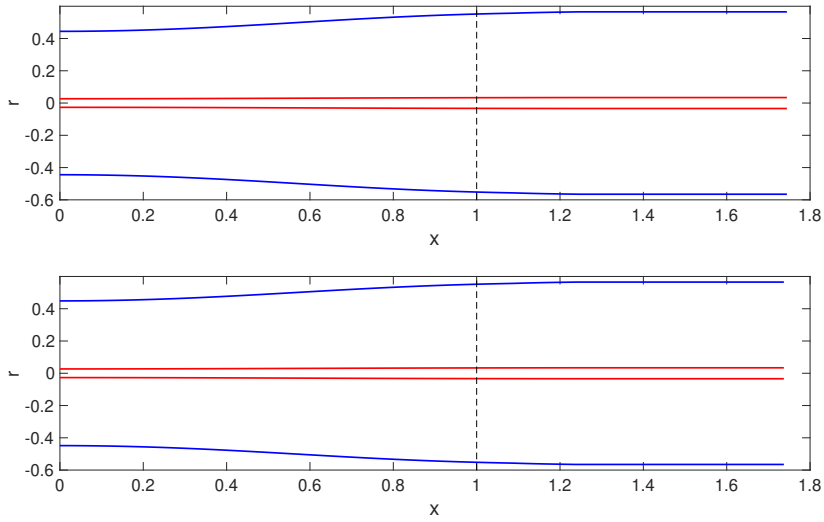

Figure 5.9: Emitter obtained from an axisymmetric tube by pulling with force $\hat{F} = 1$, pressure $\hat{P} = 0$ and $t_{off} = 1.605$ until the stopping criterion is met. The geometry is obtained with the heating function in (5.41), for a laser power $P_{tot} = 2\text{W}$, $\alpha = 0.41$ (top) and $\alpha = 0.405$ (bottom).

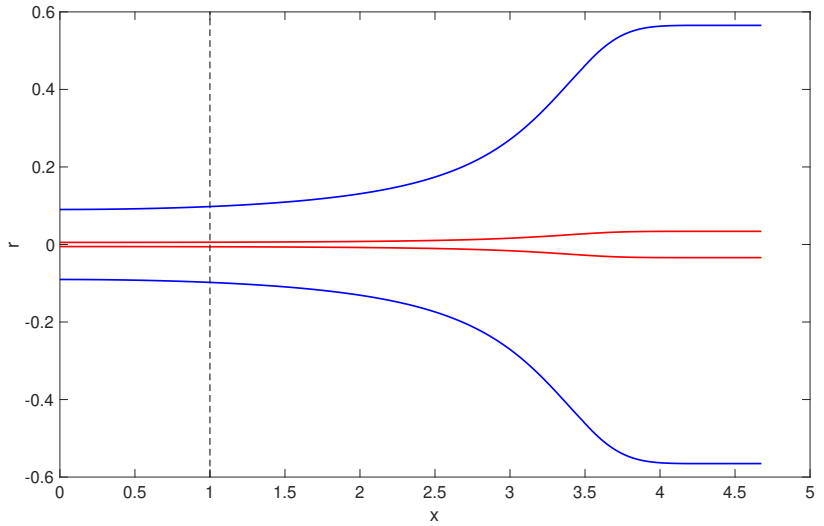

Figure 5.10: Emitter obtained from an axisymmetric tube by pulling with force $\hat{F} = 1$, pressure $\hat{P} = 0$ and $t_{off} = 1.605$ until the stopping criterion is met. The geometry is obtained with the heating function in (5.41), for a laser power $P_{tot} = 2\text{W}$ and $\alpha = 0.53$.

non linearly and gives a more uniform temperature over the heated length.

Figures 5.2 and 5.9 compare the shape of the emitter for the two different heating functions pulled from the same initial tube using the same pull parameters. The results look completely different for the two different power distributions. In the latter case the more uniform temperature distribution results in less stretching/deformation. Recall that in Figure 5.2 the geometry was very sensitive to the value of α and a slight change in α resulted in a considerable difference in both the overall length and the size of the tip. In comparison to the geometry from the exponential function, the two results in Figure 5.9 are more similar, demonstrating that there is much less sensitivity to α compared with the case of the exponential power distribution.

In order to see how the results change for different α, Figure 5.10 shows the geometry of the emitter for a comparatively larger value of α. As before, the length of the tip increases with increasing α. However, notice that the tip is more straight (not sharp) over a longer region, unlike the results delivered from the power distribution defined by the exponential profile. This is a result of a more uniform temperature profile.

5.5 Summary

The focus of this chapter has been to develop a coupled flow and temperature model of the heating and pulling process and use it to investigate the effect of temperature-dependent viscosity. After a brief review of the temperature dependence of the material properties of silica glass required in the temperature models, we developed the temperature equations that govern the temperature variations in both time and space for the heating and cooling stages. All of the material properties of the glass are considered to be temperature-independent, except for viscosity. The strong dependence of the glass viscosity on temperature are determined using the viscosity-temperature relationship given by Doremus (2002) for higher temperature values.

The complete temperature model was developed using fundamental energy conservation principles. Exploiting the slenderness of the tube, we have developed an axisymmetric one-dimensional temperature model, which is independent of the cross-plane problem as, to leading order, the temperature is uniform in a cross-section. The numerical method for producing solutions to determine the evolution of geometry due to temperature-dependent viscosity provides a better understanding of key process parameters on the deformation process. This was achieved by coupling models for axial and pressure-driven cross-plane flows to the temperature model and solving them using MATLAB. Similar to the previous results, with sufficiently large pressure, the aspect ratio of the tube can be increased so as to have the radial dimension of the inner channel at the tip equal to that of the initial tube. We have computed numerical simulations for a prescribed power distribution that determines the distribution of temperature within the heated region. The region of our interest in deformation includes the region between the tip and the transition point (the end of the taper), where there is no deformation beyond this point.

Finally, we compared the numerical solutions obtained using various power distributions to highlight the evolution of the geometry and to demonstrate the effectiveness of the numerical method we have developed for generating these simulations. In doing this we found considerable sensitivity to parameter values. This is consistent with experiments which show quite large changes in emitter geometry for relatively small changes in input parameters. It also reflects the fact that glass viscosity is highly temperature sensitive. We will look more at this in the next chapter.

Chapter 6

Comparison of the model with experiments

6.1 Introduction

The model and the numerical solutions developed in this thesis thus far are useful for analysing the important aspects of industrial manufacturing of emitters using the heating and pulling technique. Although this thesis is primarily concerned with mathematical modelling of the heating and pulling process, experiments which were informed by the modelling were carried out to validate the model. These experiments were conducted by Dr A. Radionova, the Institute for Photonics and Advanced Sensing at the University of Adelaide, and in part performed at the Optofab node of the Australian National Fabrication Facility utilising Commonwealth and SA State Government funding.

When modelling a wide variety of industrial applications, experimental inputs are clearly beneficial to ensure that the model and solutions conform to reality, and to identify advisable and/or necessary improvements to the model. Also, experimental data is needed for estimating unknown parameters in our temperature model. Thus, comparison of the model with experiments enables development of a model able to provide accurate predictions for industrial manufacturing processes.

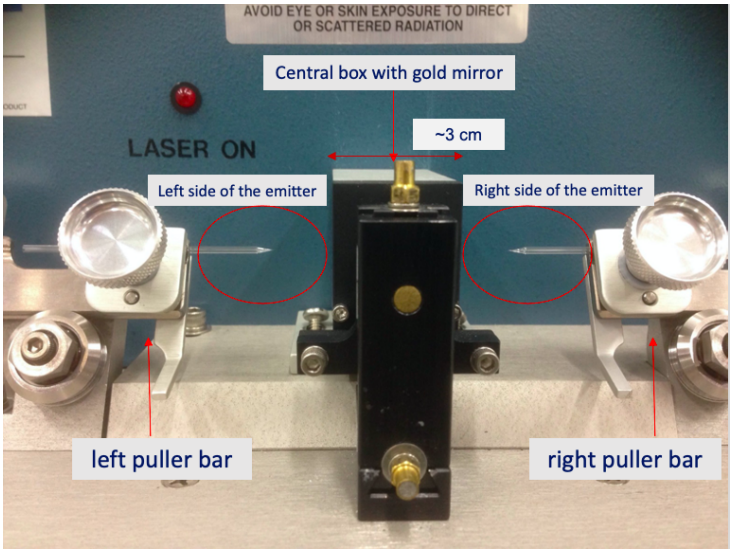

Figure 6.1: Photo of a Sutter Instrument Company P-2000 micro pipette puller provided by and presented with the permission of Dr A. Radionova (Radionova 2019).

The present chapter starts with an introduction to the apparatus and the pull parameters. We then discuss the calibration of the model with experiments to determine suitable quantities for unknowns in the temperature model. Finally we show how the model can be used to predict the final geometry of the emitter and yield information of real benefit at the level of industrial fabrication, for example by identifying suitable pull parameters for a desired outcome. The instrument used for experimental work is the Sutter P-2000 micro-pipette puller (Sutter Instrument Company Co., Novato, CA). This puller uses a CO_2 laser to melt the glass. A photograph of the puller is given in Figure 6.1. Fused silica is the tubing material that is mostly used to fabricate fine tips when fabricating glass emitters. We will provide some comparative results of the model predictions in the final section of this chapter showing numerical solutions against the experimental data to illustrate the accuracy of the developed model and solutions. However, the Sutter P-2000 puller does not enable pressurisation of the tube so the experimental validation of the model is for no applied pressure.

6.2 Experiments and measurements

6.2.1 Overall apparatus

A glass tube made of fused silica (F300) of known initial geometry is first placed horizontally into the puller bars and secured with clamps at both sides. The centre part of the tube goes through the section to be heated by the CO_2 laser. Initially the tube is at room temperature. As the puller program begins, the laser goes to a warm-up position and is turned on, after which the beam is directed at the glass. A reflective scanning mirror (gold coated) focuses the laser beam onto the surface of the glass providing a relatively uniform heat across the glass circumference (Sutter Instrument 2010). The laser heats the glass over a period of several milliseconds (ms), and then turns off, allowing the glass to cool. Heating of the glass by the laser raises the temperature sufficiently that the glass softens, allowing it to be stretched by the gravitational force of a weight (0.171kg/1.68N) (Wang et al. 2016), which is located in the base of the P-2000 puller and connected to both puller bars as shown in Figure 6.2 (Sutter Instrument 2010). After several seconds, the glass tube forms an hour glass shape and eventually breaks into two halves forming two glass emitters at the end of a draw (Sutter Instrument 2010); this can be seen in Figure 6.2.

According to the puller manual (Sutter Instrument 2010), the entire glass deformation process is controlled in the Sutter P-2000 puller by five control parameters: HEAT, FILAMENT, VELOCITY, DELAY, and PULL. Controlling these factors allows for precise control of the shape of the taper and the tip diameter. Thus, it is beneficial to discuss the effect of each of these parameters.

The HEAT parameter (range 0 - 999) controls the heat delivered to the glass. A heat of 100 units corresponds to a power of 0 Watts, whereas a heat of 999 corresponds to a

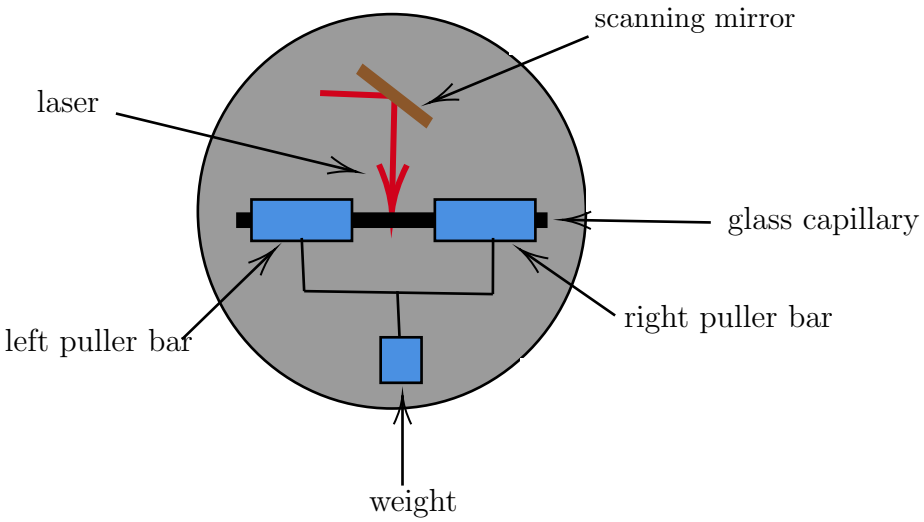

Figure 6.2: Operation of Sutter P-2000 adapted from Sutter Instrument (2010).

power of 10 Watts. In this range, the laser power increases by 1 Watt for each increment of 90 heat units (Wang et al. 2016).

The FILAMENT parameter (range 0 - 5) determines the scanning pattern of the laser which can also be understood as the section of the tube being heated by the laser beam or as the heater length ($2H$) in our model. A FILAMENT of 0,1,2,3,4,5 corresponds to a heated length of 1mm, 1.5mm, 1.9mm, 4.5mm, 6.5mm, and 8mm, respectively (Sutter Instrument 2010). The VELOCITY parameter (range 0 - 255) represents the speed at which the puller bars move as the glass softens due to the weight. As the force acts, the velocity increases until the value reaches the programmed VELOCITY parameter on the instrument. This is called the trip velocity. Each VELOCITY unit is approximately equal to 1/40 mm s^{-1} (Wang et al. 2016). Once the trip velocity has been reached, the

DELAY parameter (range: 0 - 255) controls the time between the deactivation of the laser and the activation of a hard pull (force) determined by the PULL parameter (range: 0 - 255) to increase the pull and break the tube. DELAY is a time in milliseconds. The program stops when the glass tube separates into two halves. If the glass tube does not separate in a pull, the program typically loops until the glass tube separates. More detailed information about the Sutter P-2000 puller and the parameters can also be found in Wang et al. (2016), Sutter Instrument (2010), Radionova (2019).

The sequence of a normal program with the above mentioned parameters is as follows. After fixing the tube in the puller and closing it, the pull button is pressed and the laser goes to a warm-up position and is turned on. After 1 sec the beam is directed at the glass. The centre of the tube is heated for a distance determined by the FILAMENT setting by a voltage-controlled power supply predefined by the HEAT setting. The pulling starts as the glass softens, when the fibre temperature is high enough for significant material flow, and draws apart the two ends under the gravitational force of the weight attached. When the speed of separation of the puller bars reaches the trip velocity as given by the VELOCITY parameter, the program is said to 'trip'. The exact sequence of events that follows depends on the DELAY parameter. Figure 6.3 shows a pull cycle in a program depending on the value of the DELAY parameter. For DELAY $<$ 128, the hard pull is activated at the trip velocity and the glass is heated for an additional time of 128 less DELAY milliseconds after which the laser is deactivated. For DELAY $\geq$ 128, the laser is deactivated when the trip velocity is reached, and the hard pull is activated after DELAY less 128 milliseconds (Sutter Instrument 2010). In this latter case the glass cools somewhat before activation of the hard pull which is more likely to simply break the glass into the two halves and not cause any further stretching. When the DELAY = 128 the hard pull initiates at the same time as the laser is turned off and pulls until the tube breaks

(or separates). A feature of P-2000 is the ability to run multi-line programs where each line in a program gives the settings for the various parameters. For example, in a 2 line program, if the glass tubes are not separated at the end of the first line of the program, the next program line executes. If the glass tube does not separate after executing this line, then the program repeats program line 1 and loops until the tube breaks. The glass tube, however, may separate before executing all the lines of a multi-line programme. For a single line program this process may repeat multiple times until the two halves of the tube separate (Sutter Instrument 2010). When separation occurs, there is a brief message indicating the length of time the glass was heated.

The reset button can be pressed to stop the puller and so might be used to prevent looping if the button can be pressed at the correct time. According to Mr. Graham Brown, Sutter Instrument's Design Engineer (email exchange, May 13, 2020), an alternative to pressing reset is to have a programme line with HEAT = 1 and VELOCITY > 0 (with other parameters of any choice). This line will cause the programme to stall since the glass cannot be melted. As a result, a time out will occur after 57 seconds, and the reset button can be pressed to terminate the programme. In any given cycle, a programme terminates after separation and also after a 57 second time-out.

6.2.2 Timed heat program

Looping through a program may be particularly useful in practice for fabricating geometries (e.g. patch pipettes) that require multiple HEAT cycles, but it is challenging to model because of the limited information provided about looping, such as the loop count and time between loops. We inquired from the Sutter Company as to whether looping could be stopped and on the meaning of a VELOCITY=0 setting. From the discussion

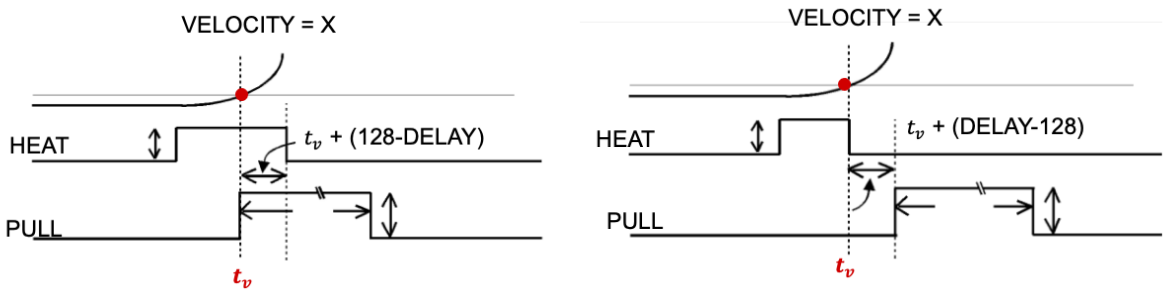

(a) DELAY < 128 (b) DELAY > 128

Figure 6.3: Pull cycle depending on the value of DELAY parameter adapted from Sutter Instrument (2010).

with Mr. Graham Brown, Sutter Instrument's Design Engineer (email exchange, July 16, 2020), it was determined that, when the VELOCITY parameter in the puller is set to zero (VELOCITY = 0), the P-2000 puller operates in a special mode called "Timed heat" mode. In this mode, the laser turns off after a time determined by the DELAY setting: 1 millisecond/unit. More precisely, the time of laser activation can be adjusted in this program setting by adjusting the DELAY parameter. For example, if the DELAY value is 100, the laser will remain on for 100 milliseconds and then turns off. This is a much simpler mode of operation of the puller and gives the ability to run a single line program and stop, whether or not the tube has broken.

In summary, for a timed-heat program parameters are set as follows.

- HEAT is set to a value to give a laser power sufficient to melt the glass. For example if HEAT=280, this corresponds to a 2W power output, as 100 units equal 0W, and each addition of 90 heat units increases the laser power by 1W.

- VELOCITY = 0, provides the configuration for a timed heat program with no looping.

- FILAMENT is set to a desired total heater length, where in the model H is half the

filament length.

- DELAY is set to give the desired heating time.
- PULL will be applied after the DELAY. According to Mr. Graham Brown, Sutter Instrument's Design Engineer (email exchange, December 3, 2020), PULL = 0 is often recommended for timed-heat program. PULL = 0 means pulling with the weight which is approximately 0.84N.

The experimental approach of using a timed heat setting was appealing because it resembled our model, and we adopted this to compare our model to experiments. In this program, we have a choice of changing the FILAMENT, HEAT, PULL and DELAY parameters. However, the puller handbook recommends using FILAMENT = 0 when pulling nanospray emitters and PULL = 0 (as given above), essentially leaving the parameter values for HEAT and DELAY to be chosen. We chose to fix the DELAY also, at 100 milliseconds of heating, and vary only the HEAT parameter.

6.2.3 Limitations in relating the model to experiments

In order to relate our model to the operation of the P-2000 puller, we considered a number of significant aspects of our modelling. To begin with, it is important to note that pressure is not a parameter integrated into this instrument at present, and thus, during the validation process, we set $\hat{P} = 0$ in the model. Viscosity plays one of the most significant roles in the deformation process and in reality the viscosity of the glass depends upon temperature, which in general varies with both the axial position and time. Unfortunately, one of the key downsides of the Sutter puller is the inability to record temperature variations in the glass due to the laser safety measures and the dynamics

of the process itself. The laser beam itself does not have a temperature, and its heat is defined as its power output. The temperature induced in a material is a function of its albedo (a function of the amount of radiation absorbed/reflected) and its specific heat capacity. Experimental results in combination with a coupled flow and temperature model must be used to determine several unknown parameters in the model such as the absorption coefficient/emissivity and the convective cooling coefficient, and a suitable function describing the power density of the laser. Once this calibration of the model is complete, the model can be used to generate useful data for industrial fabrication of the emitters.

We note that our model assumes the entire pulling process is both axisymmetric about the tube axis and symmetric about $x = 0$. However, although experiments were set up to be symmetric about $x = 0$, with the intention to obtain two emitters with the same geometry at the end of a pull, none of the experimental trials supported this premise and, upon additional study, it was discovered that one side of the puller's tightening clamps is lighter than the other due to usage over the years, indicating that the pulling tension is not equal on both sides of the puller. As a result, the experimental data related to the analysis in this thesis corresponds to the dimensions of the emitter from one side (since they were acceptable) and ignores the other.

Finally we note that experiments undertaken using fibres of $150\mu m$ nominal OD, clad with a polyamide coating which had to be stripped from the heated region, were affected by issues such as maintaining static tension between the glass and the holder, alignment difficulties and varying heat distribution depending on the stripped length. Consequently, uncoated fibres with OD of $300.07\pm1.06\mu m$ and ID of $19.35\pm0.96\mu m$ and OD of $305\pm4\mu$m and ID of $27 \pm 2\mu$m were utilised because they are more manageable, especially at the tip, after a pull.

In light of the preceding discussion, it is evident that the experimental data presently available for comparison with the numerical model are not as consistent as desired, despite the considerable effort and care with which they were collected. Certainly, more work is required to refine the instrument and the experimental procedures. However, we will examine in the following sections our modelling approach and how the numerical results compare with the experimental data supplied.

6.2.4 Measurements

The inner diameter (ID) and outer diameter (OD) of the tapers obtained from experiments were measured at approximately fixed lengths from the undeformed end, which is referred to as the $x = 0$ (beginning) position. This method of obtaining experimental data was found to give a good consistency across multiple pulls using the same parameters. However, recall that in the model the tip was always assumed to be at $x = 0$. Thus extra work was needed to adjust the experimental data to suit the requirements of the model. Figure 6.4 compares the method used in experiments to obtain the measurements after a pull (top) and how these measurements are adjusted to be used in the model (bottom).

The dimensional measurements for the experiments were determined using a digital photo taken under a microscope. These were scaled to obtain dimensionless values to make comparisons with the model results. Due to the small sizes of the diameters involved, and the comparatively long lengths of the tapers, multiple photos and measurements of the tips were taken at 5x, 10x, 20x and 50x magnification using the microscope, and the data had to be pieced together. This resulted in more measurement uncertainty. Experiments also revealed that there were variations in the values of OD and ID along the initial length of the tube (before the pull), which can affect the heat distribution and

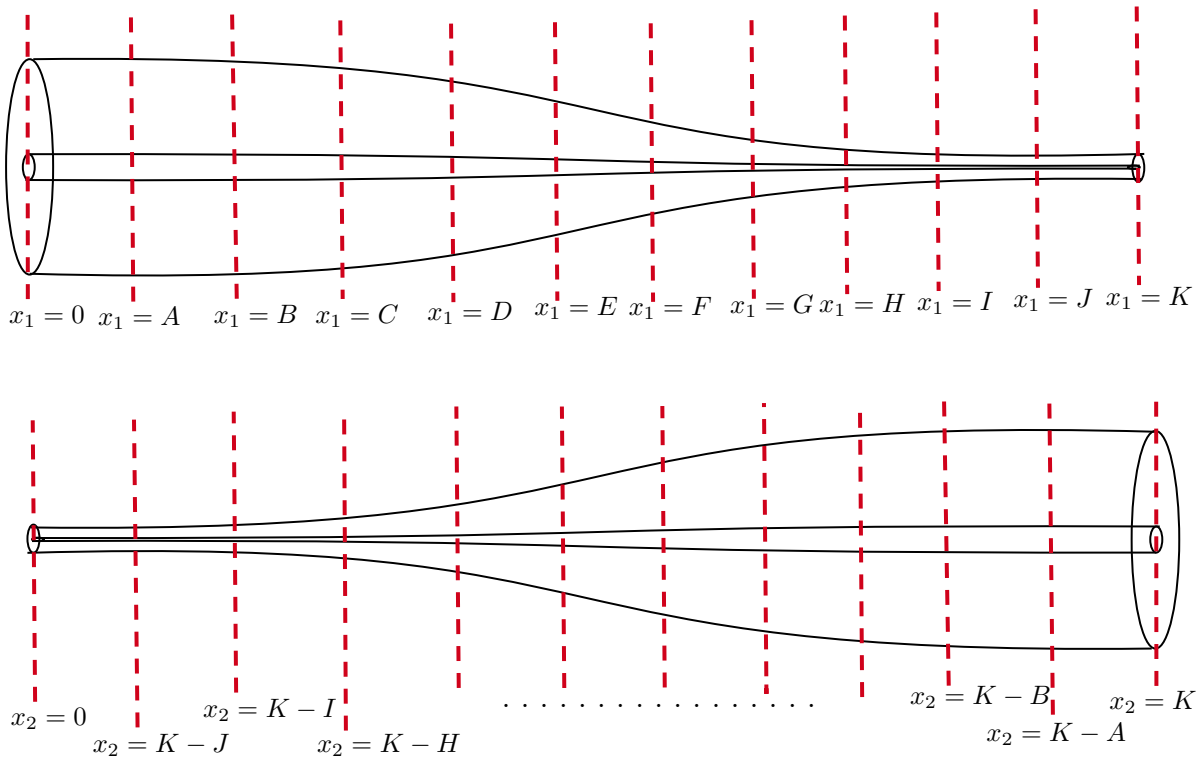

Figure 6.4: The top figure shows how the experimental measurements were taken and the bottom figure shows how these measurements were adjusted to correspond to the model. (Several x_2 values in the bottom figure are removed due to space restrictions).

thus the temperature distribution during a pull. As a result, each time a new experiment is conducted, even with the same power setting, the result may change. Considering these imperfections and the need for experimental measurements at a microscopic level, especially at the tip, rather than comparing the model with a single experimental result, an average of the results over at least three experiments for each of the power setting was used to minimise the effect of experimental variations.

Figure 6.5 shows the shape of an emitter captured using an optical microscope. The experimental data measured from Figure 6.5 using an optical microscope is given in Table 6.1. Notice that at the very tip it is difficult to compare experiments and numerical values due to the very small dimensions and because the tube is pulled until it breaks, which is

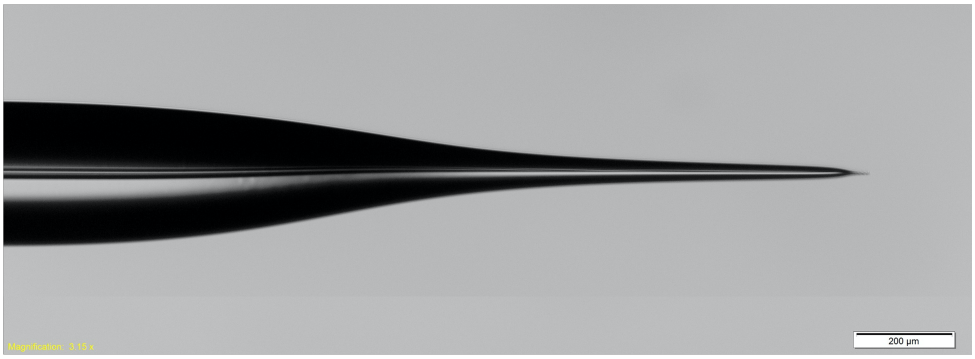

Figure 6.5: Microscopic image of an emitter pulled with HEAT =240. Provided by and presented with the permission of Dr A. Radionova.

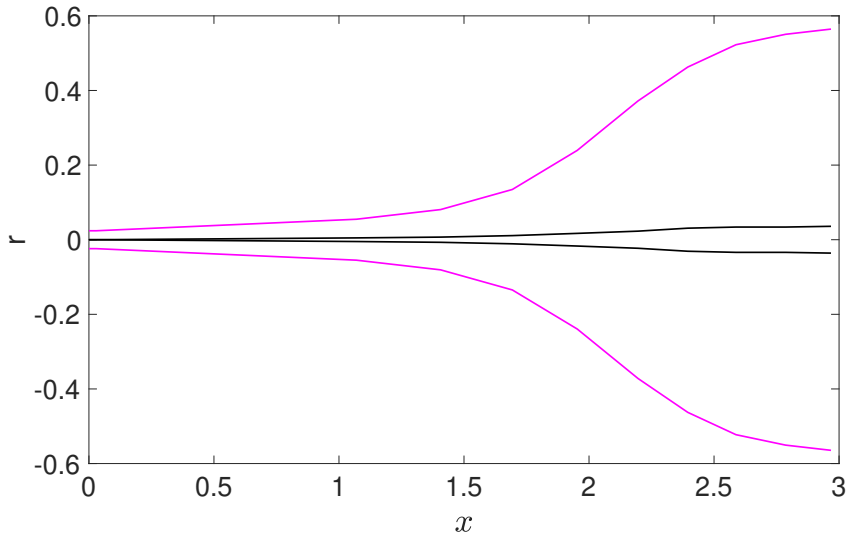

Figure 6.6: Non-dimensional geometry of the emitter generated using the data recorded in Table 6.1 pulled with HEAT =240. The external radius of the emitter is given in magenta and the internal radius is given in black.

not always a clean cut. Although not done in the experiments, we note that, if necessary, the tip could be cut at a position with the desired dimension to remove a completely closed hole or tip. Table 6.2 shows the data adjusted from the row data given in Table 6.1 to adapt the experimental result to the model requirements. The non-dimensional figure plotted after scaling the data points in Table 6.2 is shown in Figure 6.6.

x_1 position	Length (μm)	ID(μm)	OD(μm)
0	0	19.086	300.07
A	154. 276	18.025	292.648
B	322.867	18.025	277.803
C	486.686	16.435	245.994
D	655.806	12.194	197.749
E	862.568	9.013	127.238
F	1083.114	5.832	71.571
G	1326.987	3.711	42.943
H	1410.752	3.181	37.111
I	1613.273	2.588	29.159
J	2497.534	0	12.746
K	2522.495	0	0

Table 6.1: Raw data recorded from the stretching tube experiment in Figure 6.5 pulled with HEAT =240. The column titled "x_1 position " illustrates the experimental measurements of lengths in comparison with Figure 6.4. Data provided by Dr. A. Radionova.

x_2 position	Length (μm)	ID(μm)	OD(μm)
0	0	0	0
K-J	24.961	0	12.746
K-I	909.222	2.588	29.159
K-H	1111.743	3.181	37.111
K-G	1195.508	3.711	42.943
K-F	1439.381	5.832	71.571
K-E	1659.927	9.013	127.238
K-D	1866.689	12.194	197.749
K-C	2035.809	16.435	245.994
K-B	2199.628	18.025	277.803
K-A	2368.219	18.025	292.648
K	2522.495	19.086	300.07

Table 6.2: Data adjusted from that given in Table 6.1. No scaling has been applied.

Experiments have demonstrated that HEAT values less than 230 result in no stretching of the glass tube and just a slight deformation in the centre. At HEAT = 235, a symmetrical hourglass shape is obtained and the tube does not break. It was also found

Parameter	Value
HEAT	230 - 246
VELOCITY	0
DELAY	100
FILAMENT	0
PULL	0

Table 6.3: Pull parameters from the Sutter P-2000

that increments of 2 in the HEAT values are sufficient to introduce small but noticeable changes in the fibre geometry. Importantly, experimental results were found to be reproducible for the same pull parameters. Most of the resulting emitters from the zero velocity program resulted in a long taper length with a conical/hourglass shape. Table 6.3 summarises the draw parameters of the Sutter P-2000 that were used to generate comparative experimental and computational results.

6.3 Relating experiments to the model

With the five parameters that can be managed by the user, there are many ways the puller can be controlled. The most frequently used strategy to change the parameters is to change a single parameter at a time while leaving the others fixed. This demands a considerable number of experimental trials to explore the full parameter space in order to determine the optimal parameter set. Mathematical modelling can be useful in providing guidance in choosing the parameters and later optimising them depending on the requirements. This should reduce the number of trials and, so, minimise materials and labour costs. In this section we first explain how experiments using the timed heat (VELOCITY = 0) program were used to calibrate the model. Then we will explain how the model can be used to make predictions for future experiments.

Viscosity plays an important role in the total deformation process, which changes with the axial position and time in general, such that $\mu(\theta(x,t))$. Although the power supplied to the laser can be determined, the power density of the laser and the fraction of energy absorbed by the glass during an experiment are unknown. Additionally, as the glass leaves the laser, or when the laser is completely turned off, the temperature of the surrounding atmosphere is unknown. In the absence of this information we compared model results for some different choices with experiments and inferred improvements and unknown parameters as described below.

Following a pull, the inner diameter (ID) and outer diameter (OD) of the glass tube measured experimentally were plotted against the model outcomes as explained in Section 6.2.4. The discrepancy between model and experiment indicated how the model needed to be changed for better agreement. To perform a match to the experimental outcome, we use the solution to the full flow model of Chapter 2, with τ defined in terms of $\hat{\gamma}$ (since $\hat{P} = 0$) and with the temperature dependent viscosity model of Chapter 5. Since F is known and can be fixed, we adopt the scales in (5.16) in Chapter 5 and (4.12) in Chapter 4 with $\hat{F} = 1$. With the necessary modifications to allow for experimental analysis of the positive pressure case, it is also possible to apply the model equations of Chapter 4, where τ is scaled with $\hat{P}$ and the influence of surface tension is included or excluded depending on its magnitude.)

A number of different power distribution functions were tried in (5.7) to identify a function that gives reasonable agreement with experimental data. In addition to the equations (5.7) and (5.39) already discussed in Chapter 5, we have tried

$$q(x) = C \tanh\left(\alpha\left(\eta - \frac{x}{H}\right)\right), \tag{6.1}$$

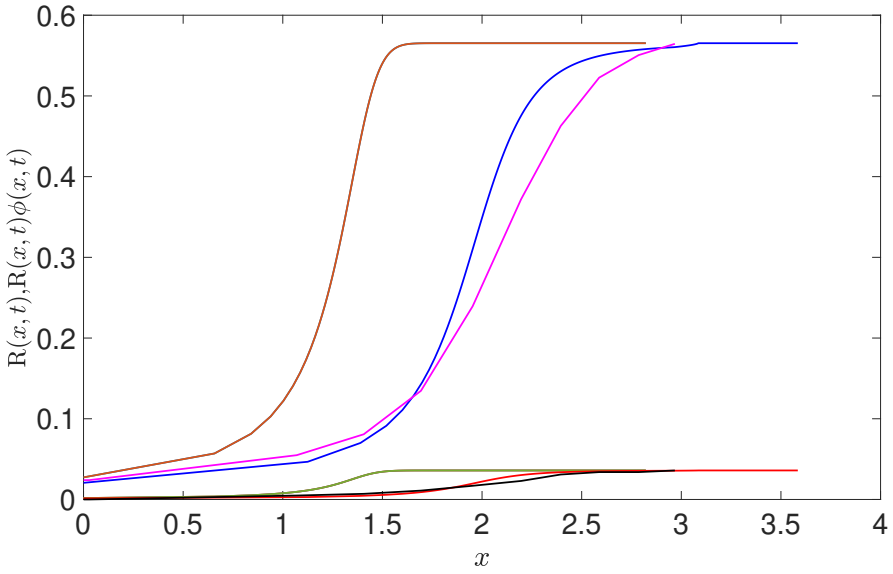

Figure 6.7: A radial slice showing geometry using (6.1) ($R(x,t)$ in orange and $\phi(x,t)R(x,t)$ in green) and (6.2) ($R(x,t)$ in blue and $\phi(x,t)R(x,t)$ in red) against experiments ($R(x,t)$ in magenta and $\phi(x,t)R(x,t)$ in black) where the initial OD $= 300.07\mu$m and ID $= 19.086\mu$m. These results are obtained with HEAT $= 240$, where $\alpha = 0.5$ and $\eta = 0.5$ for (6.1) and $\alpha = 1.15$ for (6.2) respectively.

where C, α and η are fitting constants and a rational function of the form

$$q(x) = C\left(\frac{1}{\alpha\frac{x}{H}+1}\right), \tag{6.2}$$

where C and α are fitting constants. These functions can be integrated easily and, most importantly are decreasing functions, such that the highest power density is at $x = 0$ and the smallest power density is at $x = 1$, matching the assumption we made when developing our temperature model in Chapter 5. From the experimental measurements taken at multiple HEAT values, the power distribution that closely resembled various experimental outcomes was the rational function in (6.2). Figure 6.7 shows how the results compare for (6.1) and (6.2) against the experiment in Figure 6.6. The parameters for the model findings are chosen in this case to ensure a good match with the experiments

Parameter	symbol	Value	SI unit
Initial length	$L(O)$	1.275×10^{-3}	m
Surface tension	γ	0.3	N/m
Minimum viscosity	μ_{hot}	1.5×10^{5}	Pas
Density	ρ	2200	kg/m^3
Heated length	H	0.85×10^{-3}	m
Specific heat	c_p	1140	J/kgK
Force	F	0.84	N
Emissivity	β	0.8	-
Absorption efficiency factor	P_{abs}	(assume) 0.76	-
Initial temperature	θ_a	293	K
Maximum temperature	θ_{hot}	2169	K
Universal gas constant	G_{cst}	8.3145	-
Stefan Boltzman constant	k_b	5.6×10^{-8}	W/m^{2}K^4

Table 6.4: Summary of the pull parameters used for generating numerical solutions (Sutter Instrument 2010, Jasion et al. 2015).

at the tip. Notice that while the dimension of the external radii $R(x,t)$ at the tip are similar in all three situations, the overall deformed length of the tube closely matches the values obtained using (6.2). Thus, in this thesis, we use (6.2) to make comparisons to the experiments.

Using (6.2) in (5.6) we obtain

$$C = \frac{P_{abs} P_{tot} \alpha H}{2 \ln |\alpha + 1|}, \tag{6.3}$$

which can be used to obtain $\mathcal{Q}$ as in (5.31). Following the procedure explained in Section 5.3 of Chapter 5, for $0 \leq \hat{x} \leq 1$,

$$\mathcal{Q} = \frac{P_{tot} \alpha P_{abs} \mu_{hot}}{3 H \rho F \hat{\chi}^2 c_p \Theta \ln |\alpha + 1|} \left(\frac{1}{\alpha \hat{x} + 1} \right), \tag{6.4}$$

where the hats denote the dimensionless quantities.

The model results rely on several material properties, which we either fix from the

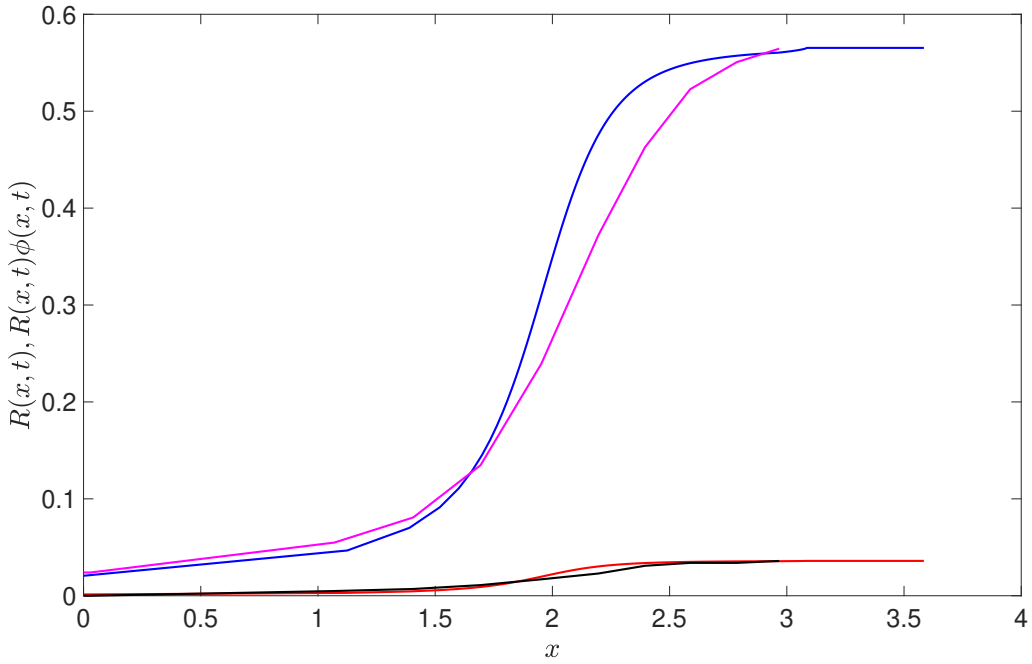

(a) A radial slice showing geometry using both model and experiment.

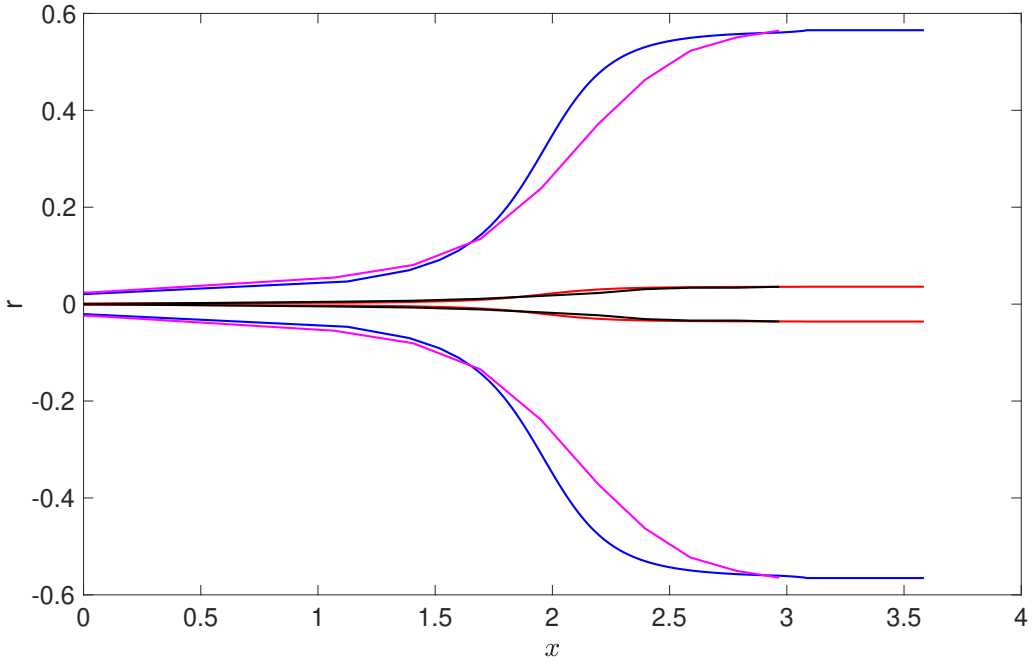

(b) Full image of the emitter using both model and experimental results.

Figure 6.8: Comparison of emitter geometry yielded by model and experiments with HEAT =240. Plotted against axial position are the external radius ($R(x,t)$) as given by (blue) the model, (magenta) experiments, and the internal radius $\phi(x,t)R(x,t)$ as given by (red) the model, (black) experiments. The geometry of the emitter is obtained with HEAT =240 and $\alpha = 1.15$. The initial cross-sectional area $\chi^2(x,0) = 1$ and aspect ratio $\phi(x,0) = 0.0635$, where initial ID = 19.086μm and OD = 300.07μm.

literature or infer through reasonable matches to experiments. We fix $P_{abs} = 0.76$, for energy absorption (by matching to experimental results), and $\beta = 0.8$, for emissivity from Jasion et al. (2015). Additionally, to obtain reasonable comparisons with the experimental trials, a heated length of $H = 0.85$mm for FILAMENT = 0 (1mm) is used, despite the fact that the nominal heater length is $H = 0.5$mm. This is not unreasonable given that conduction allows heat to be transmitted beyond the heated length and the size of the laser beam means it heats beyond the filament length. The other relevant physical quantities useful in generating the numerical solutions are summarised in Table 6.4 for convenience, unless otherwise specified. As in Chapter 5, computations could begin when the glass reaches softening point because deformations occur only within a narrow temperature range when the glass is sufficiently soft (thus at a high temperature). The starting temperature for computing the numerical solutions is set to $\theta_0 = 0.7$ corresponding to a physical temperature of 1518K. It is effectively assumed that there is no flow until the viscosity is low enough to start stretching. This is not unreasonable given the relatively slow flow until the temperature reaches a point where the viscosity is reduced sufficiently to allow for considerable deformation. Furthermore, to avoid unnecessary computational time, we stop computations when the maximum temperature across all the cross-section has reached the starting temperature (θ_0), such that $\theta_{\max}(x_j, t_K)) \leq \theta_0$ for $j = 1, 2, \ldots, J$.

The process of obtaining the numerical solutions is similar to that described in Section 5.4.1 of Chapter 5, with the exception of the function $q(x)$ used to compute the distribution of power and thus the distribution of temperature.

Figure 6.8 shows inner and outer radii of an emitter pulled with a temperature-dependent viscosity generated from the model when HEAT = 240 and is compared with the outcome of an experiment. Notice that the experimental result seems shorter compared with the model result near the undeformed end, this is because all experimental measurements in

the outer radius were initiated at a point where the difference between two measurements observed was in the fourth decimal place (measurements were almost similar up to three decimal places). Figure 6.8 (a) shows a radial slice through the emitter and Figure 6.8 (b) shows the full emitter using both experimental and model results.

We still have some work to do before we can use our model to make predictions. As discussed in Section 6.2.4 one significant difficulty in relation to comparison of the model with the experiments is the variation in the initial tube size across the experimental trials. Although the variability in the inner and outer diameter is measured in micrometres, the change in both the inner and outer diameters affects the initial cross-sectional area or thermal mass that is deformed and results are sensitive to this, probably because of the strong dependence of viscosity on temperature. We anticipate that the power distribution in the glass will vary with the cross-sectional area, which we model by changing the value of α as the tube size changes. Thus the value of α is considered to vary with the initial cross-sectional area of the tube in addition to the value of HEAT used in an experiment. Therefore, for different pairs of (HEAT, χ_0), while holding other parameters constant, we first computed the corresponding value of α (by trial and error) to give a good visual match to the experimental outcome. The initial cross-sectional area (χ_0) of the tube can be determined using the experimental ID and OD measurements. This process can be used to generate a data set of triples comprising (HEAT, χ_0, α) for each of the experiments conducted which can later be used effectively in the process of using the model for prediction.

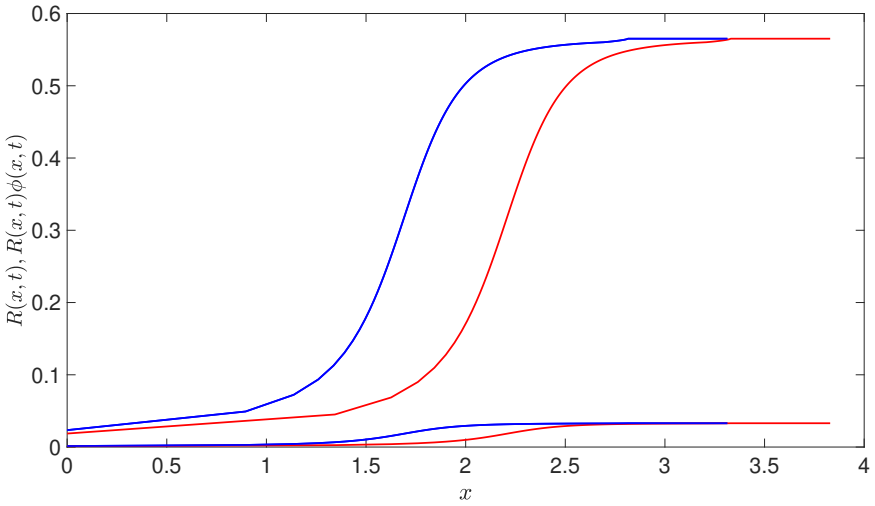

Figure 6.9: Comparison of emitter geometry yielded by the model with $\alpha = 1.152$ (both inner and outer channels in blue), and $\alpha = 1.154$ (both inner and outer channels in red). In both cases HEAT $= 240$. The initial cross-sectional area $\chi^2(x, 0) = 1$ and aspect ratio $\phi(x, 0) = 0.0635$, where initial ID $= 17.495\mu$m and OD $= 300.07\mu$m.

6.4 Model Prediction

To ensure that the model is truly beneficial to future experiments, we must automate the process of numerical prediction and demonstrate its performance using experiments not used for model calibration. To do this we consider a new experiment and for each intended HEAT value we perform a simple interpolation or extrapolation on the generated (χ_0, α) data set (discussed in Section 6.3) to find the value of α corresponding to the cross-sectional area of the tube, χ_0. This way we predict the value of α to use to make a prediction with our model.

Recall that α determines the distribution of power across the heated length and, when $q(x)$ was an exponential function, α was very sensitive to the geometry, requiring a prediction with at least three decimal places of precision. Similarly when $q(x)$ is a rational function the geometry is sensitive to the value of α. Figure 6.9 compares the sensitivity

of the inner and outer radii of the tube versus axial position for two similar values of α, differing only in third decimal place, when $q(x)$ is a rational function as given in (6.2). Note that the slope of the neck-down region of the body changes with the choice of α, with higher α producing the deepest curve for both inner and outer channels. There is also a difference in the overall lengths.

Figure 6.10 and 6.11 compare the model predictions with the average outer and inner radii versus axial position from the experimental results obtained for four distinct power values, HEAT =240, 242, 244, 246, over the course of 12 experimental trials with three trials for each power. In all cases the tube separated (broke) into two emitters at the end of a pull. For each power, the value of α required to generate the model result was predicted by interpolation of the data set generated in model calibration as described in the previous section. The overall agreement between the experimental data and the model output is very good. For each power the average initial cross-sectional area is as given in the caption. The length of the emitter is not considered critical and experimental measurements can contain error because of the need to stitch two or more photographs together to show the whole emitter. Thus, it was hard to measure the taper length accurately. These predictions depend on the existing data and without a doubt can be improved further with the availability of more data, maintenance of the P-2000 puller and improved experimental techniques. Until experimental techniques are improved, there is little points in striving for a better fit between model and experiments.

6.5 Summary

The micro-scale nature of the problem significantly complicates both the modelling and experimental processes. There are some inconsistencies in the ID and OD measurements

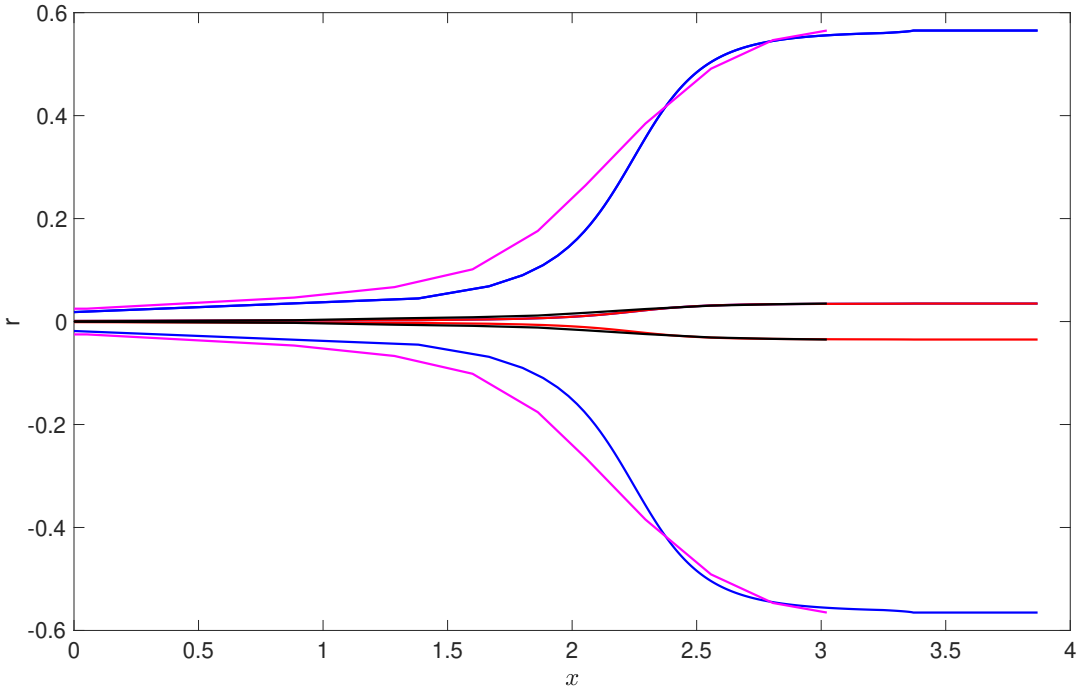

(a) Plot of final emitter geometry for a tube corresponding to HEAT =240 starting with an initial cross-sectional area $S_0 = 265.5780\mu\text{m}^2$. The numerically predicted value of α is $\alpha = 1.1574$).

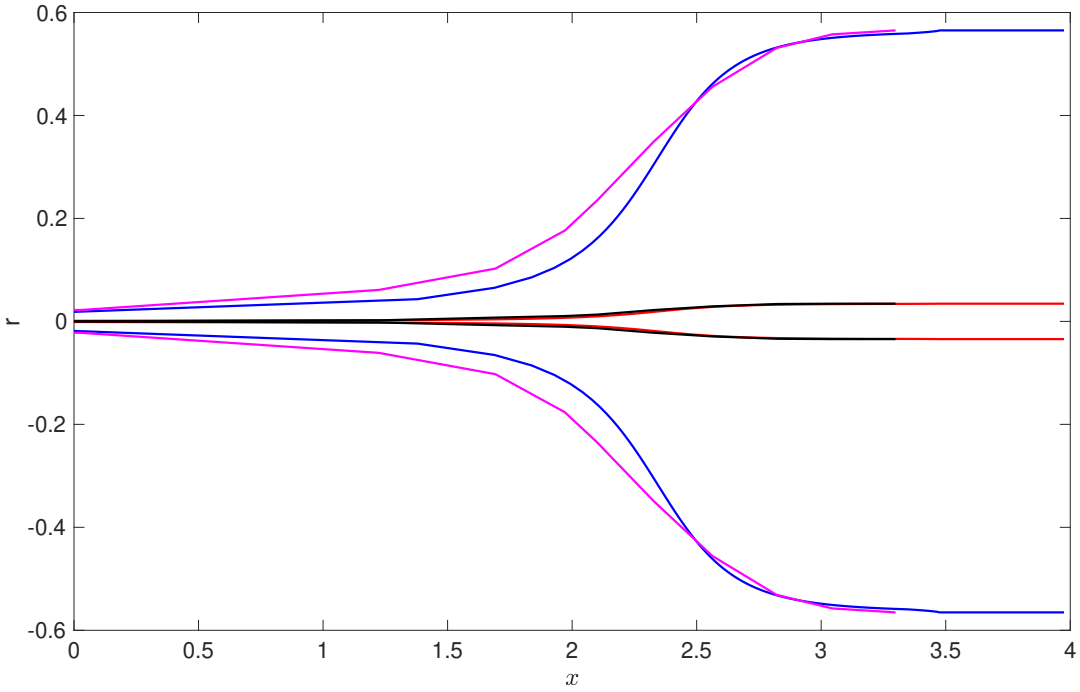

(b) Plot of final emitter geometry for a tube corresponding to HEAT =242 starting with an initial cross-sectional area $S_0 = 264.4986\mu\text{m}^2$. The numerically predicted value of α is $\alpha = 1.0690$).

Figure 6.10: The model results in blue (OD) and red (ID) are compared with the experiment plotted in black (ID) and magenta (OD) in each figure.

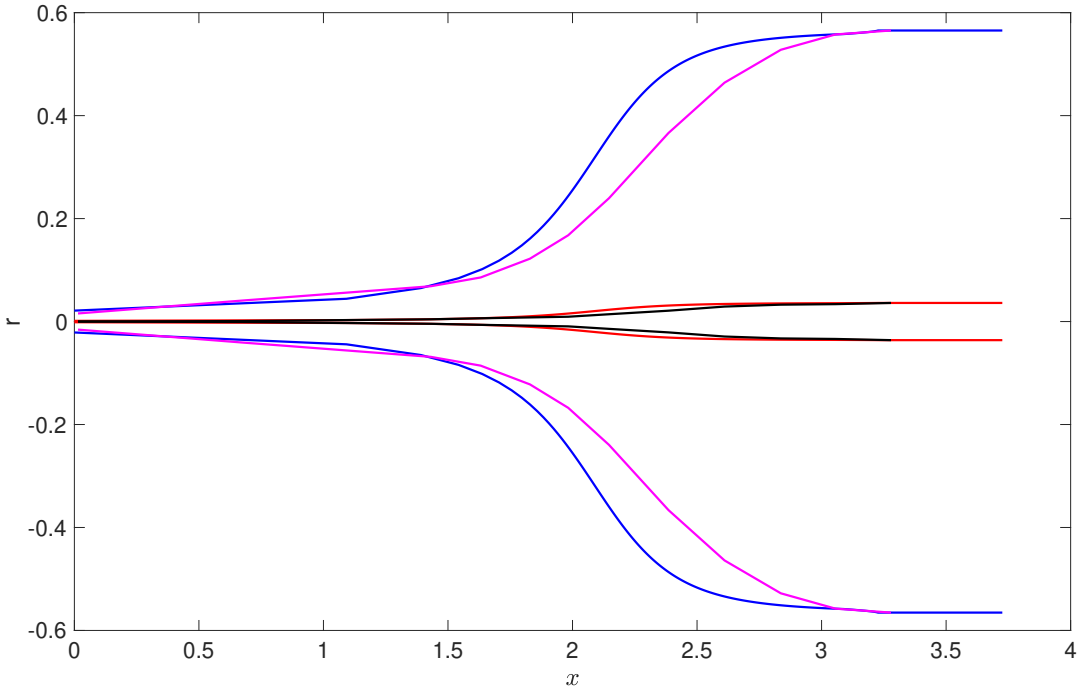

(a) Plot of final emitter geometry for a tube corresponding to HEAT =244 starting with an initial cross-sectional area $S_0 = 264.1360\mu\text{m}^2$. The numerically predicted value of α is $\alpha = 1.0077$).

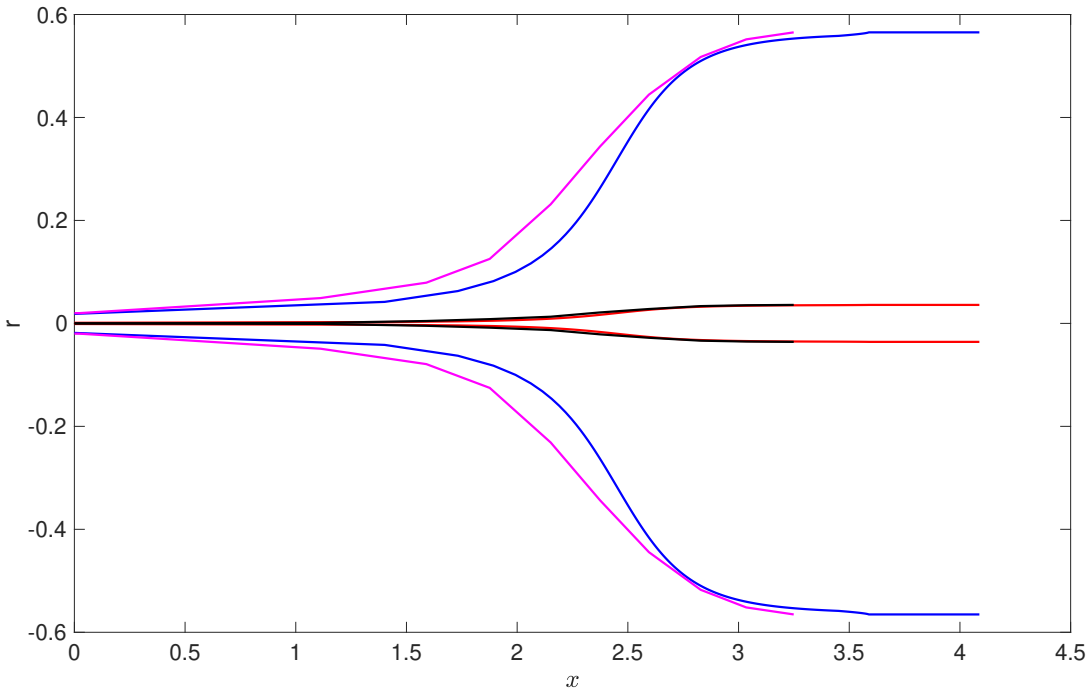

(b) Plot of final emitter geometry for a tube corresponding to HEAT =246 starting with an initial cross-sectional area $S_0 = 265.8623\mu\text{m}^2$. The numerically predicted value of α is $\alpha = 1.0109$).

Figure 6.11: The model results in blue (OD) and red (ID) are compared with the experiment plotted in black (ID) and magenta (OD) in each figure.

along the length of the tube before the pull, which impacts the heat distribution and the viscosity profiles during the pull.

Along with the model, we have extensively explored the zero velocity or the timed heat program, which might not be the best option for manufacturing emitters using the P-2000. However, this program is less challenging from a modelling and experimental point of view as the number of parameters can be minimised. Importantly, the ability to model a single line programme from the beginning to the end of a pull is not possible with a non-zero velocity programme, as the changes from one loop to the next are unknown, necessitating the use of numerous assumptions that may not be realistic in terms of modelling.

We have used the experiments using the timed heat program in two different ways namely model calibration and prediction using a suitable function for $q(x)$ as described in detail in this chapter. Model calibration comes first, where we have used different pairs of (HEAT, χ_0), holding all other parameters constant, to find by trial and error the corresponding α that gives good agreement with the experiment. This gives us a data set of (HEAT, χ_0, α) for each experiment. This is followed by model prediction. For the prediction we have taken the values of the generated data set and interpolated/extrapolated over the calibration data to find α to obtain a model prediction of the final shape of the emitter. We then compare the model output with experimental measurements to see how well they agree. Despite all known and possible sources of error, there exists a satisfying agreement between the numerical solutions derived from the coupled flow and energy models and the actual experimental data. Regardless of the experimental imperfections, the accuracy of the numerical solutions addressed in this chapter are also strongly dependent on the material properties, which have been difficult to quantify precisely owing to the extensive variations in the temperature. Importantly, the methodology we have developed in this chapter may be used to obtain an improved predictive model once experimental

techniques are improved.

Most of the separated emitters out of the zero velocity program had a nice long taper with a much simpler conical shape compared with non-zero velocity. For similar OD and ID measurements of the initial fibre tubing the time taken to pull the emitters is about the same and the taper profiles are similar.

Chapter 7

Conclusion

In this thesis we have developed a mathematical model and a numerical solution method for the unsteady heat and draw process used for tapering of tubular glass fibres. For the first time active pressurisation of internal channels has been included in an unsteady fibre-drawing model, enabling investigation of the competition between the surface tension and the pressure. The most important outcome of this work is to demonstrate the feasibility of manufacture of emitters with a near-uniform bore by the heat and pull process with active pressurisation of the channel. The symmetry of the process means that two identical emitters are obtained from a single heat and pull process by cutting/breaking the tube at the centre. The geometry at the centre then corresponds to the geometry at the very tip of the emitter.

Asymptotic methods are used which exploit the slenderness of the tube. The use of asymptotic methods throughout has resulted in a system of leading order equations, reducing the governing equations and boundary conditions into two simplified models describing the axial and transverse flow problems and a third model for temperature. This thesis begins with the flow model assuming viscosity as a function of axial position and time (uniform in a cross-section) which is later coupled with a temperature model.

Lagrangian coordinates and reduced time transformations were found to be useful

in generating the solutions, with the latter being used for generating a classical two-dimensional Stokes flow problem with moving boundaries driven by unit surface tension and applied pressure. The Lagrangian reference frame has been useful to track the motion of cross-sections and solve for each cross-section. With the internal channel being pressurised, the axial and transverse flow models, which comprise the full flow model, need to be solved simultaneously, requiring a numerical solution. The numerical solution we have developed can be used to solve for the flow in an unsteady setting, while taking into account the changes in viscosity with time and axial position throughout the deformation process. The computations are complicated, requiring knowledge of the previous history of the viscosity of the cross-sections at previous time steps in order to compute solutions for all future times.

The model and solution method described in this thesis enable determination of a pulling force, channel over-pressure, and draw time to achieve tapers with a desired internal diameter and wall thickness at the very tip from a given tubular fibre for a temperature-dependent viscosity. There is no unique solution to this problem; multiple parameter sets for the draw parameters will yield the same geometry at the tip with a larger pulling force requiring a larger over-pressure. However, the shape of the internal channel along the length of the taper, will change with the choice of parameters and so we optimise this choice to target an inner channel with as close to a constant diameter as possible.

The geometry of the emitter is quite sensitive to the pulling force and pressure parameters. An emitter for use in mass spectrometry, having a tip with a channel diameter near to that of the original fibre and small wall thickness, implies a geometry at the tip with significantly larger aspect ratio ϕ and smaller cross-sectional area χ^2 than the original fibre which, in turn, implies an over-pressure and pulling force that are nearing the regime

where the fibre may burst or break. As the pulling force and over-pressure reduce, the sensitivity increases such that a very small variation in the force or pressure will result in the fibre bursting ($\phi \to 1$) or the channel closing ($\phi \to 0$). Note that such a failure will occur first at the tip which is subjected to the greatest amount of heat and consequently undergoes more deformation than any other cross-section. Practical limitations on maintaining the force and pressure at given values will, then, require that these parameters be sufficiently large so that small variations do not result in unacceptable changes in ϕ at the tip. However, larger force and over-pressure result in greater non-uniformity of the internal channel, i.e. a larger bulge in the inner channel, so that increasing these parameters too much is also not desirable. Clearly there is a trade-off between the two and an optimisation problem to be solved based on the physical limitations of the puller and the fitness for purpose of the taper.

The model has also been used to explore the importance of over-pressure relative to surface tension in governing the transverse flow geometry in unsteady stretching of an annular capillary tube. It has been shown that if the surface tension is small compared with the applied pressure, then the flow in the cross-plane can be explained in terms of the pressure, neglecting the effect of surface tension, and an analytical solution for the full model in terms of τ can be obtained. Using these solutions practical limitations such fibre break or fibre burst during a draw using reduced time can be identified. Furthermore, two important approximations, namely weak and zero surface tension are identified. We found that if $O(10^{-2}) \leq \hat{\gamma}/\hat{P} \leq O(10^{-1})$ then the effect of the surface tension is important and cannot be neglected. However, for $O(10^{-3}) \leq \hat{\gamma}/\hat{P} \leq O(10^{-2})$, the surface tension has weak effect and can be neglected in the axial flow problem but will have some impact in the cross-plane flow problem and should be considered when predicting the deformations in the cross-section geometry.

To characterise the deformation process completely, either the viscosity must be known or the viscosity must be calculated using a temperature model coupled to the flow model. In this thesis, we concentrated on heating the glass for a specified time with a laser and developed the temperature model with the option of selecting a suitable power distribution to suit experiments which were done with the Sutter P-2000 puller.

The experimental results have been used first to generate a data set to determine the model parameters which was later used in the prediction. Despite the limitations associated with obtaining accurate temperature measurements experimentally, the model shows overall good agreement with the experiments in determining the temperature changes and thus the deformations during the whole glass deforming process. Although the model can be used to gain insights into the selection of operational parameters, the optimal parameter combination needs to be determined with reference to physical limitations of the puller used and permissible tolerances on the geometry. We leave for future work the comparison of the model predictions in terms of adding pressure with the experiments which require that the puller be modified.

The temperature model we have developed is a simple one applicable only to one mode of operation of the P-2000 puller, namely the Timed heat at velocity zero case only. Further work is still needed to completely validate the model, even for this case, which requires inaccuracies in the puller to be fixed. Once this is done the model might be adapted for other modes of operation of the puller. Our goal was to create a simple model that gives understanding about the sensitivity of geometry to the process parameters used in the Sutter P-2000 puller. We have seen that results are very sensitive to parameters in the temperature model. This is consistent with experimental findings and a feature of emitter tip fabrication, linked to the fact that glass viscosity is strongly temperature dependent. This is not a reason to discount the value of mathematical modelling. Rather,

the sensitivity of emitter tip fabrication to the process parameters makes mathematical modelling of considerable value for understanding practical outcomes, estimating process parameters, and learning how to control the fabrication process.

The flow model developed in this thesis considers the use of constant pressure in the inner channel. While this seems to be reasonable, the use of non constant pressure may need to be explored in the future. As seen from our modelling, once the laser is turned off, the tube cools and solidifies fastest at the tip where there is less thermal mass while parts with more thermal mass continue to deform. This suggests the possibility to minimise the bulge in the tube by gradually reducing the pressure over time. Another interesting future extension of this model would be to the unsteady stretching of tubes with complex internal geometries (e.g. multiple internal channels).

We conclude by noting that, while we have focussed on manufacture of emitters for mass spectrometry, our model has, with suitable modifications, wider applications, such as to the manufacture of microbottles for whispering gallery resonator sensors. However, this is for future investigation and is beyond the scope of the current thesis.

Bibliography

Axinte, E. (2011), 'Glasses as engineering materials: A review', *Materials & Design* **32**(4), 1717–1732.

Boyd, K., Ebendorff-Heidepriem, H., Monro, T. M. & Munch, J. (2012), 'Surface tension and viscosity measurement of optical glasses using a scanning co 2 laser', *Optical Materials Express* **2**(8), 1101–1110.

Bradshaw-Hajek, B. H., Stokes, Y. M. & Tuck, E. O. (2007), 'Computation of extensional fall of slender viscous drops by a one-dimensional eulerian method', *SIAM Journal on Applied Mathematics.* **67**(4), 1166–1182.

Chen, M. J., Stokes, Y. M., Buchak, P., Crowdy, D. G. & Ebendorff-Heidepriem, H. (2015), 'Microstructured optical fibre drawing with active channel pressurisation', *Journal of Fluid Mechanics* **783**, 137–165.

Chouffart, Q. (2018), Experimental and numerical Investigation of the continuous Glass Fiber Drawing Process, PhD thesis, Department of Aerospace and Mechanical Engineering, University of Liège.

Chryssou, C. E. (1999), 'Theoretical analysis of tapering fused silica optical fibers using a carbon dioxide laser', *Optical Engineering* **38**(10), 1645–1649.

Cummings, L. J. & Howell, P. D. (1999), 'On the evolution of non-axisymmetric viscous fibres with surface tension, inertia and gravity', *Journal of Fluid Mechanics* **389**, 361–389.

Dewynne, J. N., Howell, P. D. & Wilmott, P. (1994), 'Slender viscous fibres with inertia and gravity', *Quarterly Journal of Mechanics and Applied Mathematics* **47**(4), 541–555.

Dewynne, J. N., Ockendon, J. R. & Wilmott, P. (1992), 'A systematic derivation of the leading-order equations for extensional flows in slender geometries', *Journal of Fluid Mechanics* **244**, 323–338.

Dewynne, J., Ockendon, J. R. & Wilmott, P. (1989), 'On a mathematical model for fiber tapering', *SIAM Journal on Applied Mathematics* **49**(4), 983–990.

Dole, M., Mack, L. L., Hines, R. L., Mobley, R. C., Ferguson, L. D. & Alice, M. B. (1968), 'Molecular beams of macroions', *The Journal of Chemical Physics* **49**, 2240–2249.

Doremus, R. H. (2002), 'Viscosity of silica', *Journal of Applied Physics* **92**(12), 7619–7629.

Ek, P. & Roeraade, J. (2011), 'New method for fabrication of fused silica emitters with submicrometer orifices for nanoelectrospray mass spectrometry', *Analytical Chemistry* **83**(20), 7771–7777.

Fitt, A. D., Furusawa, K., Monro, T. M. & Please, C. P. (2001), 'Modeling the fabrication of hollow fibers: capillary drawing', *Journal of Lightwave Technology* **19**(12), 1924.

Fitt, A. D., Furusawa, K., Monro, T. M., Please, C. P. & Richardson, D. J. (2002), 'The mathematical modelling of capillary drawing for holey fibre manufacture', *Journal of Engineering Mathematics* **43**(2), 201–227.

Gallacchi, R., Kölsch, S., Kneppe, H. & Meixner, A. J. (2001), 'Well-shaped fibre tips by pulling with a foil heater', *Journal of Microscopy* **202**(1), 182–187.

Gibson, G. T. T., Mugo, S. M. & Oleschuk, R. D. (2009), 'Nanoelectrospray emitters: Trends and perspective', *Mass Spectrometry Reviews* **28**, 918–936.

Grellier, A. (2000), Characterisation of optical fibre tapering using a CO_2 laser, PhD thesis, University of Kent at Canterbury.

Grellier, A. J. C., Zayer, N. K. & Pannell, C. N. (1998), 'Heat transfer modelling in CO_2 laser processing of optical fibres', *Optics Communications* **152**(4-6), 324–328.

Griffiths, I. M. & Howell, P. D. (2007), 'The surface-tension-driven evolution of a two-dimensional annular viscous tube', *Journal of Fluid Mechanics* **593**, 181–208.

Griffiths, I. M. & Howell, P. D. (2008), 'Mathematical modelling of non-axisymmetric capillary tube drawing', *Journal of Fluid Mechanics* **605**, 181–206.

Hannis, J. C. & Muddiman, D. C. (1998), 'Nanoelectrospray mass spectrometry using non-metalized, tapered (50→ 10 μm) fused-silica capillaries', *Rapid Communications in Mass Spectrometry* **12**, 443–448.

He, D., Wylie, J. J., Huang, H. & Miura, R. M. (2016), 'Extension of a viscous thread with temperature-dependent viscosity and surface tension', *Journal of Fluid Mechanics* **800**, 720–752.

Helebrant, A., Buerhop, C. & Wei𝔅mann, R. (1993), 'Mathematical modelling of temperature distribution during co_2 laser irradiation of glass', *Glass Technology* **34**(4), 154–158.

Ho, C. S., Lam, C. W. K., Chan, M. H. M., Cheung, R. C. K., Law, L. K., Lit, L. C. W., Ng, K. F., Suen, M. W. M. & Tai, H. L. (2003), 'Electrospray ionisation mass

spectrometry: Principles and clinical applications', *The Clinical Biochemist Reviews* **24**(1), 3–12.

Howell, P. D., Wylie, J. J., Huang, H. & Miura, R. M. (2007), 'Stretching of heated threads with temperature-dependent viscosity: Asymptotic analysis', *Discrete & Continuous Dynamical Systems - B* **7**(3), 553–572.

Huang, H., Miura, R. M., Ireland, W. P. & Puil, E. (2003), 'Heat-induced stretching of a glass tube under tension: Application to glass microelectrodes', *SIAM Journal on Applied Mathematics* **63**(5), 1499–1519.

Huang, H., Wylie, J. J., Miura, R. M. & Howell, P. D. (2007), 'On the formation of glass microelectrodes', *SIAM Journal on Applied Mathematics* **67**(3), 630–666.

Jasion, G. T., Shrimpton, J. S., Chen, Y., Bradley, T., Richardson, D. J. & Poletti, F. (2015), 'Microstructure element method (msem): viscous flow model for the virtual draw of microstructured optical fibers', *Optics Express* **23**(1), 312–329.

Kelly, R. T., Page, J. S., Luo, Q., Moore, R. J., Orton, D. J., Tang, K. & Smith, R. D. (2006), 'Chemically etched open tubular and monolithic emitters for nanoelectrospray ionization mass spectrometry', *Analytical Chemistry* **78**(22), 7796–7801.

Kriger, M. S., Cook, K. D. & Ramsey, R. S. (1995), 'Durable gold-coated fused silica capillaries for use in electrospray mass spectrometry', *Analytical Chemistry* **67**(2), 385–389.

Kusỳ, P., Klepárník, K., Aturki, Z., Fanali, S. & Foret, F. (2007), 'Optimization of a pressurized liquid junction nanoelectrospray interface between ce and ms for reliable proteomic analysis', *Electrophoresis* **28**(12), 1964–1969.

Luzi, G., Epple, P., Scharrer, M., Fujimoto, K., Rauh, C. & Delgado, A. (2010), 'Influence of surface tension and inner pressure on the process of fibre drawing', *Journal of Lightwave Technology* **28**(13), 1882–1888.

Matovich, M. A. & Pearson, J. R. A. (1969), 'Spinning a molten threadline. steady-state isothermal viscous flows', *Industrial & Engineering Chemistry Fundamentals* **8**(3), 512–520.

Modest, M. F. (2013), *Radiative heat transfer*, 3 edn, Academic press.

Morris, C. A., Friedman, A. K. & Baker, L. A. (2010), 'Applications of nanopipettes in the analytical sciences', *Analyst* **135**, 2190–2202.

Pearson, J. R. A. & Petrie, C. J. S. (1970), 'The flow of a tubular film. Part 1. Formal mathematical representation', *Journal of Fluid Mechanics* **40**(1), 1–19.

Radionova, A. (2019), Theta-Channel Emitters for Nano-Electrospray and Mass Spectrometry, Phd thesis, The University of Auckland.

Ranathunga, G. P., Stokes, Y. M. & Chen, M. J. (2022), 'Unsteady stretching of a glass tube with internal channel pressurisation', *arXiv preprint arXiv:2201.05243* .

Sander, K. & Elisabeth, V. (2007), 'A decade of microfluidic analysis coupled with electrospray mass spectrometry: An overview', *Lab on a Chip* **7**, 1394–1412.

Scherer, G. W. (1992), 'Editorial comments on a paper by Gordon S. Fulcher', *Journal of the American Ceramic Society* **75**(5), 1060–1062.

Stokes, Y. M., Bradshaw-Hajek, B. H. & Tuck, E. O. (2011*a*), 'Extensional flow at low Reynolds number with surface tension', *Journal of Engineering Mathematics* **70**, 321–331.

Stokes, Y. M., Bradshaw-Hajek, B. H. & Tuck, E. O. (2011*b*), 'Extensional flow at low Reynolds number with surface tension', *Journal of Engineering Mathematics* **70**(1-3), 321–331.

Stokes, Y. M., Buchak, P., Crowdy, D. G. & Ebendorff-Heidepriem, H. (2014), 'Drawing of micro-structured fibres: circular and non-circular tubes', *Journal of Fluid Mechanics* **755**, 176–203.

Stokes, Y. M. & Tuck, E. O. (2004), 'The role of inertia in extensional fall of a viscous drop', *Journal of Fluid Mechanics* **498**, 205–225.

Stokes, Y. M., Tuck, E. O. & Schwartz, L. W. (2000), 'Extensional fall of a very viscous fluid drop', *The Quarterly Journal of Mechanics and Applied Mathematics* **53**(4), 565–582.

Stokes, Y. M., Wylie, J. J. & Chen, M. J. (2019), 'Coupled fluid and energy flow in fabrication of microstructured optical fibres', *Journal of Fluid Mechanics* **874**, 548–572.

Sutter Instrument (2010), *P-2000 laser based micropipette puller system operation manual*, Rev 2.2 (20100629), One Digital Drive Novato, CA 94949. `www.sutter.com`.

Tronnolone, H. (2016), Extensional and surface-tension-driven fluid flows in microstructured optical fibre fabrication, PhD thesis, The University of Adelaide.

Tronnolone, H., Stokes, Y. M. & Ebendorff-Heidepriem, H. (2017), 'Extrusion of fluid cylinders of arbitrary shape with surface tension and gravity', *Journal of Fluid Mechanics* **810**, 127–154.

Tronnolone, H., Stokes, Y. M., Foo, H. T. C. & Ebendorff-Heidepriem, H. (2016), 'Gravitational extension of a fluid cylinder with internal structure', *Journal of Fluid Mechanics* **790**, 308–338.

Tycova, A., Prikryl, J. & Foret, F. (2016), 'Reproducible preparation of nanospray tips for capillary electrophoresis coupled to mass spectrometry using 3D printed grinding device', *Electrophoresis* **37**(7-8), 924–930.

Valaskovic, G. A., Kelleher, N. L., Little, D. P., Aaserud, D. J. & McLafferty, F. W. (1995), 'Attomole-sensitivity electrospray source for large-molecule mass spectrometry', *Analytical Chemistry* **67**(20), 3802–3805.

Von der Ohe, R. & Yue, Y. (2003), Simulation of glass fiber forming processes, PhD thesis, Faculty of Engineering and Science, Aalborg University.

Voyce, C. J., Fitt, A. D., Hayes, J. R. & Monro, T. M. (2009), 'Mathematical modeling of the self-pressurizing mechanism for microstructured fiber drawing', *Journal of Lightwave Technology* **27**(7), 871–878.

Wadsworth, W. J., Witkowska, A., Leon-Saval, S. G. & Birks, T. A. (2005), 'Hole inflation and tapering of stock photonic crystal fibres', *Optics Express* **13**(17), 6541–6549.

Wang, T., Liu, J., Yang, B., Chen, X., Wang, X. & Yang, C. (2016), 'Optimization of micropipette fabrication by laser micromachining for application in an ultrafine atmospheric pressure plasma jet using response surface methodology', *Journal of Micromechanics and Microengineering* **26**(6), 065001.

Wilm, M. & Mann, M. (1996), 'Analytical properties of the nanoelectrospray ion source', *Analytical Chemistry* **68**(1), 1–8.

Wilm, M. S. & Mann, M. (1994), 'Electrospray and taylor-cone theory, Dole's beam of macromolecules at last?', *International Journal of Mass Spectrometry and Ion Processes* **136**(2-3), 167–180.

Wu, X. (2012), Modeling and characterization of microfabricated emitters: In pursuit of improved esi-ms performance, Master's thesis, Queen's University Kingston, Ontario, Canada.

Wylie, J. J., Bradshaw-Hajek, B. H. & Stokes, Y. M. (2016), 'The evolution of a viscous thread pulled with a prescribed speed', *Journal of Fluid Mechanics* **795**, 380–408.

Wylie, J. J. & Huang, H. (2007), 'Extensional flows with viscous heating', *Journal of Fluid Mechanics* **571**, 359–370.

Wylie, J. J., Huang, H. & Miura, R. M. (2007), 'Thermal instability in drawing viscous threads', *Journal of Fluid Mechanics* **570**, 1–16.

Wylie, J. J., Huang, H. & Miura, R. M. (2011), 'Stretching of viscous threads at low Reynolds numbers', *Journal of Fluid Mechanics* **683**, 212–234.

Wylie, J. J., Huang, H. & Miura, R. M. (2015), 'Asymptotic analysis of a viscous thread extending under gravity', *Physica D: Nonlinear Phenomena* **313**, 51–60.

Yadav, P. R., Han, T., Olatunji, O., Pattanayek, S. K. & Das, D. B. (2020), 'Mathematical modelling, simulation and optimisation of microneedles for transdermal drug delivery: Trends and progress', *Pharmaceutics* **12**(8), 693–724.

Yarin, A. L. (1986), 'Effect of heat removal on nonsteady regimes of fiber formation', *Journal of Engineering Physics* **50**(5), 569–575.

Yokota, H., Sugai, E. & Sasaki, Y. (1997), 'Optical irradiation method for fiber coupler fabrications', *Optical Review* **4**(1A), 104–107.

Yuill, E. M., Sa, N., Ray, S. J., Hieftje, G. M. & Baker, L. A. (2013), 'Electrospray ionization from nanopipette emitters with tip diameters of less than 100 nm', *Analytical Chemistry* **85**(18), 8498–8502.